DEVELOPMENT AND TESTING OF NEW STRATEGIES FOR PRE-PROCESSING AND ANALYSIS OF 4D FLOW-SENSITIVE MRI DATA

vorgelegt von

Jelena Bock

Dissertation zur Erlangung des Doktorgrades
der Technischen Fakultät
der Albert-Ludwigs-Universität Freiburg im Breisgau

Dekan	Prof. Dr. B. Becker
Gutachter	Prof. Dr. H. Burkhardt
	Prof. Dr. M. Markl
Vorsitz	Prof. Dr. Peter Thiemann
Beisitz	Prof. Dr. Matthias Teschner
Tag der Prüfung	10.04.2013

Autor Jelena Bock
Radiologische Klinik - Medizin Physik
Universitätsklinikum Freiburg

DEVELOPMENT AND TESTING OF NEW STRATEGIES FOR PRE-PROCESSING AND ANALYSIS OF 4D FLOW-SENSITIVE MRI DATA

Layout based on a LaTeX style by Jan Lienemann & Simon Dreher

Contents

Abbreviations

3D	Three-Dimensional: three dimensions
4D	Four-Dimensional: three dimensions and time
AA	Aortic Arch
AAo	Ascending Aorta
BPA	Blood-Pool contrast Agent
bpm	Beats Per Minute
CA	Contrast Agent
CE-MRA	Contrast Enhanced Magnetic Resonance Angiography
CNR	Contrast-to-Noise Ratio
CT	Computed Tomography
CWT	Continuous Wavelet Transform
DAo	Descending Aorta
DICOM	Digital Imaging and COmmunications in Medicine
DSA	Digital Subtraction Angiography
DWT	Discrete Wavelet Transform
ECA	Extracellular Contrast Agent
ECG	ElectroCardioGram
FCM	Fuzzy c-Means
FFT	Fast Fourier Transform
FOV	Field Of View
GRE	GRadient Echo

MIP	Maximum Intensity Projection
MRI	Magnetic Resonance Imaging
NMR	Nuclear Magnetic Resonance
PC-MRI	Phase-Contrast Magnetic Resonance Imaging
PC-MRA	Phase-Contrast Magnetic Resonance Angiography
PD	Pressure Difference
PET	Positron-Emission Tomography
PWV	Pulse Wave Velocity
ROI	Region Of Interest
RF	Radio Frequency
SNR	Signal to Noise Ratio
SPECT	Single-Proton-Emission CT
stdev	standard deviation
TE	Echo Time
TR	Repetition Time
US	UltraSound
v_{enc}	Velocity Encoding

Zusammenfassung

Vaskuläre Krankheiten, vor allem Atherosklerose, bilden die Haupttodesursache in den Industrienationen. Um diese Krankheiten vorzubeugen und zu behandeln, ist es wichtig den Prozess der Krankheitsentstehung und der -progression besser zu verstehen. Mehrere Risikofaktoren können die Entwicklung vaskulärer Krankheiten beeinflussen: Rauchen, wenig Bewegung, genetische Prädispositionen.
Des Weiteren spielt auch die Hämodynamik eine wichtige Rolle, da der Fluss direkt auf die Gefäßwand einwirkt (Druck, Scherkräfte) und somit ein Zusammenhang zwischen pathologisch verändertem Fluss und der Entstehung und/oder Progression von häufig vorkommenden Erkrankungen der Aorta (Aneurysma, Aortendissektion, usw.) besteht. Daher ist die Entwicklung neuer Methoden zur Untersuchung des hämodynamischen Verhaltens interessant und viel versprechend für die Diagnose und Prognose von Gefäßkrankheiten.
Um die Hämodynamik in den Gefäßen zu untersuchen, bietet sich zeitaufgelöste flusssensitive 3D Phasenkontrast-Magnetresonanztomographie (PC-MRT) an. Sie ermöglicht zusätzlich zu der Aufnahme der Gefäßmorphologie auch die Akquisition der räumlich registrierten Geschwindigkeitsvektorfelder, die den lokalen Blutfluss oder die Gewebebewegung während des Herzzyklus beschreiben. Um jedoch aus resultierenden mehrdimensionalen Datensätzen (drei räumliche Dimensionen, drei Geschwindigkeitsrichtungen und Zeit) zuverlässige hämodynamische Parameter zu erhalten, sind einige Vorverarbeitungs- und Quantifizierungsschritte notwendig.
In der vorliegenden Arbeit geht es um die Entwicklung und Erprobung neuer Strategien zur Bearbeitung und Analyse solcher zeitaufgelösten MR-Flussdaten.
Es wurden zunächst mehrere neue Algorithmen für die 3D Gefäßextraktion, die sogenannte 3D Phasenkontrast-MR-Angiographie (PC-MRA), aus den flusssensitiven Daten evaluiert. Die Gefäßgeometrie zu kennen ist wichtig, um zuverlässig die hämodynamischen Parameter nur innerhalb des Gefäßes abzuleiten und somit keine Werte von außerhalb des Gefäßes die Rechnung verfälschen. Ausserdem ist die Gefäßgeometrie für Berechnung der Druckgradienten oder der Wandschubspannung notwendig, da für diese Parameter die Gefäßwand als Randbedingung benötigt wird. Des Weiteren wurde die berechnete PC-MRA mit der Standardmethode, der kontrastverstärkten (CE)

MRA verglichen, sowie der Einfluss unterschiedlicher Kontrastmittel auf die PC-MRA untersucht.
Die Ergebnisse dieser Studie zeigten keinen signifikanten Qualitätsunterschied zwischen PC-MRA und CE-MRA. Die PC-MR Daten, die mit Kontrastmittel aufgenommen wurden, zeigten ein signifikant besseres Signal-zu-Rausch-Verhältnis in den morphologischen Daten, eine Reduktion des Rauschens in den Geschwindigkeitsdaten und eine bessere Visualisierung im Vergleich zu den Daten, die ohne Kontrastmittel aufgenommen wurden.
Im nächsten Schritt wurde die Gefäßextraktion von der statischen 3D auf die zeitaufgelöste 3D (4D Segmentierung) erweitert. Dafür wurde das Clustering-Verfahren eingesetzt, welches das Unterteilen der Daten in verschiedene Gruppen (Gefäß, Rauschen, statisches Gewebe) ermöglicht. Das Unterteilen in Gruppen ist bei PC-MR Daten von Vorteil, da diese nicht nur Fluss/Gefäß beinhalten, sondern auch statisches Gewebe und Rauschen. Die Gruppen können dann für die weitere Analyse bzw. Korrektur der Daten eingesetzt werden.
Die 4D Segmentierung wurde sowohl mit der statischen 3D Segmentierung als auch mit der manuellen Standardmethode verglichen. Mit der zeitaufgelösten Segmentierung kann im Vergleich zu einer starren Segmentierung die Bewegung der Gefäßwand besser dargestellt werden sowie die Flussparameter korrekter berechnet werden und weichen weniger von der manuellen Standardmethode ab.
Um die klinische Anwendbarkeit der PC-MR-Daten zu bestätigen, wurde eine Probanden- und Patientenstudie durchgeführt, bei der Druckgradienten in den Gefäßen aus den PC-MR-Geschwindigkeitsdaten abgleitet wurden. Der Druckgradient ist ein relevanter klinischer Marker für den Schweregrad kardiovaskulärer Erkrankungen wie Aortenisthmusstenose oder Aortenklappestenose. In der klinische Routine wird standardmäßig eine Katheteruntersuchung eingesetzt, also eine invasive Methode, um den Gradient zu bestimmen. Aus den mit PC-MR aufgenommenen Geschwindigkeitsdaten können die Druckgradienten nicht-invasiv mit Hilfe von Navier-Stokes-Gleichung abgeleitet werden.
Diese Studie hat gezeigt, dass es möglich ist, zuverlässige Druckgradientenwerte aus den zeitaufgelösten PC-MR-Daten zu berechnen.

Die in dieser Arbeit vorgestellten Methoden ermöglichen auf Basis der zeitaufgelösten 3D Phasenkontrast-MR Daten sowohl die Gefäßmorphologie zu bestimmen als auch zuverlässig die Hämodynamik in dem Gefäß zu charakterisieren.

1 Introduction

1.1 Motivation

A man is as old as his arteries - Thomas Sydenham (1624 - 1689) was one of the first physicians to recognize which important role the vessels play for human's health [1]. Nowadays, centuries later, arterial diseases especially atherosclerosis are the leading cause of death in industrialized nations [2]. To cure these diseases successfully one must understand the process of development and progression of the pathologies. In the case of vascular disease, origin and progression are a multi-factorial process. Many risk factors causing cardiovascular diseases, such as unhealthy diet, smoking, no exercise, genetics have been identified and investigated [2, 3].

In recent years, the hemodynamic has been recognized as an important contributor [4, 5]. Since flowing blood directly interacts with the vessel and alters its morphology, cardiovascular research aims to understand the complex dynamical behavior of the blood flow. New insights into the hemodynamic behavior may reveal relevant information for future diagnosis and prognosis [6]. To investigate the hemodynamics, time-resolved 3 dimensional (3D) Phase Contrast (PC) Magnetic Resonance Imaging (MRI) has been proven to be a useful tool. PC-MRI allows for the *in vivo* assessment of time-resolved 3 directional velocity vector field information [7], without restriction to anatomic coverage or flow directions [8]. The acquired data can be used to display and to investigate time-resolved 3D (4D) flow and subsequently to derive and to analyze hemodynamic parameters such as wall shear stress [9] and pressure gradients [10, 11].

However, the acquired data show artifacts due to several sources of error, i.e. data quality needs to be improved before reliable hemodynamic information can be derived. Furthermore, since the PC-MRI data contain not only vessels of interest but also surrounding tissue and noise, the vessels need to be segmented before hemodynamic calculations.

The aim of the work described in this thesis was to develop and to test new strategies for preprocessing and analysis of time-resolved 3D PC-MRI (also referred to as 4D flow-sensitive MRI) data to provide an improved characterization of normal and pathologically altered 3D hemodynamics in the human aorta.

1.2 Main contributions

This thesis contains three parts:

1. Evaluation of new algorithms for the optimal 3D extraction of vessel morphology (= angiography) data from flow-sensitive 4D MRI. Additionally, 3D PC-MR angiography (PC-MRA) was compared with gold standard contrast-enhanced MRA (CE-MRA). As the PC-MRA has a poorer spatial resolution compared to CE-MRA, it is important to know to which extend the vascular geometry attained by PC-MRA reflects the actual dimensions of the vessels. In addition, the influence of different contrast agents on the PC-MRA were investigated.
2. An approach was developed to obtain 4D vessel geometry. 4D PC-MRA is important since the aorta, especially the ascending aorta, moves and deforms during the cardiac cycle, i.e. by using rigid segmentation this motion is lost. Additionally, rigid segmentation may increase the error in the calculation of hemodynamic parameters. First, it was shown that underestimation of vessel lumen leads to 20-30% overestimation of cycle-averaged velocities [12]. Second, if using 4D segmentation the incorporation of the noisy values from outside the vessel is reduced compared to the method of rigid segmentation, thus leading to more accurate hemodynamic values.
3. PC-MRA combined with time-resolved 3D velocity data was used to derive and to analyze pressure gradients in the aorta. Pressure gradients are an important clinical marker for the severity of cardiovascular disease such as aortic valve stenosis and aortic coarctation [13, 14]. However, no systematic study including quantitative analysis and visualization of the spatial and temporal distribution of time-resolved 3D pressure differences in the human aorta has been presented to date. It was therefore the purpose of this study to evaluate the potential of an optimized data analysis strategy for the assessment of aortic pressure difference maps.

1.3 Thesis overview

The thesis is structured as follows: first, a general introduction covering the basics of anatomy (section 2.1), imaging and data acquisition techniques (sections 2.2 and 2.3) as well as vasculature segmentation techniques (sections 2.4-2.6) is presented. The next chapter provides an overview on the methods used for pre-processing of the PC-MRI data. The following chapters will cover the topics of this thesis: extraction and evaluation of 3D PC-MRA (chapter 4), the clustering approach for 4D vessel segmentation (chapter 5) as well as the derivation and analysis of time-resolved 3D pressure differ-

ences (chapter 6). Subsequently, the main results of all thesis topics are summarized and discussed in chapter 7.

2 Background and Theory

This chapter provides the background relevant for this work. First, the anatomy and physiology of the heart and the vessels are described in section 2.1; sections 2.2 and 2.3 give insight into the imaging techniques and data acquisition strategies relevant for this thesis. Finally the most common vasculature segmentation techniques are presented in sections 2.4 and 2.5.

2.1 The cardiovascular system

The work presented here focuses on the largest blood vessel, the aorta, and in particular on its anatomy and flow characteristics. In the following section, major components and the functioning of the human cardiovascular circulation are described. Secondly, more detailed information on the aortic anatomy and function is provided as well as aortic diseases relevant for this work are presented.

2.1.1 Cardiovascular circulation

The main components of the cardiovascular system are the heart, blood vessels and blood. The human cardiovascular system is closed, i.e. the blood never leaves the blood vessels' network. The blood carries essential substances such as oxygen and nutrients to all body cells and transports back carbon dioxide and other waste products. The arteries are the vessels, where the blood is transported away from the heart, and the veins are the vessels carrying the blood back to the heart. The vessels at the interface of arteries and veins are called capillaries. They enable the interchange of oxygen, nutrients and carbon dioxide between blood and surrounding tissue [16].
As depicted in figure 2.1, cardiovascular circulation consists of two loops connected through the heart. One loop is the pulmonary circulation where deoxygenated blood is transported away from the right side of the heart to the lungs and then the oxygenated blood back to the heart. The second loop is the systemic circulation which distributes the oxygenated blood to the body and returns deoxygenated blood back to the heart.

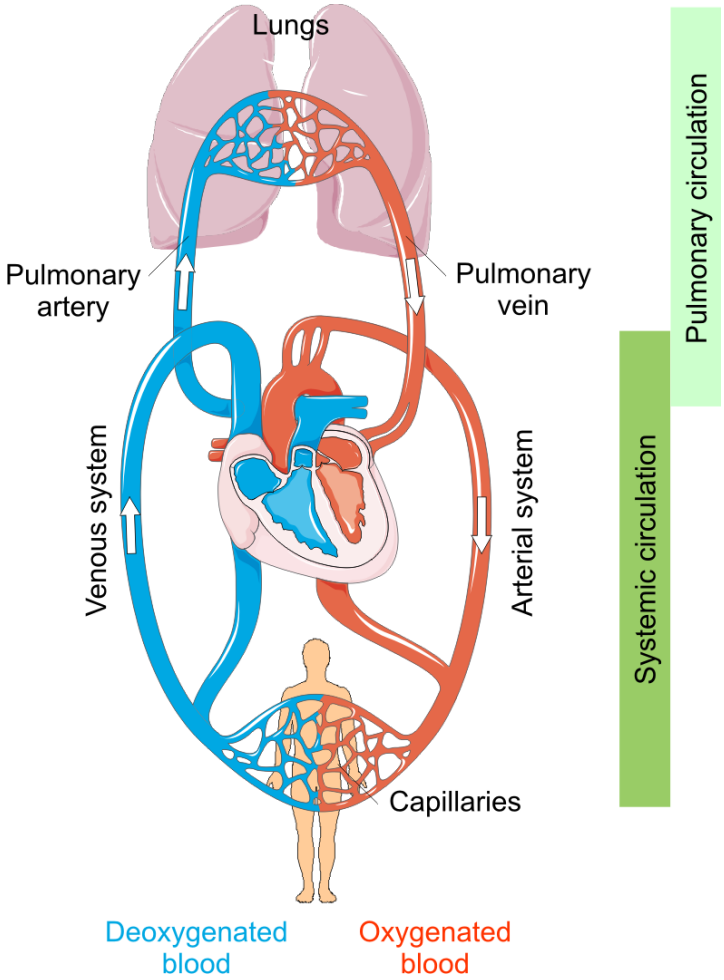

Figure 2.1: *The circulatory system includes the pulmonary and the systemic circulations. The systemic circulation transports blood from the heart to the organs and returns deoxygenated blood back to the heart. The pulmonary circulation carries deoxygenated blood from the heart to the lungs and oxygenated blood back to the heart.* (This figure was produced using Servier Medical Art [15].)

In terms of the length of the circulation, pulmonary circulation is much shorter than the systemic one.

2.1.1.1 Heart

Anatomy

As illustrated in figure 2.2, the heart is a four-chambered organ, divided into a left and a right half by the cardiac septum. Each of the halves is further divided into atrium (upper part) and ventricle (lower part). Deoxygenated blood is conducted via the right atrium (RA) into the right ventricle (RV) and then pumped into the pulmonary system through the pulmonary artery (PA). After oxygenation, the blood returns to the left

atrium (LA) via the pulmonary veins and passes into the left ventricle (LV), from where the blood is transported by the aorta (Ao) into the systemic circulation.
The blood flow within the heart is regulated by a valve system which ensures forward flow only. Atria and ventricles are separated by atrioventricular valves (mitral/bicuspid and tricuspid valves for the left and the right side, respectively). The two semilunar valves, located at the arteries leaving the heart, are the aortic valve and the pulmonary valve.

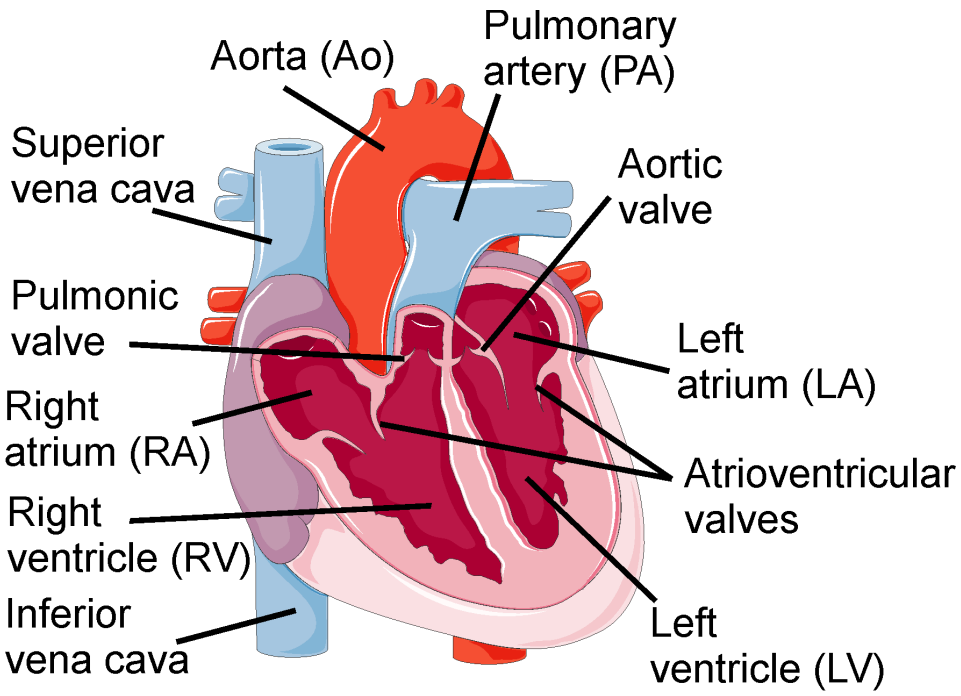

Figure 2.2: *Schematic representation of the anatomy of the human heart with the heart chambers, heart valves and adjacent vascular system.* (This figure was produced using Servier Medical Art [15].)

Cardiac cycle

The cardiac cycle comprises rhythmic muscular contractions of the heart. Each contraction (= heartbeat) can be subdivided into two major phases: *systole* and *diastole*. In systole, the ventricles contract, the intra-ventricular blood volume is compressed and as soon as the closing pressure of the semilunar valves is exceeded the blood is ejected into the pulmonary artery and the aorta. In diastole, the ventricles are relaxing and the heart fills with blood (figure 2.3 A). The frequency of the cardiac cycle is called the heart rate. At rest, the heart beat ranges from 50 to 100 beats per minute (bmp) in a healthy person. Due to the periodic contractions of the heart, blood flow shows a pulsatile temporal waveform.

This pumping motion can be recorded by detecting the temporal electrical activity of the heart tissue by an electrocardiogram (ECG)[17]. The recorded voltage curve shows a characteristic structure with spikes and waves. These are labeled with letters P, Q, R, S and T (see figure 2.3 B). The R-wave is the most distinct characteristic of the ECG course and marks the beginning of the systole. Therefore, the R-wave is used as a trigger for the synchronization of cardiovascular MRI measurements with cardiac cycle.

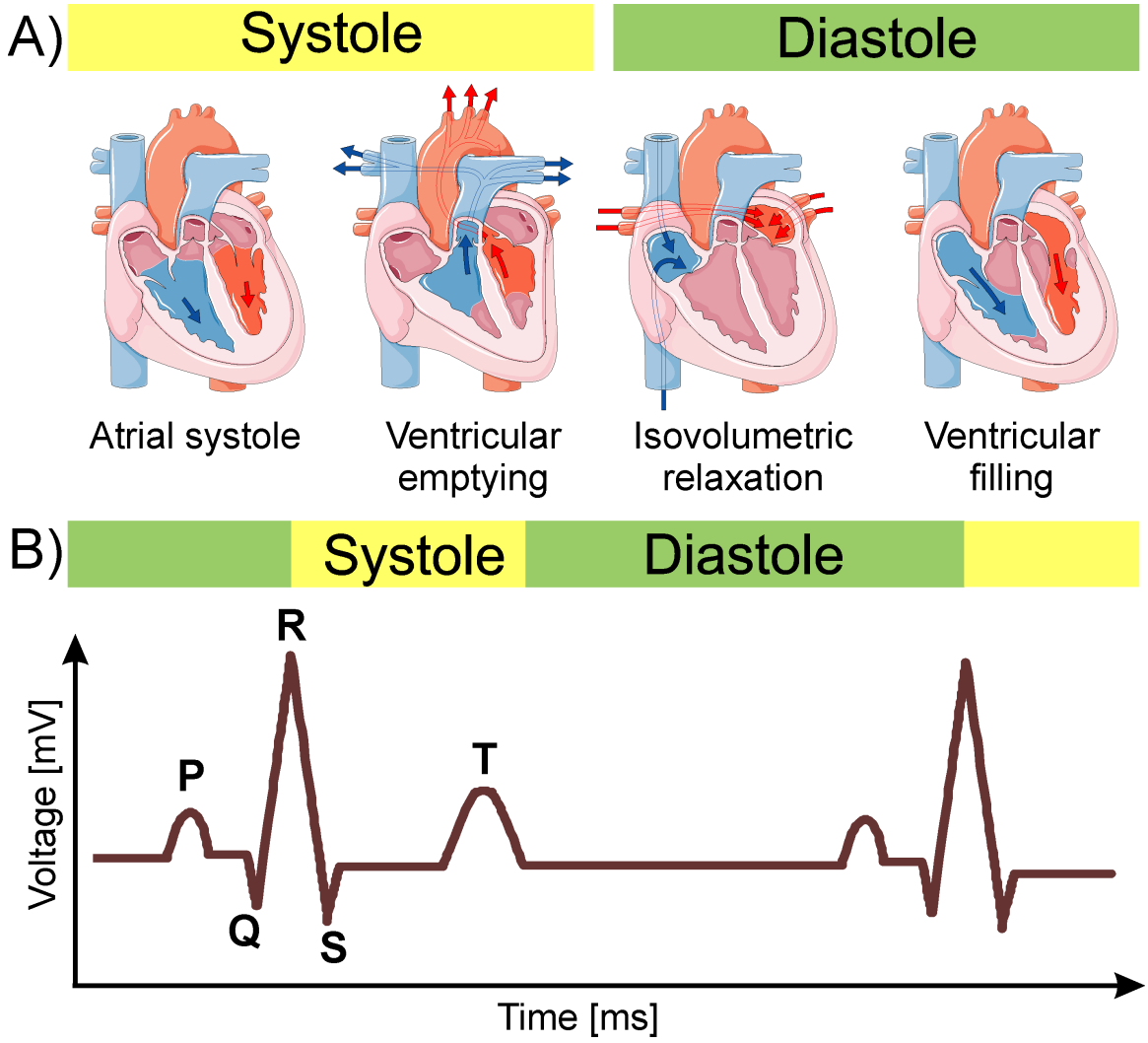

Figure 2.3: *Different cardiac phases (A) and their temporal allocation in the ECG (B) of a healthy heart. At the beginning of cardiac activity (R-wave), the ventricles are filled with blood, which is ejected during the contraction of the ventricles into the arteries. In the diastolic phase (filling phase), the blood flows through the atria into the ventricles, from where it is ejected in the subsequent systole back into the vascular system.* (This figure was produced using Servier Medical Art [15].)

2.1.1.2 Blood vessels

The blood vessels transport the blood throughout the body. Blood vessels can be subdivided into three major types:

- the arteries, which conduct blood from the heart to the peripheral organs;
- the capillaries - these micro vessels enable the exchange of essential nutrients between blood and surrounding tissues;
- the veins, which transport the blood towards the heart.

The blood flow is pulsatile in the arteries and is relatively constant in the veins.

Aorta

The aorta is the largest artery in the body, originating in the left ventricle at the aortic valve and extending down to the abdomen (figure 2.4 A). The aorta is divided into three segments:

- the ascending aorta (AAo) is the segment between the heart and the aortic arch;
- the aortic arch (AA) represents the curved portion at the top of the aorta, where supra-aortic branches originate, supplying head and arms with blood;
- the descending aorta (DAo) is the section beginning at the aortic arch and running down to the legs where it branches. The sections above and below the diaphragm are the thoracic aorta and the abdominal aorta, respectively.

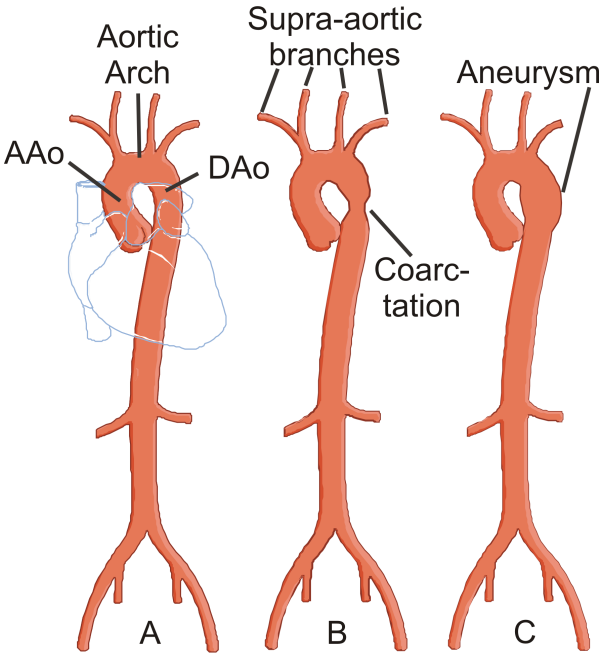

Figure 2.4: *A) Healthy human aorta with segments: ascending aorta (AAo), aortic arch, descending aorta (DAo); B) Aorta with coarctation (stenotic narrowing in descending aorta); C) Aorta with aneurysm.*

Like all arteries, the aorta has a three layer wall structure:

- Tunica intima is the innermost layer, which provides a smooth surface for blood to flow across.

- Tunica media is the middle layer and consist of muscle and elastic fibers, allowing the aorta to expand and contract with each heartbeat.
- Tunica externa is the outermost layer, providing additional stability to the aorta.

The aorta is an elastic artery with a wall that is thicker by factor 1.5 than that of the other arteries [17]. Other characteristic parameters of a healthy human aorta are summarized in table 2.1. As a result of the pulsatile blood flow, the aorta deforms and moves, especially the ascending aorta. The AAo undergoes a diameter change of 0.22 cm [18] resulting in a change of cross-sectional area of ± 5.9% between systole and diastole [19].

Length	[cm]	30 - 40
Diameter	[mm]	20 - 35
Cross sectional area	[cm^2]	4
Mean pressure	[mmHg]	95 - 105
Mean velocity	[m/s]	1.0
Pulse wave velocity	[m/s]	5 - 6
Wall thickness	[mm]	2.5

Table 2.1: *Healthy human aorta in numbers* [20, 21].

2.1.1.3 Hemodynamic

In the systemic circulation, blood ejected from the left ventricle flows due to arterio-venous pressure difference (ΔP) back to the right atrium. The blood is distributed to the organs according to their regional resistance (R). This resistance is caused by the internal friction of the fluid. The relationship between resistance and pressure can be determined according to Ohm's Law:

$$R = \frac{\Delta P}{Q} \tag{2.1}$$

with Q being blood flow. The equation (2.1) applies for an organ as well as for the entire systemic circulation, where the resistance of the systemic circulation referred to as *total peripheral resistance* (TPR) with a normal value of 17.3 mmHg$\cdot$ $l^{-1}\cdot$ min (2.3 kPa $\cdot$ $l^{-1}\cdot$ min) [22]. To overcome this resistance, the left ventricle must produce an averaged pressure of 100 mmHg (13.3 kPa) in the aorta.
The heart ejects the blood intermittently, thereby the pressure in the left ventricle increases to 120 mmHg in the systole, and drops to a few mmHg in diastole (see figure 2.5). To avoid this high pressure drop and to ensure the continuous flow, aorta and large arteries have a so called *Windkessel* function. That means that due to the elasticity of the

large arteries, a part from the ejected stroke volume (= the volume of blood ejected from left ventricle with each heart beat) is retained during the systole and is continuously released during diastole. In this way, the blood pressure fluctuations over the cardiac cycle are alleviated [16]. The systolic pressure in the aorta and major arteries is about 120 mmHg (≈ 16 kPa), the diastolic - about 80 mmHg (≈ 11 kPa).
The resistance of pulmonary circulation is with 1.8 mmHg·l^{-1}· min (0.24 kPa· l^{-1}· min) only a small fraction of TPR, so that the right ventricle has to produce a significantly lower mean pressure (15 mmHg = 2 kPa) [22].
The intermittent action of the heart induces a (pressure) pulse wave that propagates along the arterial vessels with pulse wave velocity PWV. PWV in the normal healthy aorta is 3-5 m/s. The PWV is substantially higher than the blood flow velocity V in the same blood vessels. The central aortic pressure wave is composed of a forward-traveling wave generated by left ventricle and a time-shifted reflected wave from the periphery [23] (figure 2.5). The less flexible the vessel wall is, the higher is the velocity of both forward and reflected waves.
The temporal correlation of hemodynamic processes is illustrated in figure 2.5.

2.1.1.4 Blood

The human blood is a fluid, composed of blood cells (45%) suspended in the blood plasma (55%). The normal blood amount is about 7% of the fat-free body mass [16]. The main blood cells are the thrombocytes (platelets), leukocytes (white blood cells) and the erythrocytes (red blood cells). Although the blood cells are the reason for the non-Newtonian aspect of the blood flow, in the large arteries the blood viscosity can be assumed to be constant (viscosity = $3.2 \cdot 10^{-3}$ Pa·s) [24]. As a result, blood flow in large arteries, as considered in this work, can be reasonably assumed to have a Newtonian behavior.

2.1.2 Aortic diseases

There is a large number of aortic diseases, congenital or acquired. Below, only the vascular diseases relevant for this work are described.

2.1.2.1 Stenosis

A *stenosis* is a congenital or acquired abnormal narrowing in a blood vessel (figure 2.4 B). The severity of the stenosis is characterized by the degree of lumen (= inside space of the vessel) reduction and the pressure gradient (= difference in the level of blood

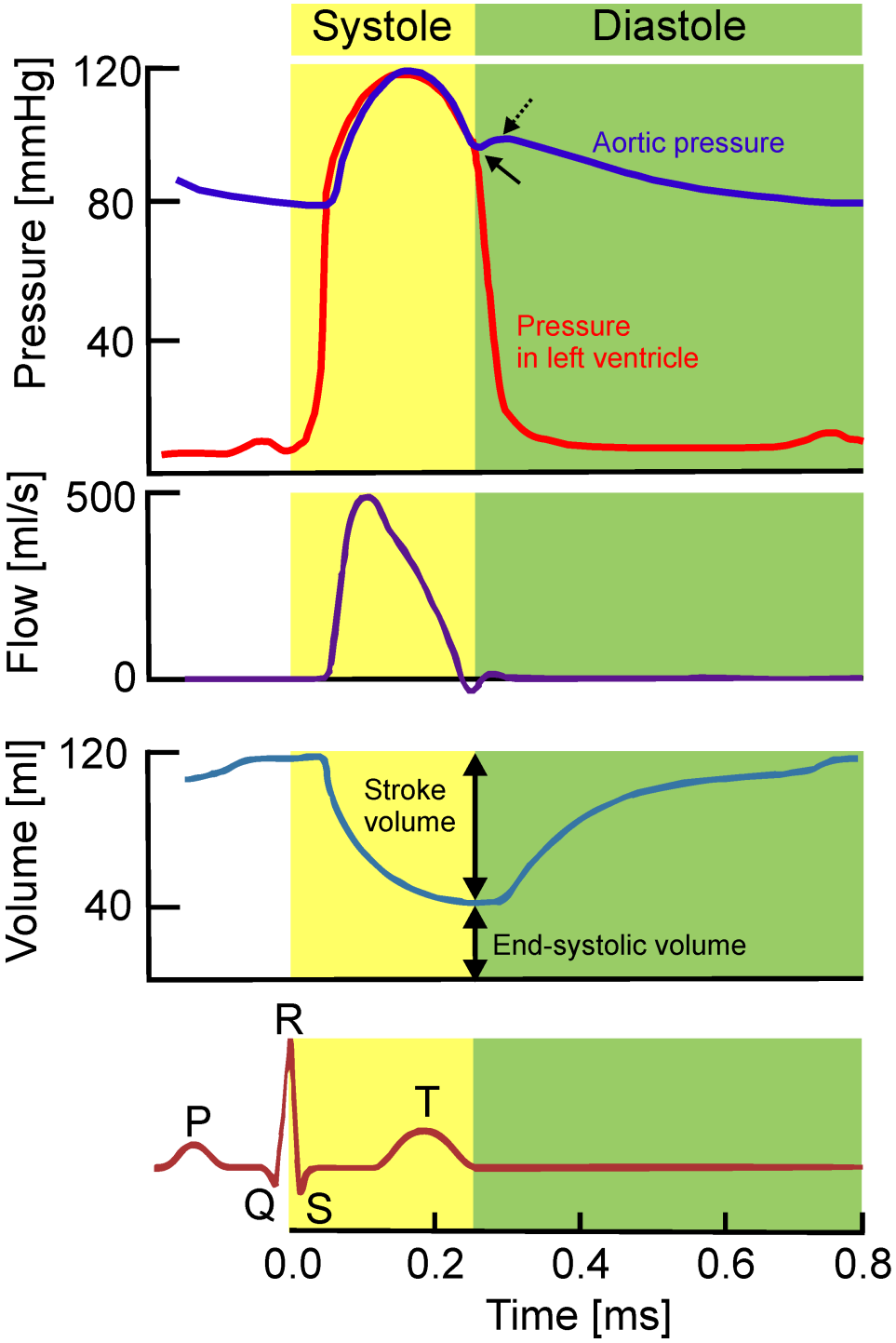

Figure 2.5: *Temporal correlation of pressure, flow, ventricle volume and ECG in systole and diastole (in resting state with a heart rate of 75 bmp). The solid arrow identifies the beginning of the reflected pressure wave, the dashed arrow indicates the peak of the reflected wave.* Figure was adapted from [22].

pressure) across the narrowing. Dependent on the severity, stenoses are treated by drugs, surgery, angioplasty or stenting.

Aortic valve stenosis

Aortic valve stenosis (short aortic stenosis) is a congenital or acquired narrowing of the aortic valve, resulting in an inadequate pumping of the blood and thus an increase of the left ventricular pressure. In an early stage, the ventricle maintain the pressure by wall thickening (hypertrophy). In the later stage, the ventricle dilates resulting in a thinner wall and impaired systolic function. Aortic valve stenosis can be treated by aortic valve repair or replacement.

Aortic coarctation

If the origin of an aortic stenosis is congenital and the narrowing is located in the proximal descending aorta, it is named aortic coarctation and is encountered in approx. 0.1 % of newborns. This vessel malformation causes proximal hypertension and reduces distal blood flow. Coarctations can be treated by surgical repair, balloon dilation or stent.

2.1.2.2 Aneurysm

In contrast to a stenosis, an aneurysm is an abnormal dilatation of blood vessels as a result of congenital or acquired vessel wall changes [25]. Causes of aneurysms are degenerative vascular diseases, infections, inflammations or connective tissue disorders. Aneurysms commonly occur in the thoracic (figure 2.4 C) and abdominal aorta or in the brain. When the diameter of an aneurysm increases beyond 4.5-5 cm, there is a significant risk of rupture, resulting in severe hemorrhage and sudden death. Aortic aneurysms are treated surgically by replacing the section of the vessel by a graft.

2.1.2.3 Atherosclerosis

Atherosclerosis is the cause of more than half of all deaths in Western industrialized nations [2]. It is a slowly progressive disease of the arteries, in which the intima is thickened as a result of the accumulation of fatty materials. These increasingly constrict the lumen. In the course of the disease, fibrous plaques form. These plaques are accumulations of macrophages, tissue debris and cholesterol crystals. Most common sites of plaques are the carotid arteries, coronary arteries and the descending thoracic aorta. The major modifiable risk factors are diabetes, hyperlipidemia, hypertension and smoking. Non-modifiable risk factors are advanced age, male gender and genetic abnor-

malities [2].
The consequences of plaque formation is a narrowing of the lumen, which can lead to ischemia, a stiffening of the vessel wall (calcification), the formation of thrombi, which can obstruct the residual lumen and cause peripheral embolism (e.g. stroke) or myocardial infarction (heart attack), and bleeding into the plaques and into the vessel wall [2]. If the vessel wall is damaged, it can rupture, so life threatening dangerous bleeding may occur.
Several studies show association between atherosclerosis and arterial stiffness [5]. One possible explanation is that the presence of atherosclerosis leads to stiffening of the arteries and increase in PWV [26]. Another reason might be that due to increased stiffness in elder the arteries could not well absorb the pulsatile pressure, which may lead to increased stress of the vessel wall and eventually lead to vessel wall damage and atherosclerosis [5].
Atherosclerosis is treated by dietary changes, drugs or stenting.

2.2 Cardiovascular imaging

The focus of this work is on the cardiovascular magnetic resonance imaging (MRI) data. MR imaging in general and the specific cardiovascular MR data acquisition techniques are described in detail in the subsequent sections. In addition, since echocardiography data also has been used, this method is explained as well. Other important cardiovascular imaging methods are briefly summarized and their use in cardiovascular diagnostics is described.

2.2.1 Imaging techniques

For the clinical diagnostics of cardiovascular diseases, several invasive and non-invasive cardiovascular imaging techniques are available. Catheter angiography is an invasive approach, meaning that this procedure involves penetrating of skin or body cavities. All other methods such as Doppler ultrasound (echocardiography), computed tomography (CT), single-proton-emission CT (SPECT), positron-emission tomography (PET) and MRI are non-invasive.

2.2.1.1 Catheter angiography

Catheter angiography is an X-ray-based technique for vessel imaging. For examination of the arterial vessels, the catheter is inserted through the femoral artery (a large artery in the thigh) and is guided to the vessel of interest, where a contrast agent (here iodine-containing substance) is injected into the vessel resulting in a higher absorption of X-rays in the blood vessels compared to surrounding tissue [27].
For the so-called Digital Subtraction Angiography (*DSA*), two X-ray images are acquired, one without and one with a contrast medium. Subtraction of these images enables visualization of the vessels flooded by the contrast agent (see figure 2.6).
Due to the high spatial and temporal resolution, DSA is a gold standard technique for detection and investigation of stenoses, especially in the coronary vessels (vessels supplying the heart). Furthermore, one can apply the catheter to measure pressure in vessels and cardiac chambers. Coarctation of large vessels can be quantified by measuring pressure proximal and distal of the pathology [28] and calculating the pressure gradient across the constriction. These catheter measurements are reference standard technique for pressure gradient determination.
The disadvantages of the technique are high invasiveness and radiation exposure of the patient.

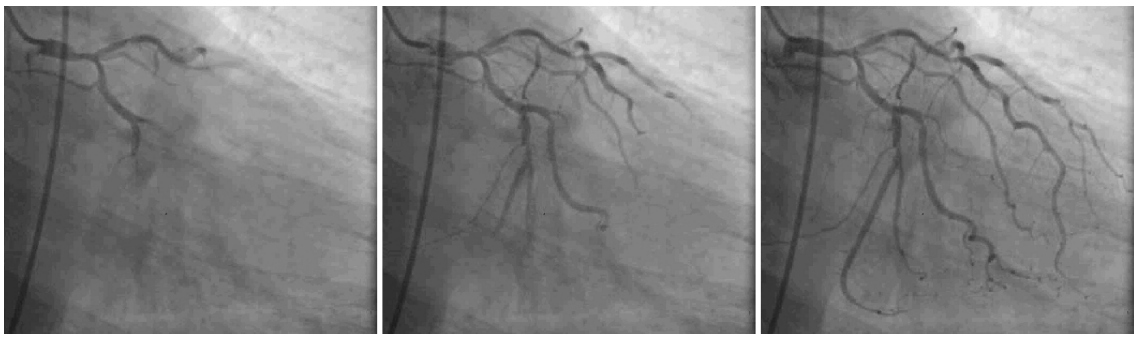

Figure 2.6: *DSA at three stages of inflow of contrast agent into a healthy coronary vasculature.* Image is courtesy of Dr. Bernd Jung, University Medical Center, Freiburg.

2.2.1.2 Computed tomography

Computed tomography (CT) is a projective X-ray imaging technique. A narrow X-ray beam and an opposed linear detector array are swept around the patient. Tomographic images are generated through a computer-based analysis from a series of projections obtained at different orientations [29]. Major advantages are high spatial resolution with isotropic voxels and extremely short scan times resulting in a rapid examination. The radiation dose and use of iodine contrast agents are the main drawbacks of this technique.

Applications of CT in vascular diagnostics include the assessment of coronary vessel calcification which can be used as predictive value for coronary events [30]. Furthermore, CT can be deployed for plaque differentiation (vulnerable or stable) in atherosclerosis [31]. Due to high spatial resolution, CT angiography is a well established technique, especially for the coronary vessels (figure 2.7).

Figure 2.7: *CT acquisition of the left and right coronary arteries. A stenosis can be clearly seen in the central region of the right coronary artery (thick white arrow).* Image is courtesy of Dr. Bernd Jung, University Medical Center, Freiburg.

2.2.1.3 Nuclear imaging with SPECT and PET

In both techniques (SPECT and PET), a radio-pharmaceutical is used.
In SPECT, the used radionuclide emits γ-radiation, that is detected using gamma-cameras which rotate around the patient. SPECT images show the distribution of the administered radiopharmaceutical in the body, allowing to assess the function of various organs [27].
In contrast to SPECT, PET uses radionuclides (such as fluorodeoxyglucose $^{18}F-FDG$ or N13-Ammonia $^{13}N-NH_3$) that emit positrons (β^+ decay). If one of these positrons annihilates with an electron, two high energy (γ) photons moving in opposite directions are produced and can be detected. By using computer analysis, images of radionuclide concentration within the body are reconstructed [27]. The advantage of nuclear

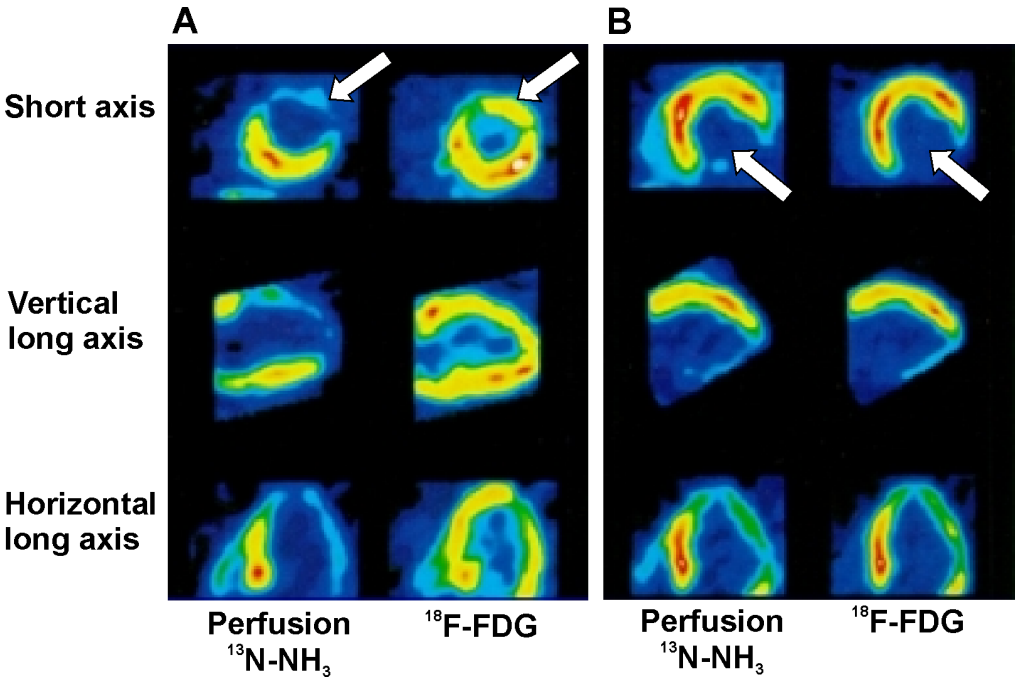

Figure 2.8: *PET scans of perfusion and metabolic activity of two patients after infarction. A)Patient with low perfusion but viable heart muscle; B) patient with necrotic scar tissue (see arrows).* Figure is courtesy of Dr. Bernd Jung, University Medical Center, Freiburg.

imaging is the ability to measure metabolic and physiologic processes [32]. Applications of SPECT and PET imaging include the evaluation of plaque vulnerability in the atherosclerosis as well as the assessment of the perfusion and the metabolic activity of the heart muscle in the ischemic heart disease.
Disadvantages of PET and SPECT compared to MRI are the inferior spatial resolution and radiation dose.

2.2.2 Echocardiography

Echocardiography is a cardiac imaging technique using ultrasound waves. Ultrasound is sound with a frequency above the upper limit of human hearing (> 20 kHz)[33]. Ultrasound frequencies used in medical applications are in the range of 1 MHz to 40 MHz [34].
The sound waves propagate at different speed in different tissues (blood 1570 m/s, fat 1460 m/s, bone 3500 m/s). Whenever a sound wave travels across an interface of tissues of different densities (acoustic impedance), the wave is partially reflected. This reflection is called an echo. The larger the difference in acoustic impedance is, the stronger is the produced echo. By evaluating the transit time and the intensity of the echo, the depth of the tissue interface causing the echo can be calculated. Additionally, the echo intensity is converted to gray value: strong echoes appear white and weaker echoes gray on the ultrasound image. The gray scale is determined by Hounsfield units.
Main applications of the echocardiography are the assessment of the anatomy and ventricular function as well as for the diagnosis of valve stenosis and insufficiency.

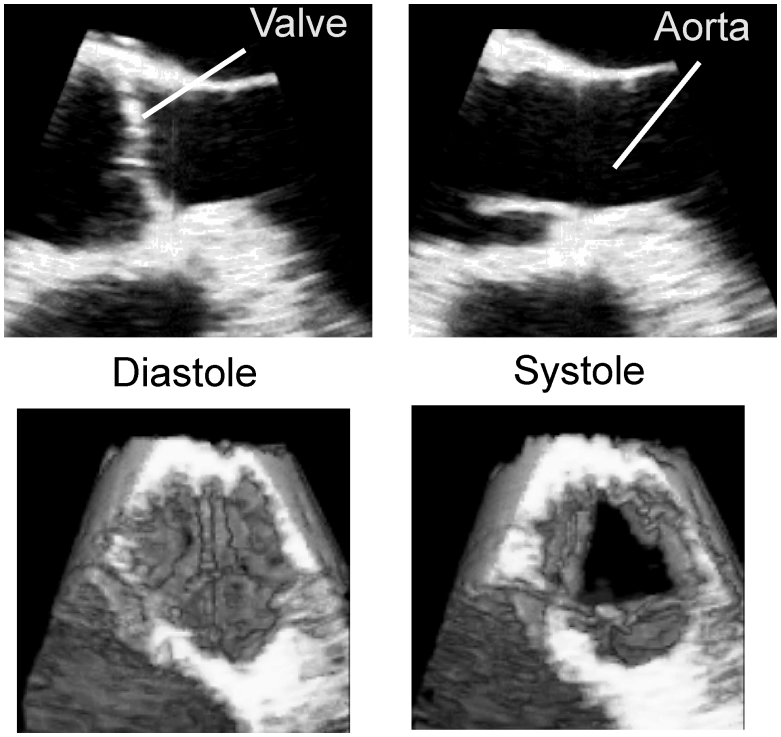

Figure 2.9: *Time-resolved 3D-ultrasound image of the aortic valve. The upper row shows two single time frames of the valve motion. The lower row displays the corresponding 3D surface reconstructions. Images on the left represent the closed valve in the beginning of the cardiac cycle, images on the right depict the open valve during the ejection phase.* Figure is courtesy of Dr. Bernd Jung, University Medical Center, Freiburg.

Doppler echocardiography

The *Doppler echocardiography* is based on the Doppler effect/Doppler shift. This effect describes a phenomenon where a sound source (moving towards the observer or away) induces a frequency shift, which depends on the speed and direction of the sound source. The Doppler shift can be positive (increase in frequency = approaching of the sound source) or negative (decrease in frequency = recession of the sound source).
In the Doppler echocardiography, ultrasound waves are emitted at a certain frequency into the tissue. These sound waves are then reflected from the moving blood cells. The reflected sound waves are received back from the transducer. The received sound waves undergo a frequency change which is directly related to the flow direction and velocity of the blood cells [35].
Blood flow velocity can be calculated using the Doppler equation:

$$\Delta F = 2\, F_0\, \frac{V}{C}\, \cos\alpha, \tag{2.2}$$

where Δ F is the Doppler shift, F_0 is the emitted frequency, V blood flow velocity, C is speed of sound ($\approx$1540 m/s in soft tissue), α is angle between ultrasound and blood flow. Example of Doppler echocardiography is shown in figure 2.10.
As evident from the equation 2.2, the Doppler shift depends crucially on the angle between blood flow and the sound field. This angle dependency makes the echocardiography operator dependent and less reproducible.

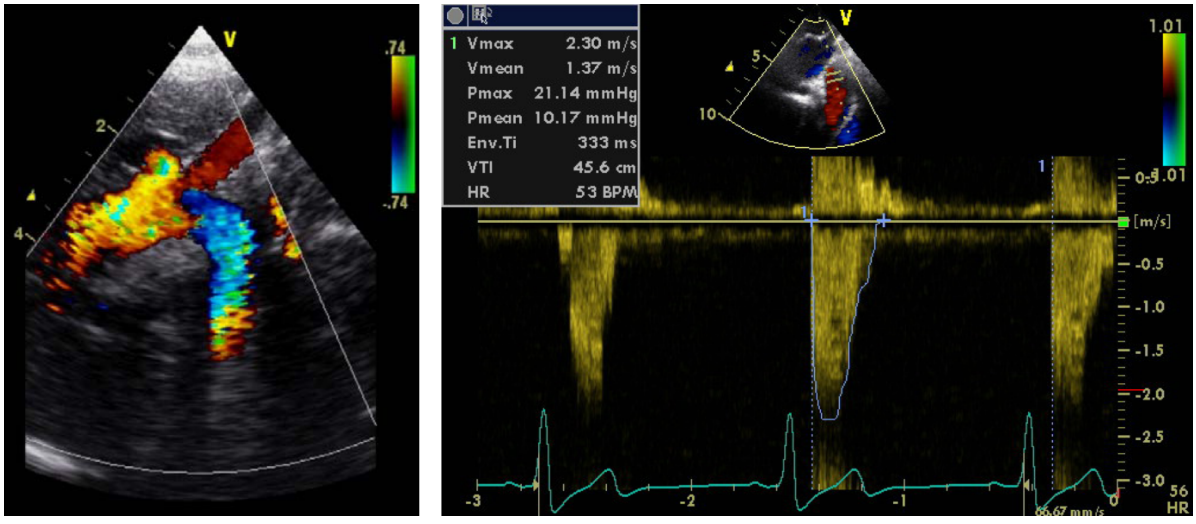

Figure 2.10: *Left image: color Doppler echocardiography of the aorta. Right image: Doppler measurement of maximal and mean velocity and pressure in the aorta.* Figure is courtesy of Dr. Daniel Hirtler, University Medical Center, Freiburg.

Further general limitations of echocardiography are variable image quality due to lung disease, chest configuration or obesity, and the reads from echocardiography tend to be more qualitative than quantitative. The advantages are that the machines are portable, the costs are relatively low with a high patient's throughput. Furthermore, it is a radiation-free technique and no contrast agent needs to be used.
Applications of ultrasound in cardiovascular diagnostics include the evaluation of occlusions in neck arteries, assessment of valve morphology (figure 2.9) and function, as well as fast pressure gradient estimation in coarctation (see section 6) [36].

2.2.3 General principles of MR imaging

In medical diagnostics, the phenomenon of nuclear magnetic resonance is used to non-invasively obtain images from the inside of the body. The principles of magnetic resonance imaging (MRI), the required hardware and the generation of the MR images, in particular imaging of the cardiovascular system, are explained below.

2.2.3.1 Spin and magnetization

Nuclear magnetic resonance (NMR) and magnetic resonance imaging (MRI) are based on the magnetic properties of atomic nuclei with odd mass number (= sum of protons and neutrons) or odd atomic number (= number of protons). An exact characterization of the NMR process requires a quantum-mechanical description. Since it is beyond the scope of this work to describe the quantum physics of NMR, a semi-classical description is sufficient for understanding the basic physics of NMR.
In this work, MRI is based on the hydrogen atom due to its high abundance given the approximate 70% water (H_2O) content of the human body. The hydrogen atom (^1H) consists of an electron and a nucleus with a single proton. A proton has a nuclear spin $\vec{s}$. In the semiclassical picture, the electrical charge induces a magnetic moment $\vec{\mu}$ which is proportional to $\vec{s}$:

$$\vec{\mu} = \gamma \cdot \vec{s},$$

where γ is the gyromagnetic ratio ($\frac{\gamma}{2\pi} = \gamma^* = 42.58\ MHzT^{-1}$ for a proton).
In an external magnetic field $\vec{B}_0$, spins will align along the field, whereby this alignment can be parallel or antiparallel. According to the Boltzmann distribution, the number of parallel-oriented spins predominates slightly since this state is energetically favorable, and thus leads to a macroscopic longitudinal magnetization $\vec{M}_z$ along $\vec{B}_0$. Furthermore, the protons will respond with a precession of $\vec{M}$ around $\vec{B}$ at a characteristic frequency, the so-called *Larmor frequency* ω_L, thereby ω_L is proportional to the magnetic field strength:

$$\omega_L = \gamma^*\, B_0. \tag{2.3}$$

The creation of the magnetic resonance signal is based on bringing a component of the longitudinal magnetization vector into the transverse plane, which is achieved by applying a radio-frequency (RF) pulse at the Larmor resonance frequency ω_L [8]. Dependent on the duration and the amplitude of the RF-pulse, the magnetization is deflected from its equilibrium state (i.e. directed along $\vec{B}_0$) by an angle (flip angle α, see figure 2.11). The magnetization now consists of two components: a longitudinal component M_z parallel to the magnetic field B_0 and a transverse component M_{xy} perpendicular to the

magnetic field and rotating with the Larmor frequency around the B_0 axis. The rotating transversal magnetization can be detected by placing a signal receiving device (=receiver coil) around the object under investigation. The precession of M_{xy} induces in the receiver coil a measurable electrical voltage, called the free-induction decay (FID).

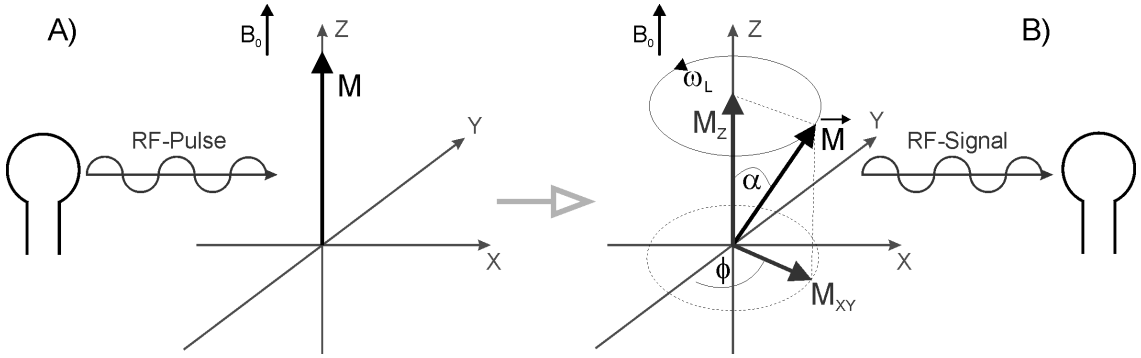

Figure 2.11: *After RF-pulse application, the magnetization $\vec{M}$ is tilted by the flip angle α from the equilibrium along B_0 direction and precesses with the Larmor frequency ω_L about the z-axis, parallel to B_0. M_z is the longitudinal and M_{xy} is the transverse component of the magnetization $\vec{M}$.*

2.2.3.2 Relaxation processes

After the application of an RF-pulse, two independent and simultaneous relaxation processes cause a decrease of transversal magnetization and thus decrease the MR signal. The *longitudinal relaxation* refers to the process of returning to equilibrium of the longitudinal magnetization after excitation, due to the energy exchange between the spins and surrounding environment (spin-lattice relaxation). The duration of this process is tissue specific and characterized by the longitudinal relaxation time T_1. After time T_1 has elapsed, the longitudinal magnetization $M_z(t)$ has grown back to approx. 63 % of its initial value (figure 2.12). In the case of $M_z(0) = 0$, the subsequent recovery of M_z is given by [37]:

$$M_z(t) = M_0 \cdot (1 - e^{-t/T_1}), \tag{2.4}$$

where M_0 is the original magnetization.
The second relaxation process, the *transverse relaxation*, has its origin in the interaction of the spins with each other and the magnetic properties of their environment. The magnetic moments of neighboring spins trigger magnetic field fluctuations. Through these field inhomogeneities, Larmor frequencies of spins differ slightly, so that the spins lose their phase coherence. The dephasing of the spins causes the decrease of the transversal

magnetization. The duration of this process is described by the time constant T_2, after that the transverse magnetization $M_{xy}(t)$ has decreased to about 37% of its initial value (see equation (2.5) and figure 2.12):

$$M_{xy}(t) = M_{xy}(0) \cdot e^{-t/T_2}. \tag{2.5}$$

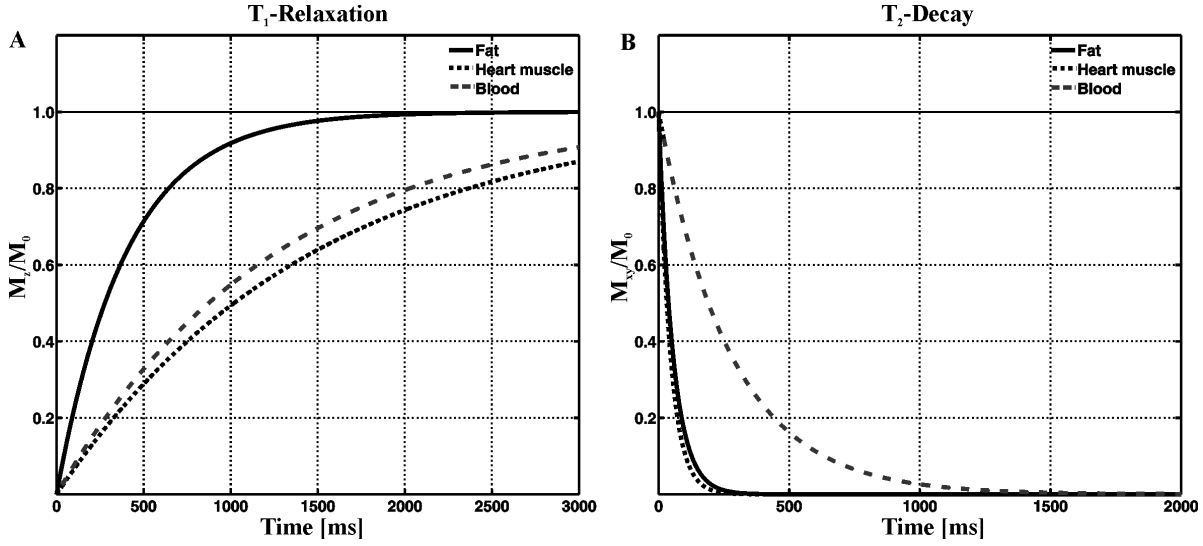

Figure 2.12: *Relaxation curves after 90° RF excitation pulse for different tissue components.* A: *T_1-relaxation of the longitudinal magnetization M_z;* B: *T_2-decay of transverse magnetization M_{xy}.*

In reality, the dephasing is even more pronounced due to external field inhomogeneities, leading to the effective transversal relaxation time T_2^* (whereby $T_2^* < T_2$):

$$\frac{1}{T_2^*} = \frac{1}{T_2} + \frac{1}{T_2'}, \tag{2.6}$$

where T_2 is related to non-reversible spin-spin relaxation and T_2' refers to reversible relaxation due to static field inhomogeneities.
The two constants T_1 and T_2 are tissue-specific, where usually $T_1 > T_2$. These relaxation times can be used in MR imaging to generate different tissue contrasts in the images. Approximate relaxation times at a main field of 3T are summarized in table 2.2.

Tissue	T_1 [ms]	T_2 [ms]
Blood	1550	275
Heart muscle	1470	45
Fat	400	55

Table 2.2: *Approximate T_1 and T_2 relaxation times at a main field of 3T* [38, 39].

2.2.3.3 Signal generation

As described above, the MR signal (FID signal) decays exponentially after the RF excitation with the relaxation time T_2^*. If the constant $T_2^{'}$ is sufficiently small, so that $T_2^{'} << T_2$, a severe signal loss may result [37]. But it is possible to gain the signal back by generating an echo.

Spin echo

The spin echo approach reverses the T_2^* dephasing of the spins by using an additional 180° RF pulse (inversion pulse) after the initial 90° pulse (see figure 2.13 A) [40, 41].
After the 90° RF-pulse, the spins are dephasing in the transverse plane. Two spins with precession frequency difference $\Delta\omega$ will have a phase difference of $\Delta\phi = \Delta\omega \cdot \tau$ after a time interval τ. By applying a 180° RF-pulse, all spins are flipped resulting in an inversion of the phase difference between two spins: $\Delta\phi = -\Delta\omega \cdot \tau$. Since the 180° RF-pulse does not change the precessing frequency of the individual spins, spins will be rephased ($\Delta\phi = 0$) after the time 2τ and form the so-called spin echo (SE). The time period between the initial pulse and maximum echo is referred to as echo time TE, here $TE = 2\tau$ [40].
The 180° inversion pulse removes the effect of T_2^* relaxation, so that the amplitude of the spin echo at TE is influenced by T_2 relaxation only [42] (see figure 2.13 A).

Gradient echo

Another approach to generate an echo is to spatially modify the magnetic field directly after the RF-pulse [43]. This field modification is referred to as *gradient* (G), meaning that the field amplitude is increasing along one spatial direction and decreasing along the opposing spatial direction. The application of a gradient results in different precession frequencies of the spins along the changing field.
A gradient applied directly after the RF pulse will result in faster dephasing of the spins as under normal conditions. Reversing the polarity of the gradient will result in a rephasing of the spins, and thereby produce an echo during the rephasing. This echo is referred to as gradient echo. The amplitude of the gradient echo at TE is influenced by T_2^* relaxation (see figure 2.13 B).

2.2.3.4 Localization and sampling of MR signal

In an MR-examination, the proton distribution in the imaged object weighted by the tissue specific relaxation times is recorded. In order to produce an image, the assignment of the signal and its origin, referred to as spatial encoding, is necessary.

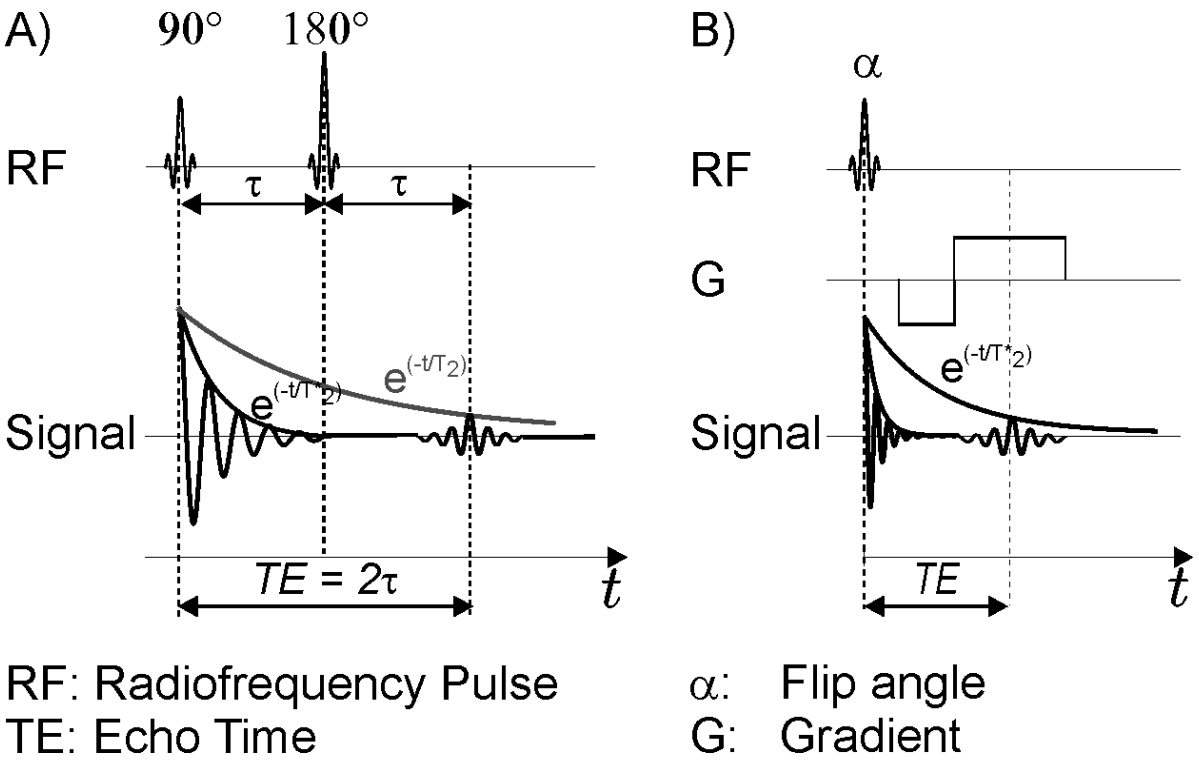

Figure 2.13: *A) Spin echo; B) Gradient echo.*

By the application of spatially and temporally variable gradient fields $\vec{G}$=(G_x, G_y, G_z) superimposing the static magnetic field, the Larmor frequency becomes spatially dependent:

$$\omega_L(\vec{r}) = \gamma B_0 + \gamma \vec{G}\,\vec{r}. \tag{2.7}$$

Using a suitable set of RF-pulses and gradient fields, object regions can be selected and spatially encoded. This set is called a pulse sequence.

Slice selection

For slice selection, a gradient (slice selection gradient $\vec{G_S}$) is applied simultaneously to the RF excitation. Thereby only the spins within a slice with a certain slice thickness Δz are excited:

$$\Delta z = \frac{\Delta\omega_{RF}}{\gamma \cdot G_S}, \tag{2.8}$$

where $G_S = \left|\vec{G_S}\right|$, $\Delta\omega_{RF}$ is the transmit bandwidth of the RF pulse (= range of frequencies) and γ is the gyromagnetic ratio.
The slice thickness is determined by the gradient slope (or strength): strong gradients are used for thinner slices as shown in figure 2.14. Slice position is determined by the frequency as illustrated in figure 2.15.

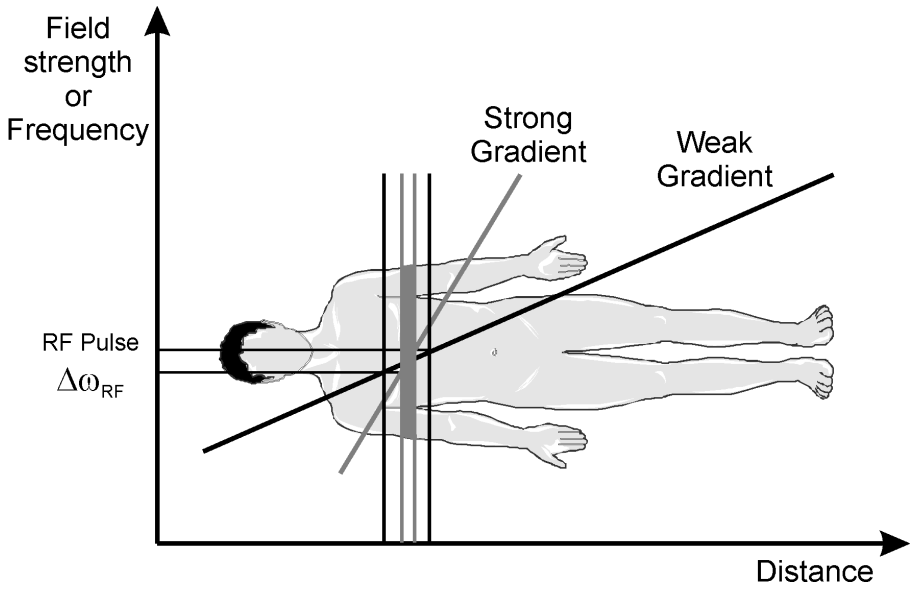

Figure 2.14: *Influence of the gradient on the slice thickness. Compared to a weaker gradient, the application of a stronger one results in a thinner slice for the same RF pulse.* Figure adapted from [44].

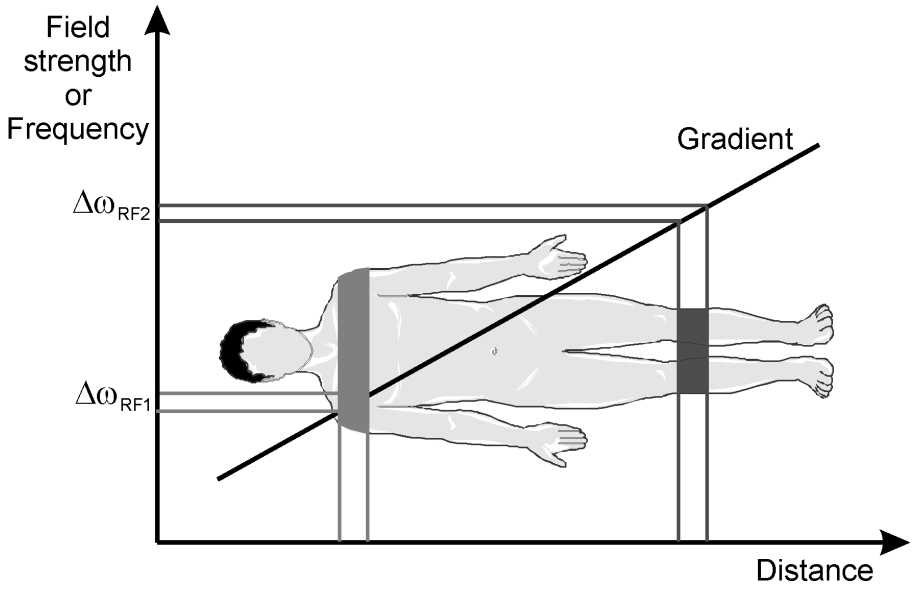

Figure 2.15: *Influence of the frequency on the slice position. For the same gradient strength, a higher frequency results in a different slice position compared to using the lower one.* Figure adapted from [44].

Phase encoding

Following the RF excitation and the slice selection gradient G_S, a phase encoding gradient G_P is applied, causing the spins to rotate at different frequencies according to their position along the gradient [42]. When the gradient G_P is switched off, the spins will have an additional gain of phase, which is dependent on their position along the gradient. The direction of G_P is referred to as phase encoding direction.

Frequency encoding

After the phase encoding gradient G_P, the frequency encoding gradient G_F is applied, whereby G_F is orthogonal to G_P and G_S. The applied gradient G_F causes the spins to rotate at different frequencies according to their position along this gradient [42]. During the application of the G_F gradient, the MR signal is read out. The direction of the frequency gradient is referred to as read-out direction.
For the full spatial encoding of the MR signal, phase encoding needs to be repeated with different gradient strengths. The number of phase encoding steps N_y is determined by the size of the selected measurement matrix $N_x \times N_y$. The time between two consecutive excitations is called repetition time TR. To measure an entire 3D volume and not only a 2D slice, a second phase encoding along the 3^{rd} dimension is necessary.

Signal sampling

In the sampling of MR signal, each phase encoding step acquires a line of the so-called k-space. The coordinates of k-space are the spatial frequencies k_x and k_y, where k represents the time integral of the applied encoding gradient starting at t_0:

$$\vec{k}\,(t) = \gamma \int_{t_0}^{t} \vec{G}\,(\tau)\; d\tau. \tag{2.9}$$

For Cartesian acquisition (as used in the presented work), the data points are stored line by line along the k_x direction. Each line represents a separately sampled MR signal. The position along k_x depends on the time point during the sampling period. The location of each line of data points in the k_y direction is determined by the amplitude and duration of the phase encoding direction at each phase encoding step [42] (see figure 2.16).
Application of the inverse Fourier transform (2D for a slice, 3D for a volume) converts the k-space signal S into the image (figure 2.16), thereby the signal S is defined as following:

$$\vec{S}\left(\vec{k}\right) \propto \int \rho\,(\vec{r})\; e^{-i2\pi\vec{k}\cdot\vec{r}}\, d\vec{r}, \tag{2.10}$$

where ρ is the spin density weighted by relaxation times. The k-space sampling rates

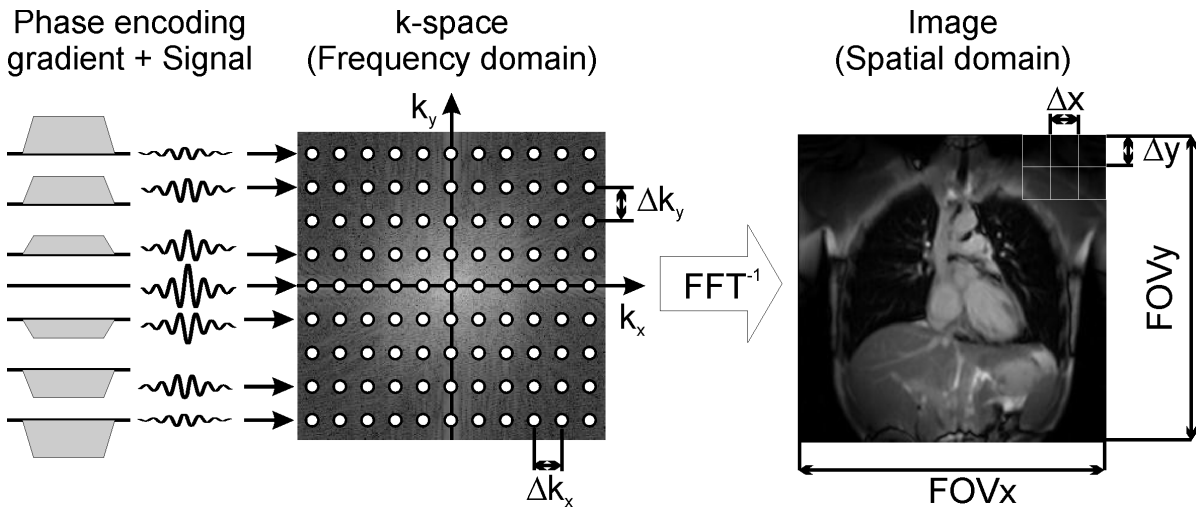

Figure 2.16: *By applying Fourier transformation, the raw data matrix (k-space) is converted to the image data matrix.*

Δk_x and Δk_y determine the maximum resolvable precession frequency, which in turn determines the spatial extent (*field of view, FOV*) and spatial resolution Δx and Δy of the image with a matrix size $N_x \times N_y$:

$$\Delta x = \frac{FOV_x}{N_x} = \frac{2\,\pi}{N_x\,\Delta k_x},$$

$$\Delta y = \frac{FOV_y}{N_y} = \frac{2\,\pi}{N_y\,\Delta k_y}.$$

Since the center of k-space contains low spatial frequencies, it contributes mostly to the contrast information; the edge of k-space represents the high spatial frequencies and thus contains information on fine details and edges [42, 44]. These k-space properties are demonstrated in figure 2.17.

2.2.3.5 Signal sampling schemes

Among numerous different signal sampling schemes, only gradient echo pulse sequence (*GRE*) relevant for this work is presented.
To fill the complete k-space, gradient echoes are generated in time intervals defined by the repetition time TR. Since no additional refocusing pulse is used, considerably shorter echo times TE can be realized compared to spin echo acquisition resulting in faster acquisition times. The acquisition time is:

$$T_{acq} = N_p \times TR,$$

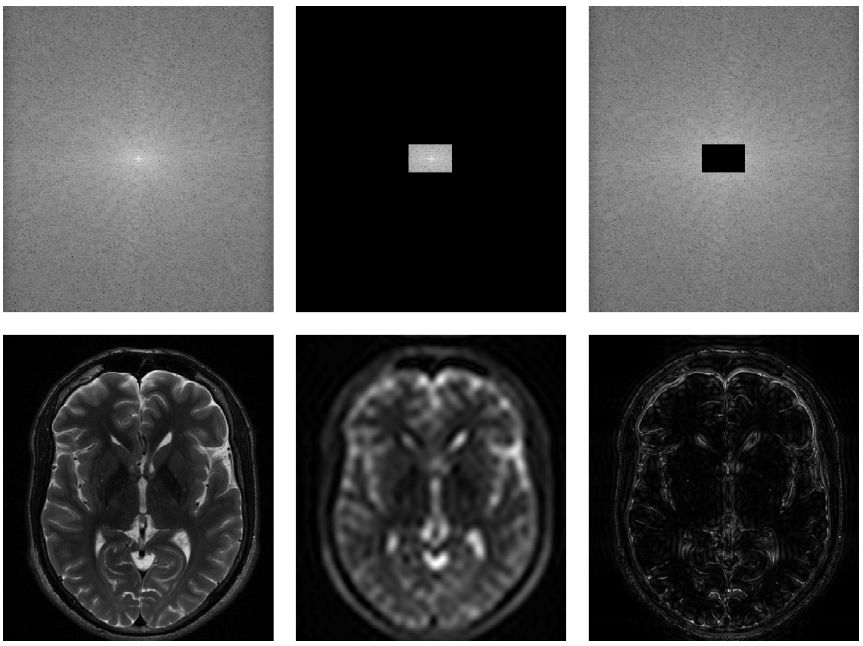

Figure 2.17: Top row: *measured k-space data in logarithmic scale. The original data* (left) *are limited to the center* (middle) *or the periphery* (right) *only.* Bottom row: *The reconstructed images using inverse Fourier transform: full k-space, low pass, high pass.* Image is courtesy of Dr. Matthias Weigel, University Medical Center, Freiburg.

where N_p is the number of phase encoding steps. The sequence diagram of GRE is illustrated in figure 2.18.

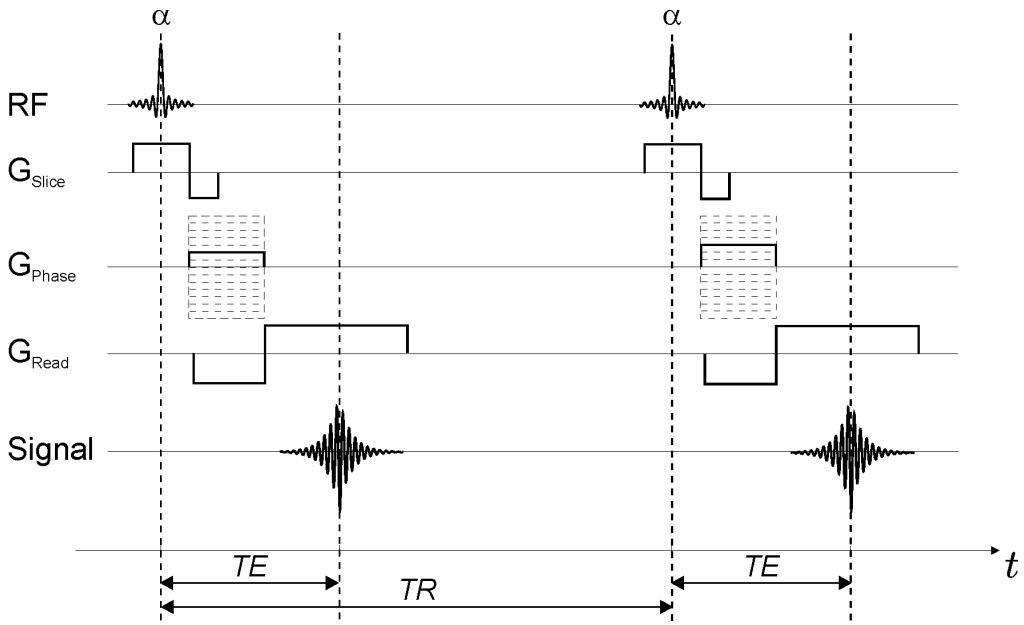

Figure 2.18: *Pulse sequence diagram for a 2D gradient echo sequence, showing two different phase encoding steps, which differ in the strength of the phase encoding gradient.* Image adapted from [45].

2.2.3.6 Modulation of the contrast

The image contrast produced with a *GRE* sequence, e.g. the influence of the relaxation times T_1 and T_2, can be modified by adjusting TE, TR and flip angle α [46].

TR >> T_2

If TR is selected to be significantly longer than T_2, then the transverse magnetization component M_{xy} is completely dephased prior to the RF-pulse and the longitudinal component M_z recovers with T_1. Each RF-pulse converts the existing longitudinal M_z into transversal magnetization M_{xy}. Depending on the tissue relaxation times, the longitudinal magnetization reaches an equilibrium state (*steady state*) after a sequence of RF-pulses with flip angle α.
Therefore the signal and available image contrast is dependent on T_1, TR and the flip angle α (see figure 2.19). A flip angle α, for which at a given TR and T_1, the steady state signal has its maximum, is called the Ernst angle (α_{Ernst}) [46]:

$$\alpha_{Ernst} = \arccos\left(e^{-TR/T_1}\right). \tag{2.11}$$

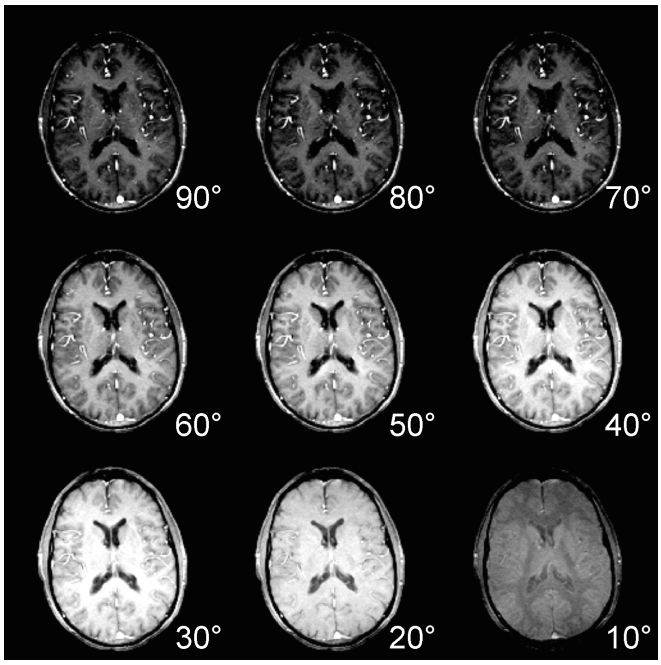

Figure 2.19: *Contrast behavior of GRE sequence applications with $TR >> T_2$ for different flip angles. Large and intermediate flip angles (upper and middle part) result in T_1 weighted images; for small angles the images are T_2^* or proton density weighted.* Figure is courtesy of Prof. Michael Markl, Northwestern University, Chicago, USA.

TR $\leq$ T_2

In fast gradient echo acquisitions ($TR \leq T_2$), the transverse magnetization M_{xy} is not fully decayed prior to the next RF-pulse and contributes to the signal generation. The steady state magnetization is a mix of transversal and longitudinal magnetization com-

ponents, resulting in a complex signal weighting and contrast, depending not only on T_1, TR and α, but also on T_2 and local field homogeneity (see figure 2.20 left).

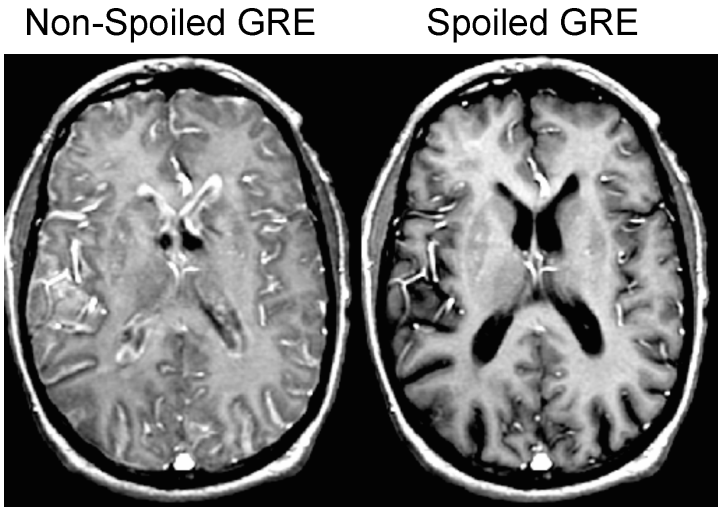

Figure 2.20: *Contrast behavior of GRE sequence with $TR \leq T_2$: non-spoiled (left) vs. spoiled (right).* Figure is courtesy of Prof. Michael Markl, Northwestern University, Chicago, USA.

However, many applications such as contrast-enhanced magnetic resonance angiography (CE-MRA, section 2.2.4.4) require not a mixed contrast but a pure T_1-weighting with short TE and TR. One approach is to use RF spoiled GRE, where the phase of the RF-pulses is systematically incremented and additional "spoiler" gradients are used after the readout process. This leads to a steady state that is approximately T_1-weighted according to the Ernst equation (2.11) [47] (see figure 2.20 right).

2.2.3.7 Contrast agents

An additional possibility for modulating the contrast of the MR images is the application of contrast agents. In most cases, MR contrast agents influence the tissue relaxation times T_1 and T_2, thereby changing the tissue signal intensity.
The effect of the contrast agents is based on the fact, that an electron produces a much stronger magnetic field than a proton. However, in most substances the electrons are paired ergo producing a weak net magnetic field [48]. Elements used in MR contrast agents, such as gadolinium (Gd) or manganese (Mn), have unpaired electrons and thus possess the ability to alter the relaxation times of adjacent protons. Paramagnetic contrast agents with Gd- or Mn-compounds have a similar effect on T_1 and T_2. The application of these contrast agents at low concentrations will result in T_1 shortening and thus, for T_1-weighted sequences in higher signal intensity of the tissue or vessel,

that takes up the contrast agents [48]. The signal intensity can only be increased up to a certain concentration of the contrast agent. Beyond this concentration, the signal intensity drops off again. As a parameter to describe the contrast mechanism, the tissue relaxivities $R_1 = 1/T_1$ and $R_2 = 1/T_2$ are used.
There are two types of contrast agents which are usually used in cardiovascular imaging: *extracellular* and *intravascular* contrast agents.
All currently used extracellular contrast agents contain gadolinium. After an intravenous bolus, extracellular contrast agent molecules migrate into the interstitial space, where they stay and do not pass through the cell membrane [49].
Intravascular or *blood pool* contrast agents are substances that do not or only to a small percentage leave the blood vessel, and thus provide advantages in vascular imaging.

2.2.3.8 MRI Hardware

The main hardware components of an MRI scanner are presented in this section and illustrated in figure 2.21.

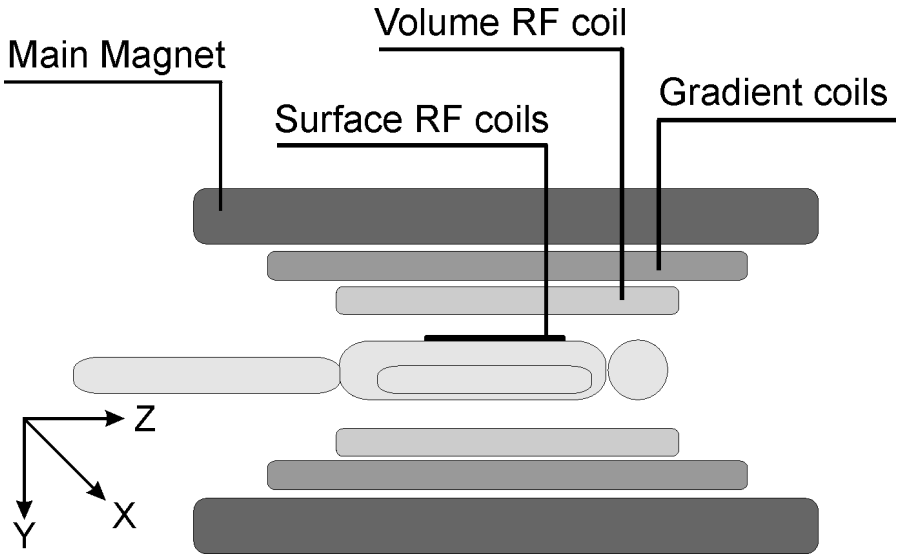

Figure 2.21: *Simplified schematic representation of the components of an MR scanner.* Image was adapted from [8].

Main components of an MR system are:

- The main magnetic coil generates a static, stable and homogeneous magnetic field $\vec{B}_0$ oriented along the bore of the magnet. In clinical routine, superconducting magnets with nominal field strengths of 1.5 or 3T are widely used. A reference coordinate system of three orthogonal axes (x, y, z) is used to define the magnetic

field direction, with $\vec{B}_0$ parallel to the z-axis; x-axis is the left-right and y-axis is anterior-posterior direction [42].

- Three gradient coils for all three spatial directions (x, y, and z) generate linear magnetic field gradients that are superimposed on the main static magnetic field $\vec{B}_0$ so that its strength increases (or decreases) along the direction of the applied gradient. This gradient magnetic field can be rapidly switched on and off. The strength of the gradient field reflects its slope and can reach up to 40 mT/m in a rise time of 200 μs [42].
- Radio frequency (RF) system comprises components for transmitting and receiving the RF signal. Major components are the RF coils, which are designed such that their emitted and received energy corresponds to the resonance frequency of hydrogen atoms. RF coils can be divided into two groups: *volume* and *surface* coils. Volume RF coils are optimized for the homogeneity of the emitted RF field. In clinical MR scanners a large volume coil is integrated into the system. Surface coils are placed as close as possible to the measured object, which will have an improved signal-to-noise ratio (SNR) but reduced RF homogeneity. Therefore, in measurements with surface coils, a separate volume coil is usually used for generating the RF-pulses, and inhomogeneity corrections have be to applied to the images (section 3.1.1).

  In cardiovascular application, a phased surface coil is commonly used. It is an array of overlapping coil elements, each connected to a separate receiver channel and decoupled from neighboring elements [50]. Each coil element covers only a part of the measured field of view and therefore receives signal from a constrained volume. The received noise increases with the square root of the number of coils, while signal intensity increases linearly [46].
- Hardware control/computer system (not illustrated in figure 2.21): It controls and monitors various functions such as switching between the gradients, generating the RF excitation pulse or reconstructing the images [44].

2.2.4 Cardiovascular MR imaging

As a non-invasive procedure in which patients are not exposed to any ionizing radiation, magnetic resonance imaging is widely used for diagnostics of the cardiovascular system. In addition to high spatial resolution and high soft tissue contrast, MRI provides the possibility to measure functional parameters such as blood flow or cardiac motion. However, motion such as heartbeat and respiration leads to artifacts in the images.
In the following, procedures for minimizing image artifacts are explained, as well as cardiovascular imaging techniques such as phase contrast MRI and contrast enhanced MR angiography are described.

2.2.4.1 ECG Gating

To synchronize the acquisition with the cardiac cycle and thus to minimize motion artifacts and capture the motion of the heart itself, the ECG signal is recorded during the MR examination. The detected R-wave is used as a trigger to time the pulse sequence. Thus, each measurement starts at the same time point in the cardiac cycle (prospective gating). To represent the dynamics of cardiac motion or blood flow throughout the cardiac cycle, the prospective gating is used in combination with time-resolved imaging (CINE).

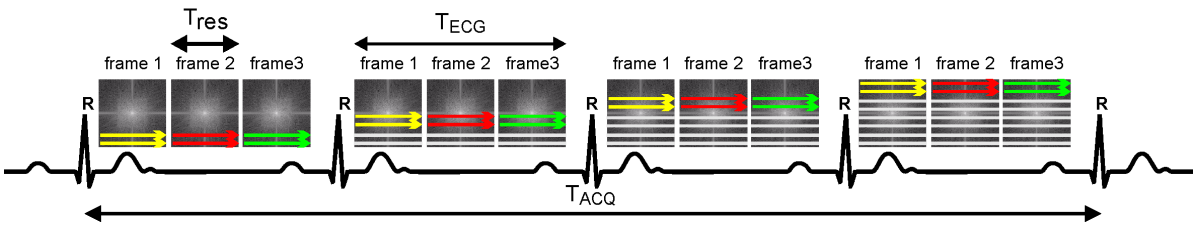

Figure 2.22: *Illustration of ECG gated CINE acquisition, here with* $N_{seg} = 2$, $N_P = 8$, $T_{ECG} \approx 3\,T_{res}$ *and* $T_{acq} = 4\,T_{ECG}$. Image adapted from [8].

Under assumption of cyclic reproducibility of a heartbeat, only few k-space lines (N_{seg}) are acquired per time frame and ECG cycle (T_{ECG}). The measurements are repeated over several cardiac cycles, until the complete k-space is acquired.
The temporal resolution (T_{res}) of the measurement is determined by $T_{res} = TR \cdot N_{seg}$ and the spatial resolution is determined by the number of phase encoding steps N_P. The total scan time (T_{acq}) of such acquisition is:

$$T_{acq} = \frac{N_p}{N_{seg}} \cdot T_{ECG}. \tag{2.12}$$

As evident from the equation above, the total acquisition time is not only influenced by the resolution and repetition time TR, but also by the heart rate of the subject (T_{ECG}). The faster the heart rate, the faster is the acquisition. The principle of ECG gated CINE measurement is illustrated in figure 2.22. An example of cardiac CINE acquisition is displayed in figure 2.23.

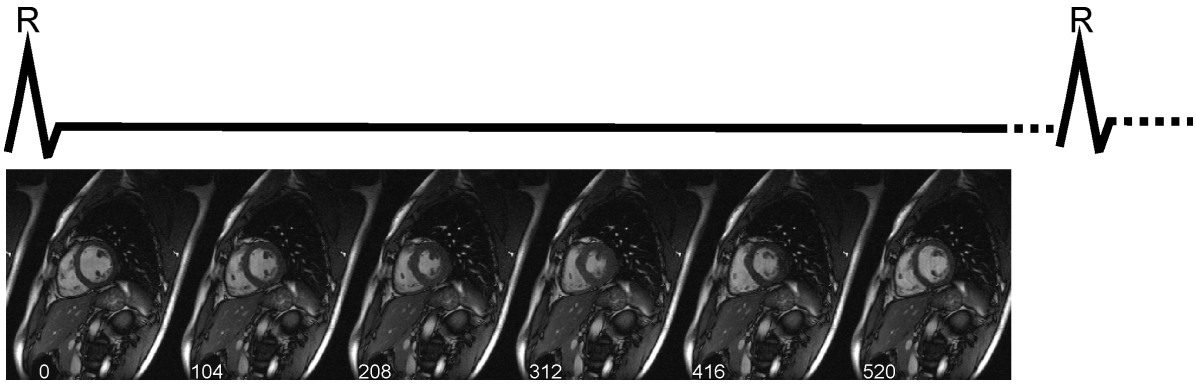

Figure 2.23: *An example of the heart acquired with CINE MRI.*

2.2.4.2 Respiratory motion compensation

The heart and adjacent blood vessels can move up to 2 cm due to breathing. This motion can cause ghosting and blurring artifacts in the images. To minimize these artifacts, the image acquisition can be performed while the subject is holding his breath. But the breath-holding approach is suitable for fast acquisitions ($\leq$ 20s) only.
The acquisition of the most time-resolved 3D data is not possible during a breathhold, therefore the measurement must be adapted to the respiration in order to minimize motion artifacts.
Several techniques are available for respiratory motion compensation, one of them is the *navigator gating* technique [51]:
A one dimensional MR signal of the diaphragm is recorded as a function of time. The diaphragm position corresponds to the breathing position, so the gating window can be placed in a certain respiratory phase. Typically, an end-expiratory gating window is used. Before the measurement, the expiratory position is determined and serves as a reference breathing position and is used to define an acceptance window. During data acquisition, one navigator is recorded for every ECG cycle. If the recorded breathing position falls into the predefined acceptance window, then the acquired data is accepted, otherwise it will be rejected and reacquired in a subsequent heart beat. The ratio between accepted and acquired acquisitions is referred to as acceptance rate and influences the total acquisition time. The acceptance rate can be increased by using a

larger acceptance window, resulting in reduced scan time but increasing artifact levels. The acquisition scheme is illustrated in figure 2.24.

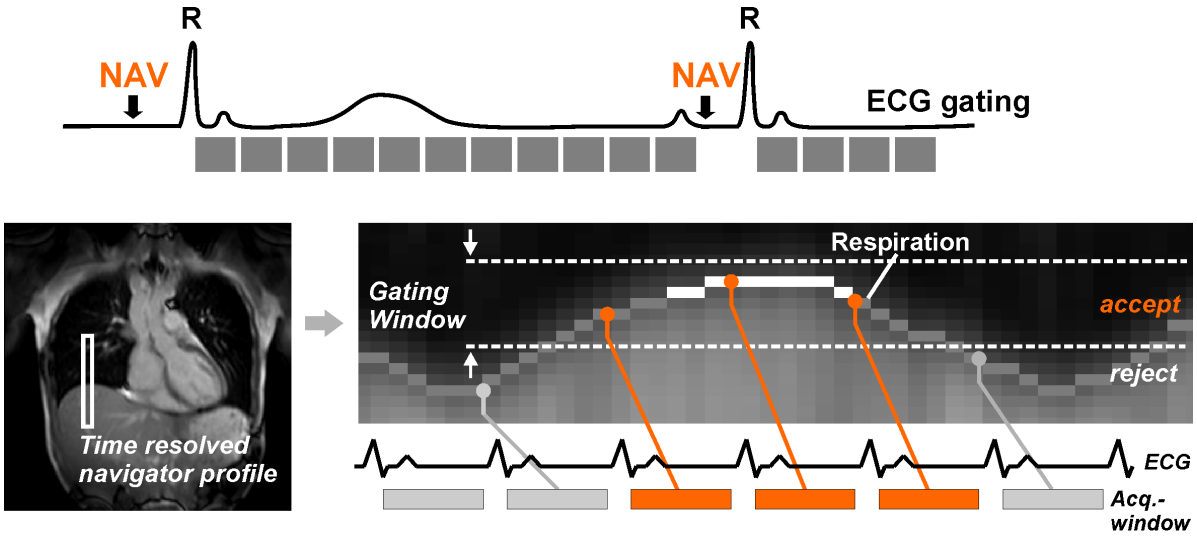

Figure 2.24: *Illustration of navigator gating, positioned over the lung-liver interface. Data outside the predefined gating window is rejected.* Figure is courtesy of Prof. Michael Markl, Northwestern University, Chicago, USA.

Furthermore, adaptive k-space reordering can be used to increase scan efficiency by sorting the data within the acceptance window into k-space according to their respiratory position [51]. This approach allows to increase the acceptance window without altering the image quality.
Other established respiration control techniques are respiratory self-gating and usage of an external respiratory sensor such as bellows. In self-gating technique the respiratory motion is sampled at certain time intervals by additional measurements of a central k-space point, center k-space profiles or low resolution images. This signal is then used to remove corrupted data either prospectively or retrospectively [52].
When using an external respiratory sensor, it will be placed around the subject's chest or abdomen. The respiratory displacement can then be determined and used to synchronize the acquisition.

2.2.4.3 Phase contrast MRI

Phase contrast (PC) MRI is a technique that is used for the direct measurement of blood flow or tissue motion velocities.
As described previously (section 2.2.3.1), the local spin magnetization is a vector quantity, meaning that the measured MR signal consists of a magnitude and a phase com-

ponent [53]. The PC-MRI technique is based on the fact that moving spins acquire an additional phase which is directly proportional to their velocity. The Larmor frequency of a moving spin $\vec{r}$ over time interval t is given by:

$$\omega_L(\vec{r},t) = \gamma(B_0 + B_{loc} + \vec{r}(t)\cdot\vec{G}(t)), \tag{2.13}$$

where B_0 is the strength of the main magnetic field, B_{loc} describes the local field inhomogeneities and $\vec{G}$ is the applied gradient [8]. The phase of the moving spins is:

$$\phi(\vec{r},t) = \int_0^{TE}\omega_L(\vec{r},t)dt = \underbrace{\gamma\, B_0\, TE}_{=0} + \underbrace{\gamma\, B_{loc}\, TE}_{\phi_0} + \gamma\int_0^{TE}\vec{G}\,(t)\,\vec{r}\,(t)\,dt. \tag{2.14}$$

Since the MR-signal is demodulated with the frequency of the main magnetic field B_0, phase contribution of $\gamma B_0\, TE$ is 0. Field inhomogeneities B_{loc} are static and result in an additional background phase ϕ_0. By applying Taylor expansion to equation (2.14) and limiting it to the first order, the phase of a spin becomes:

$$\phi(\vec{r},TE) \approx \phi_0 + \underbrace{\gamma\cdot\vec{r_0}\overbrace{\int_0^{TE}\vec{G}\,(t)\,dt}^{M_0}}_{\phi_0(\vec{r_0},TE)} + \underbrace{\gamma\cdot\vec{v}\overbrace{\int_0^{TE}\vec{G}(t)t\,dt}^{M_1}}_{\phi_1(\vec{v},TE)}, \tag{2.15}$$

where ϕ_0 is the background phase, $\phi_0\,(\vec{r_0},TE)$ is the phase shift of the static spins and $\phi_1\,(\vec{v},TE)$ is the phase shift of the moving spins. The integrals describing the contribution of the magnetic field gradients are referred to as gradient moments M_n. M_0 is the zeroth moment representing the area of the gradient and M_1 is the first gradient moment representing the time weighted area of the gradient. A gradient produces a spatially dependent phase shift (section 2.2.3.4), which means that by applying an oppositely oriented gradient of equal strength and duration (*bipolar gradient*), the total phase shift becomes zero in stationary tissue [7, 53], as illustrated in figure 2.25. As result the phase shift of the moving spins $\phi_1\,(\vec{v},TE)$ is proportional to the blood flow velocity or tissue motion $\vec{v}$ itself but also to the strength and timing of the applied gradient $\vec{G}$.

Velocity encoding strategies

The background phase ϕ_0, caused by field inhomogeneities, cannot be eliminated using bipolar gradients. To remove such a background phase, an additional scan is performed with different M_1. This can be done in two ways:

1. In the first approach, a velocity compensated scan is performed, thereby both static and moving spins are rephased (see figure 2.25, left), $M_0 = M_1 = 0$. Additionally, a velocity sensitive scan is measured with bipolar gradient, resulting in $M_0 = 0$ and $M_1 \neq 0$ [54].
2. In the second approach, encoding moments are equally distributed between scans, e.g. two measurements with different first moments $M_1^{(1)}$ and $M_1^{(2)}$ (with inverted gradient polarities) are performed [53, 54].

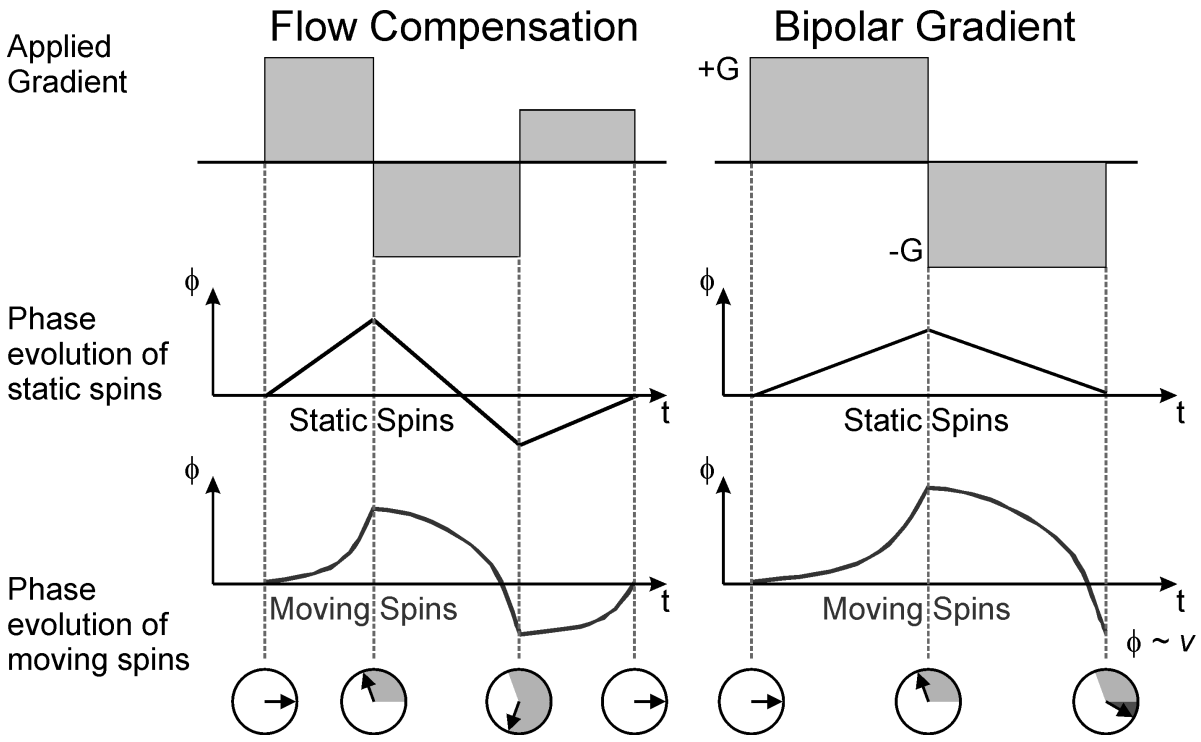

Figure 2.25: *Schematic illustration of velocity encoding in PC-MRI. Left: Gradient switching for velocity compensated scan, where both static and moving spins are fully refocused. Right: Application of a bipolar gradient leads to a phase shift of moving spins proportional to their velocity, whereas static spins are fully refocused.* Figure was adapted from [55].

By subtracting phase images from such two measurements, phase shifts not related to flow are filtered out and the remaining phase difference $\Delta\phi$ is directly proportional to the respective velocities v [53]:

$$v = \frac{\Delta\phi}{\gamma \Delta M_1}. \tag{2.16}$$

Phase shifts can be measured in the range of $\pm\,\pi$. Adjusting gradient duration and/or strength controls the so called velocity encoding sensitivity (v_{enc}), which is defined as

the maximum velocity corresponding to the phase shift of π:

$$v_{enc} = \frac{\pi}{\gamma \Delta M_1}. \tag{2.17}$$

In PC-MRI ECG gating, respiratory control and velocity encoding are combined for data acquisition. Schematic representation can be found in figure 2.26.

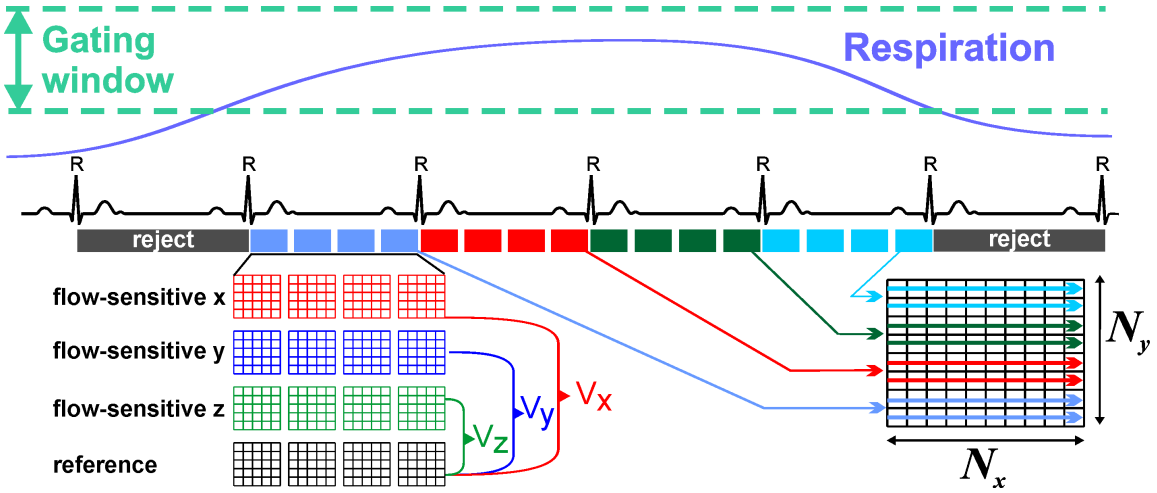

Figure 2.26: *Schematic illustration of ECG gated CINE PC-MRI acquisition with adaptive respiratory gating. The data within the acceptance window are sorted into the k-space according to their respiratory position. Data outside of the gating window are rejected.* Figure was adapted from [8].

2.2.4.4 Contrast enhanced MR angiography

For the presentation of vascular anatomy and identification of location and extent of pathological changes such as stenosis or aneurysm, contrast-enhanced MR angiography (*CE-MRA*) has been widely established in clinical routine. After intravenous contrast agent injection, the arterial bolus passage of the contrast agent is synchronized with a fast T_1-weighted 3D gradient echo sequence. Due to relaxation properties of the contrast agent (T_1 shortening) and appropriate adjustment of sequence parameters, the signal of the arterial structure is enhanced (figure 2.27), while surrounding tissue and background signals can be suppressed.

Figure 2.27: *CE-MR angiography in a patient with large aneurysm in the proximal descending aorta.*

2.3 Flow-sensitive MR data

2.3.1 4D Flow MRI

In the work presented here, 4D blood flow data are used. These data are acquired with time-resolved 3D PC-MRI with 3 directional velocity encoding (section 2.2.4.3). The data acquisition is synchronized with ECG (section 2.2.4.1) as well as with the subject's respiration (section 2.2.4.2).
To encode blood flow velocities in all three spatial directions, four data sets are acquired using interleaved velocity encoding as described in section 2.2.4.3. Each of these data sets consists of phase and magnitude images [56].
Magnitude images contain information about signal amplitude and represent the anatomy of the patient [57]. Four acquired magnitude data sets are averaged and thus provide a single magnitude data set.
The reference phase images are subtracted from each of three velocity encoded phase images, in order to yield images from flowing blood only, since the signal of the static tissue should be nulled by subtraction. The subtraction process results in three velocity data sets, each representing velocity in one spatial direction (see figure 2.28), where each voxel in the phase images contains the mean velocity of the spins in that voxel.

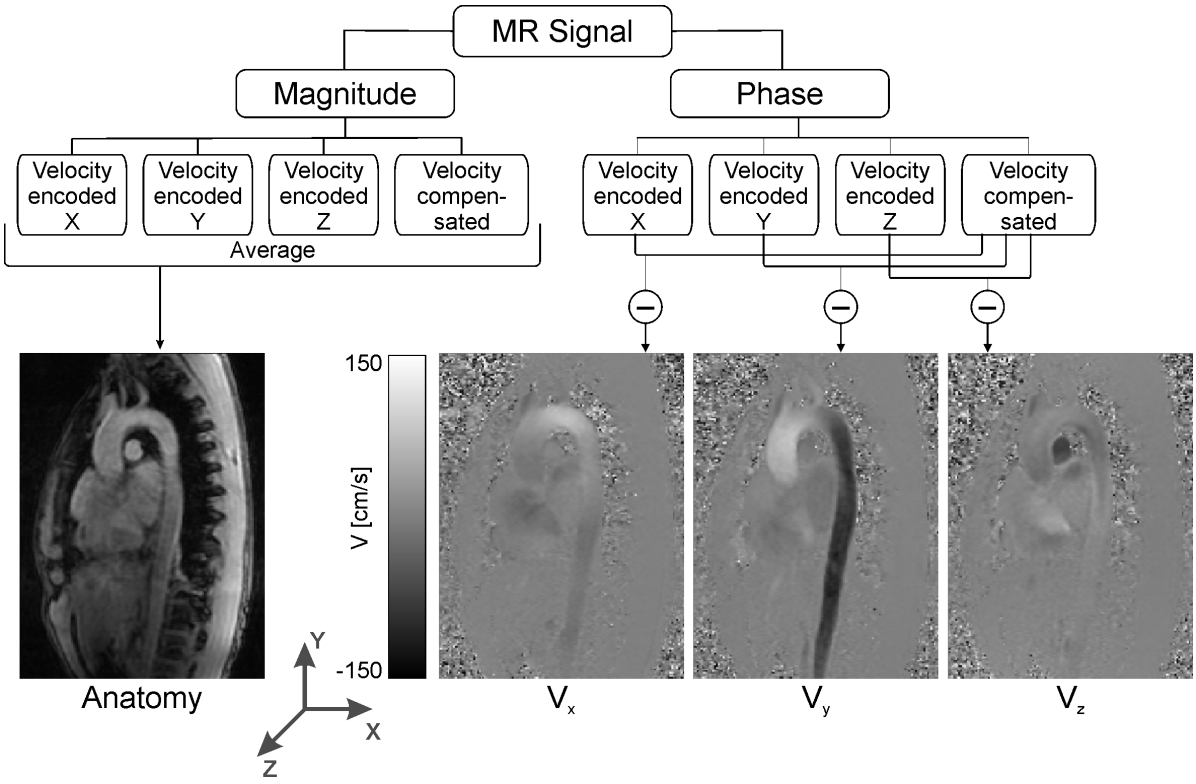

Figure 2.28: *Schematic diagram showing phase-contrast velocity mapping.*

2.3.2 Artifacts and sources of error

Artifacts in MR imaging can impact image quality of magnitude images. Additionally, several sources of errors can affect the velocity encoded images.

2.3.2.1 Partial volume effects

The partial volume effect occurs if the imaging voxel contains more than one sort of tissue. Thus the signal intensities of different tissues in a voxel are not resolved separately, but are represented as the weighted average of both signal intensities. The weighting factor is the relative percentage of the tissue types within the voxel. Partial volume effects may decrease the visibility of small or low-contrast structures, reduce the accuracy or simulate abnormalities [44, 58].
Partial volume effects make segmentation processes more difficult since they result in a blurring of intensity across boundaries, where multiple tissues contribute to a single voxel [59]. So partial volume effects can cause regions of separated or different tissue types to appear connected.

2.3.2.2 Intensity non-uniformity

B_1-inhomogeneity of the surface coil, also known as intensity non-uniformity, bias field or shading, is an artifact, which arises mainly from a very steep sensitivity drop of the surface coils in the direction of the increasing tissue depth [60] and appears as smooth non-anatomical intensity variations across the images [61]. In cardiovascular imaging, the aorta is located in the middle of the body, so it has a greater distance from the coils as the surrounding tissue or organs (figure 2.29) and is therefore very sensitive to intensity non-uniformity. Retrospective non-uniformity image correction can be applied as described in section 3.1.1.

2.3.2.3 Image Noise

Noise is an ever present phenomenon in MR images, generated by receiver coils and electronics, as well as by physiological noise, i.e. patient's body due to moving charges. The relationship between the intensity of signal and noise is called signal-to-noise-ratio (SNR_{mag}) and is an important parameter for evaluating the image quality:

$$SNR_{mag} \propto voxel\,size \cdot \sqrt{T_{acq}}, \tag{2.18}$$

where T_{acq} is the total acquisition time and voxel size represents the spatial resolution. The measurement noise affects the acquisition of the MR signal in the real and imaginary

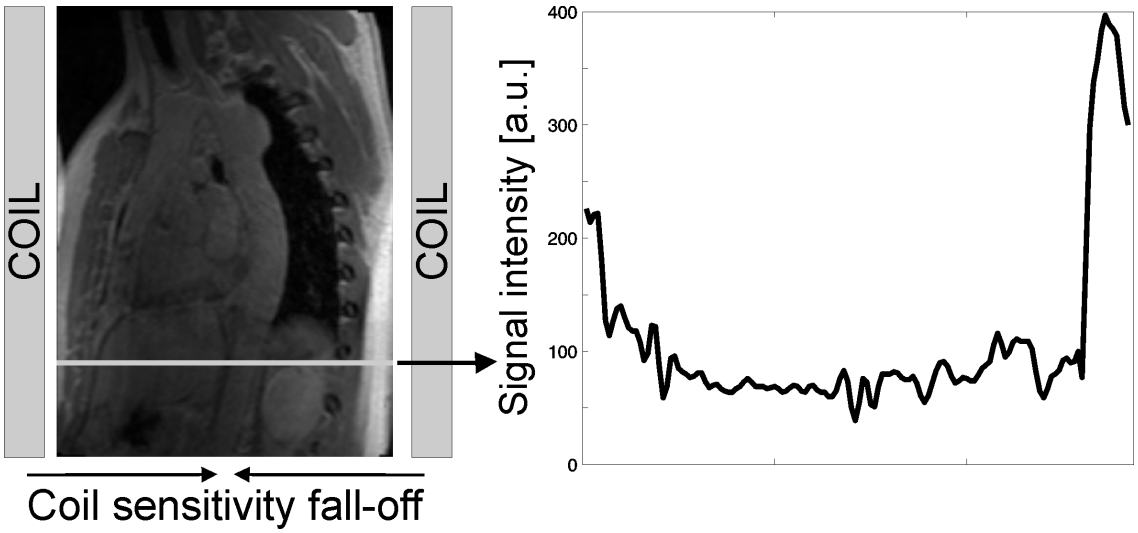

Figure 2.29: *Left: Schematic illustration of coil positioning for an aortic MRI acquisition (at the spine and at the top of the abdomen). Right: signal intensity profile for an image row (white line in the left image).*

domain. Consequently, the noise in phase-contrast velocity images is inversely related to SNR in the corresponding magnitude images [53, 55]. The noise standard deviation in the velocity images is given by [37, 53]:

$$\sigma(\phi) = \frac{\sqrt{2}}{\pi} \frac{v_{enc}}{SNR_{mag}}, \tag{2.19}$$

where SNR_{mag} is the signal-to-noise-ratio measured in the magnitude images and v_{enc} is the user selected velocity sensitivity. There is always a trade-off in adjusting the v_{enc}: on the one hand, v_{enc} should be adjusted as small as possible to have low noise, on the other hand v_{enc} should be as large as possible to avoid phase wraps (see section 2.3.2.7).

2.3.2.4 Eddy currents

Due to the rapid switching of magnetic field gradients during MR imaging, currents are induced in conducting surfaces, in particular in the gradient coils. These so-called eddy currents interfere with the static field B_0 and distort the desired magnetic gradients, resulting in phase offset errors that can be recognized by nonzero velocity of the stationary tissue [8, 62] (figure 2.30). Velocity offset errors lead to errors in blood flow quantification. Therefore, it is substantial to correct the phase contrast data for eddy currents. Correction methods are described in section 3.1.3.

2.3.2.5 Concomitant gradient terms

As the patient is not a magnetic monopole and current or electric field present in the patient are negligible, the magnetic field can be described by following Maxwell's equations:

$$\nabla \bullet \left(\vec{B_0} + \vec{B_G}\right) = \vec{0}, \tag{2.20}$$

$$\nabla \times \left(\vec{B_0} + \vec{B_G}\right) = \vec{0}, \tag{2.21}$$

where $\vec{B_0}$ is the main magnetic field and $\vec{B_G}$ is the gradient field. As a consequence of Maxwell's equations, by switching on a magnetic field gradient additional non-linear spatial dependent magnetic fields are generated [63]. These additional magnetic fields are referred to as concomitant gradient terms or Maxwell terms $\vec{B_C}$:

$$\vec{B_G} = \vec{G} \cdot \vec{r} + \vec{B_C}.$$

Concomitant gradient terms result in phase errors (figure 2.30). Since the amplitude and the duration of the gradients are known, the signal phase can be corrected in the image reconstruction process.

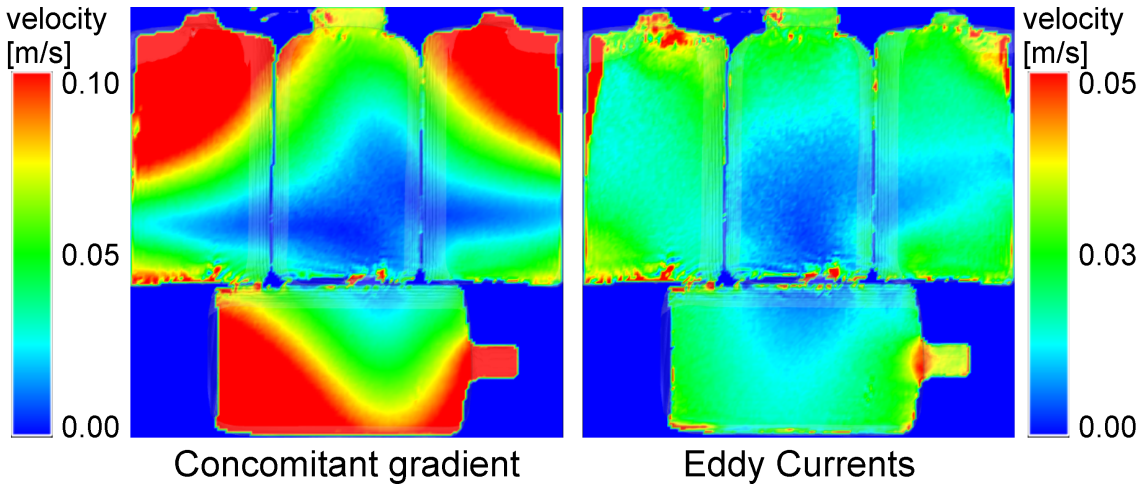

Figure 2.30: *Phase errors due to concomitant fields (left) and eddy currents (after correction for concomitant fields) in static phantoms. For a static phantom, the phase should be uniformly zero. However, spatially distributed different phases can be observed.* Images are courtesy of Ramona Lorenz, University Medical Center, Freiburg.

2.3.2.6 Gradient field non-linearities

Due to imperfections of the magnetic field gradient coils, it is complicated to generate a perfect linear increasing field along each gradient axis [55]. These imperfections introduce errors in velocity measurements by affecting the first moments M_1 used to encode flow or motion [64]. Using a vendor dependent gradient model, the errors can be corrected.

All phase offset errors (eddy currents, concomitant fields, gradient non-linearities) are strongly dependent on the position in the scanner. There is a non-linear increase in offsets with increasing distance from iso-center (s. figure 2.30). Due to large volumetric coverage in 3D PC-MRI, it is very important to correct for these phase offsets in order to get reliable results for derived parameters such as flow or pressure gradients.

2.3.2.7 Phase aliasing

A further problem is the phase aliasing artifact which may occur in the velocity encoded images. In PC-MRI, the velocity is measured as phase shift ϕ, which is in the range of $\pm$ 180° ($\pm$ π radians) [56, 57]. The velocity encoding sensitivity (v_{enc}) is thereby the maximum velocity that corresponds to the maximum phase shift of 180° (π). Any velocity larger as v_{enc} will be folded back into the principal value range, producing a wrapped phase ψ, which differs from ϕ by an unknown integer multiple of 2π [65]. Thus, the velocity values in the voxels with spins at a higher velocity than v_{enc} will be interpreted incorrectly (see figure 2.31) and need to be corrected [66]. The phase unwrapping process is described in more detail in section 3.1.4.

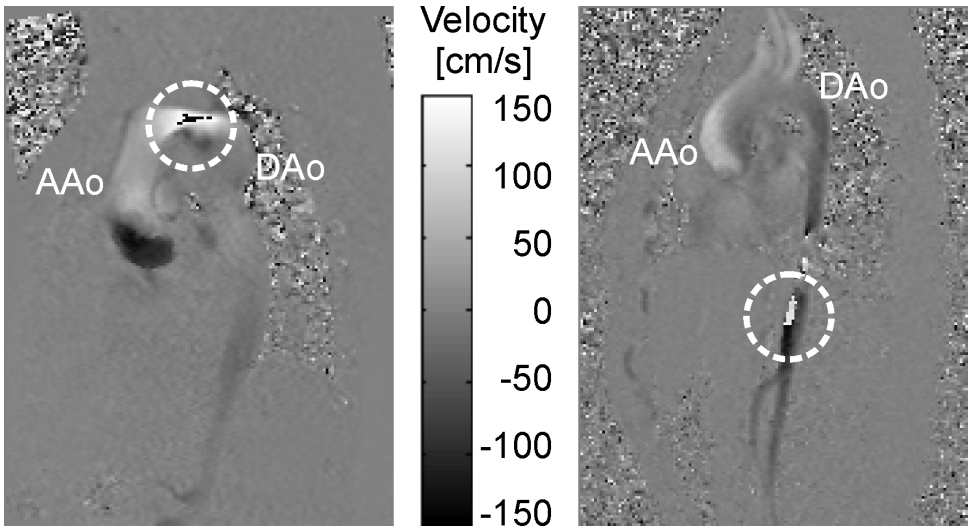

Figure 2.31: *Examples of phase wraps in left-right direction (left) and in up-down direction (right) in human aorta.*

2.4 Vasculature segmentation techniques

Segmentation describes the division of an image into regions or objects, which are homogeneous with respect to some properties. In this work, we are interested in segmentation of the aorta. There exist many approaches for vessel segmentation with optimization based on different modalities, e.g. CT, MRI, data acquisitions schemes and even vascular regions (brain, aorta, etc.). The following articles provide a good overview and review of various vessel segmentation techniques: Suri et al.[67], Kirbas and Quek [68], Lesage et al.[69].
It is beyond the scope of this work to describe all the approaches, therefore only the segmentation techniques used for aortic 3D phase contrast MR data are described. In contrast to 2D CINE PC-MR imaging, which is established in clinical routine, time-resolved 3D PC-MRI acquisitions are rather novel. To date, not many segmentation techniques are established for this type data. The specific segmentation techniques of thresholding (section 2.4.1), region growing (section 2.4.2), active surfaces (section 2.4.3) and centerline-based approach (section 2.4.4) are summarized below. Since this work is based on segmentation using pixel classification, this method is described in more detail in chapter 2.5.

2.4.1 Thresholding

Thresholding plays a central role in segmentation, because of its simplicity in implementation, computational speed and easily understandable properties [70, 71]. During the thresholding process, an image is divided into a group with values equal or larger than a certain predefined value (e.g., the threshold) and into a group having values lower than the threshold. When applying a threshold value T to the image $I(x, y)$, the segmented image $J(x, y)$ is given by

$$J(x,y) = \begin{cases} 1 & \text{if } I(x,y) \geq T \\ 0 & \text{if } I(x,y) < T \end{cases}$$

in which any point (x,y) with value 1 is called an object point and points with a value 0 are background points. In *global* thresholding a single threshold value T is selected for the entire image $I(x, y)$. Selection of T can be based on the intensity histogram or other properties of the entire image. In *variable* (regional or local) thresholding the value of T changes over an image. The value of T can be determined by dividing the image into subimages and computing T for each subimage, or by analyzing image intensities in a neighborhood of a pixel [70].

The selection of the threshold value can be performed *manually* or *automatically*. In the manual process the value is determined by the user. For automatic threshold selection, *Otsu's method* [72] is an efficient procedure to determine T entirely based on computations performed on the histogram of an image [70].

Otsu's method

Let $p(0), p(1), \ldots, p(g), \ldots, p(G-1)$ with $0 \leq p(g) \leq 1$ denote the normalized histogram of the image I, where $p(g)$ is the probability of the occurrence of gray level g and G is the total number of gray values. C_0 and C_1 are two classes which are to be separated by the threshold value T. Using this threshold the probability P_i that a pixel is assigned to class C_i is given by:

$$P_0 = \sum_{g=0}^{T} p\left(g\right) \quad \text{and} \quad P_1 = \sum_{g=T+1}^{G-1} p\left(g\right) = 1 - P_0. \tag{2.22}$$

Furthermore, $\bar{m}_0$ is the mean intensity value of the pixels from class C_0 and $\bar{m}_1$ is the mean intensity value of C_1 pixels, with the mean intensity value $\bar{m}$ of the entire image being:

$$\bar{m} = \bar{m}_0 P_0 + \bar{m}_1 P_1. \tag{2.23}$$

The corresponding variances are:

$$\sigma_0^2 = \sum_{g=0}^{T} \left(g - \bar{m}_0\right)^2 p\left(g\right) \quad \text{and} \quad \sigma_1^2 = \sum_{g=T+1}^{G-1} \left(g - \bar{m}_1\right)^2 p\left(g\right). \tag{2.24}$$

The threshold T is determined by maximizing the inter-class variance σ_B^2 and minimizing the intra-class variance σ_W^2, with

$$\sigma_B^2 = P_0 \left(\bar{m}_0 - \bar{m}\right)^2 + P_1 \left(\bar{m}_1 - \bar{m}\right)^2, \tag{2.25}$$

and

$$\sigma_W^2 = P_0 \sigma_0^2 + P_1 \sigma_1^2. \tag{2.26}$$

The optimal threshold value T is the one for which the ratio $\frac{\sigma_B^2}{\sigma_W^2}$ is maximized.

2.4.2 Region-based segmentation

Region-based segmentation techniques analyze pixels in an image I and form N regions, R_i, by grouping adjacent pixels with homogeneity properties based on a predefined

similarity criterion [71]. The regions must satisfy the following properties:

$$\begin{aligned} I &= \bigcup_{i=1}^{N} R_i, \\ R_i \cap R_j &= \varnothing \quad \forall i, j = 1, \ldots, N;\ i \neq j, \\ L(R_i) &= TRUE \quad for\ i, j = 1, \ldots, N, \\ L(R_i \cap R_j) &= FALSE \quad \forall i, j = 1, \ldots, N;\ i \neq j, \end{aligned}$$

where $L(.)$ is a logical predicate (boolean-valued function), containing a set of rules, that must be satisfied by all pixels within the given region [71].
Region growing is a basic region-based segmentation technique, consisting essentially of two steps. In the first step, the so called *seed point* (a single pixel or a set of pixels which belongs to the target region) is selected. The seed can be chosen manually or automatically by a seed finding algorithm [71]. In the next step, the neighborhood of the seed is analyzed and pixels with similar values to the seed are appended to the region including the seed. Thus, the region is growing and changing shape. The last step is repeated until further merging operations cannot be performed. A similarity criterion could be chosen based on pixel intensity or texture. Region growing schemes are simple and computationally efficient algorithms. They explore datasets only sparsely, which is an important advantage for large datasets [69].

2.4.3 Active contour model

The active contour (in 2D) or surface (in 3D) model, first introduced by Kass et al. [73], is an iterative segmentation method and is widely used for vessel segmentation, especially in 2D data sets [74–76].
In the active surface model approach, a parametric surface is deformed until the surface approximates the boundaries of interest in the provided data set [6]. The 3D active surface is typically described by a contour $X : [0,1] \times [0,1] \rightarrow \mathbb{R}^3$ placed on a dataset $I : \mathbb{R}^3 \rightarrow \mathbb{R}$. The active surface model focuses on minimizing the total energy E_{total}:

$$E_{total} = E_{int}(X) + E_{ext}(X),$$

where E_{int} is the *internal energy* and E_{ext} is the *external energy*. The internal energy depends on the shape of the contour and determines the stretching and bending behavior

of the contour [74]:

$$E_{int} = \frac{1}{2}\int_s \left(\alpha \left\| \frac{\partial X}{\partial s} \right\|^2 + \beta \left\| \frac{\partial^2 X}{\partial s^2} \right\|^2 \right) \, ds,$$

where α and β are the weighting coefficients for the magnitude of the first and second order spatial derivatives of the contour, respectively, and control the elasticity and rigidity of the contour, and $s \in [0,1] \times [0,1]$.
The external energy is associated with image forces attracting the surface to the desired boundaries [74]. Image forces are derived from the feature image, I_F:

$$E_{ext} = \int_s I_F \, ds,$$

and using a classical choice of $I_F = \|\nabla I\|^2$, the surface will be attracted towards contours with large image gradients. In 3D vascular segmentation, local phase coherence (i.e. the average angle between a velocity vector and its neighbors) [77], eigenvalue coherence (ratio of the ordered eigenvalues) [78] can be used as the feature image, I_F.

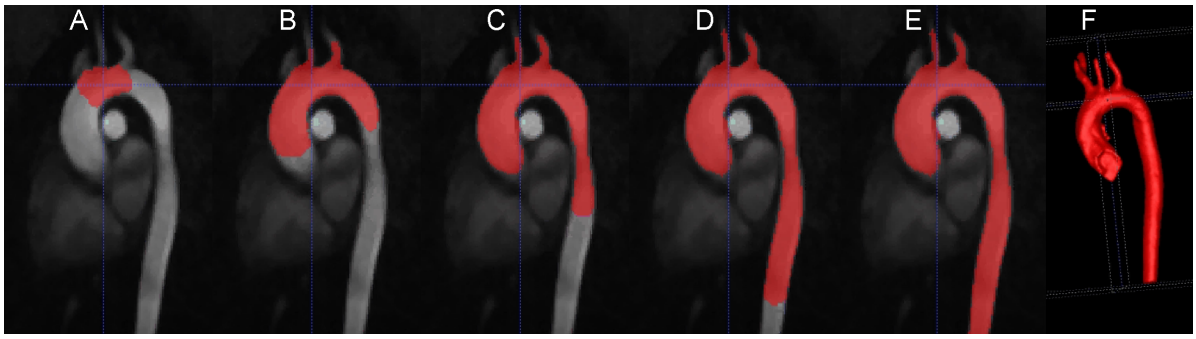

Figure 2.32: *Example for vessel segmentation using active contours model from ITK-SNAP. Images A-E represent some of the iteration steps, resulting in the 3D segmentation of the complete thoracic aorta (F). Coefficients α and β were adjusted empirically.* Image adapted from [8].

2.4.4 Centerline-based techniques

In contrast to region-growing and active contour approaches focusing on directly detecting the vessel contours, centerline-based techniques are based on extracting the vessel centerline [69]. Centerlines can be extracted from approximate surface segmentation by skeletonization (extraction of the thinnest representation of a shape that is equidistant to its boundaries). Evidently, centerline does not provide true vessel lumen segmentation, but the extracted centerline can be used to constrain the subsequent surface segmentation. One approach is to segment the vessel wall iteratively in cross-sectional

planes, using for example active contours, and then from these 2D contours, a 3D surface can be optimized using geometric models [69, 79, 80]. Another possibility is to obtain or refine the vessel surface directly in 3D using active surfaces [81].

Figure 2.33: *Example of a centerline model for subsequent vessel segmentation.* Image was taken from [81].

2.5 Data clustering

In the processing of time-resolved PC-MRI data sets, segmentation is an important processing step allowing better visualization and improved derivation of hemodynamic parameters. In clustering, the data is divided into groups and thus clustering can be used for image segmentation. Clustering offers the advantage for the PC-MRI data, that the subdivision is not limited to vessel and background, but static tissue can also be determined. In addition, clustering can be advantageous with respect to large data sets, as is the case with time-resolved 3D PC-MRI.
The theoretical background of the data clustering is explained in the following. The applied clustering methods are described in more details in chapter 5.

2.5.1 Basic principles

In cluster analysis, a collection of patterns is organized into clusters (groups) based on similarity, such that members of a cluster are more similar to each other than to members of other clusters [82, 83]. Clustering is thereby an *unsupervised classification*. In contrast to supervised classification, where a collection of labeled (pre-classified) patterns is provided and used to learn the descriptions of groups, the task of clustering is to group the collection of unlabeled patterns into meaningful clusters. In a sense, clustering is a labeling process as well, but these labels are data driven, i.e. they are obtained solely from the data [83].
The main components of pattern clustering are [83, 84]:

1. *Pattern representation* refers to the number of classes, the number of available patterns and the number, type and scale of features. Optionally, *feature extraction* and/or *selection* can be included. Feature selection is thereby a process of identifying the most effective subset of the original features and feature extraction uses the transformations of the input features to generate new enhanced features.
2. The next step is to define a *pattern proximity measure* that is appropriate to the data domain. Usually, the proximity is measured by a distance function defined on pairs of patterns. The Euclidean distance can be employed to measure the dissimilarity between two patterns [83, 85].
3. The *clustering* or *grouping* step can be performed in many ways. For this work, relevant output clusterings are either *hard*, i.e. an all-or-nothing assignment of patterns to only one class, or *fuzzy*, where each pattern possesses a certain degree of membership in each of the output clusters [86]. By assigning each pattern to the cluster with the largest membership value, a fuzzy clustering can be converted to a hard clustering [83].

Clustering is useful for data reduction. Since the amount of data is often very large and therefore requires very demanding processing, the cluster analysis can be used to group the data into a number of clusters and to process each cluster subsequently as a single entity [87].

2.5.2 Definitions and terminology

In clustering, N objects, or observations are grouped in c clusters, where $2 \leq c < N$. Each observation N consists of a set of p numeric attributes or features [85]. The data set describes a data collection with $N \times p$ values.
Let $X = \{x_1, x_2, ..., x_N\}$ denote a data set to be clustered. This set X consists of N vectors, x, where each x comprises p features. Each

$$x_k = (x_{k1}, x_{k2}, ..., x_{kp}) \in \mathbb{R}^p$$

is called a feature or pattern vector [82].
In *hard* (or *crisp*) clustering, the goal is to divide X into the disjoint non-empty partitions $S_1, ..., S_c$ defined by [85]:

$$X = S_1 \cup ... \cup S_c,$$

where

$$S_i \cap S_j = \emptyset \quad i, j \in \{1, ..., c\}, i \neq j,$$

and

$$S_i \neq \emptyset \quad i \in \{1, ..., c\}.$$

In *soft* (or *fuzzy*) clustering, the goal is to find the *partition matrix* U with $c \times N$ real elements. The matrix U defines membership degree for each feature vector:

$$U \in \mathbb{R}^{c \times N} = [u_{ik}] \quad i \in \{1, ..., c\}, k \in \{1, ..., N\},$$

where u_{ik} is the *degree of membership* of x_k in cluster i,

$$u_{ik} \in [0, 1] \quad \forall i, k.$$

Clusters should contain objects with feature vectors relatively similar to each other. To measure the similarity, the correlation of two vectors can be used as a similarity index. Conversely, the Euclidean distance between two vectors can be employed as a dissimilarity index. Greater similarity of two objects is reflected in a larger similarity index and a correspondingly smaller dissimilarity index.

In most partitional clustering methods (section 2.5.3) the following concept is employed: for a given cluster i, there exists an ideal point p_i (the *prototype* of the cluster) with $p_i \in \mathbb{R}^p$, which best represents members of cluster i [85]. Thus, the aim of such clustering algorithms is to find a set of c prototypes that best represent the clustering structure in X:

$$P = \{p_1, p_2, \ldots, p_c\} \quad \text{, where } p_i \in \mathbb{R}^p \quad \forall i \in \{1, \ldots, c\}\,.$$

The clustering method used in the presented work employs a distance metric to measure similarities between data points and prototypes. The most common distance metric is the Euclidean:

$$\|x_k - p_i\| = \sqrt{(x_{k1} - p_{i1})^2 + \ldots + (x_{kp} - p_{ip})^2}.$$

Furthermore, clustering approaches often employ an objective function in order to evaluate the preliminary clustering of the data set. The distance metric is usually exploited in such objective functions.
Schematic illustration of fuzzy clustering including all important variables is presented in figure 2.34.

2.5.3 Clustering techniques

Several clustering approaches have been described previously in the literature. These approaches are divided into two major groups: *hierarchical* and *partitional* [83].
Hierarchical methods produce a tree-structured partitioning of the data. This tree structure is called a dendogram, representing the nested grouping of patterns and similarity levels at which grouping changes [83, 85]. The root of the tree is a cluster covering all points, and tree leaves are clusters containing only one point. For large data sets, such construction of a dendogram is computationally intensive, hence, hierarchical clustering is not suitable for phase contrast data. More details on hierarchical clustering can be found in literature [83, 87].
In contrast to hierarchical clustering, *partitional* methods produce only one partition of the data instead of a clustering structure. Therefore partitional methods have advantages when processing large data sets. Most partitional algorithms assume *a priori* a number of clusters and produce clusters by optimizing an objective function defined either locally (on a subset of the patterns) or globally (over all the patterns). An example of partitional clustering is the *c-means* algorithm which is described in section 2.5.4.1.

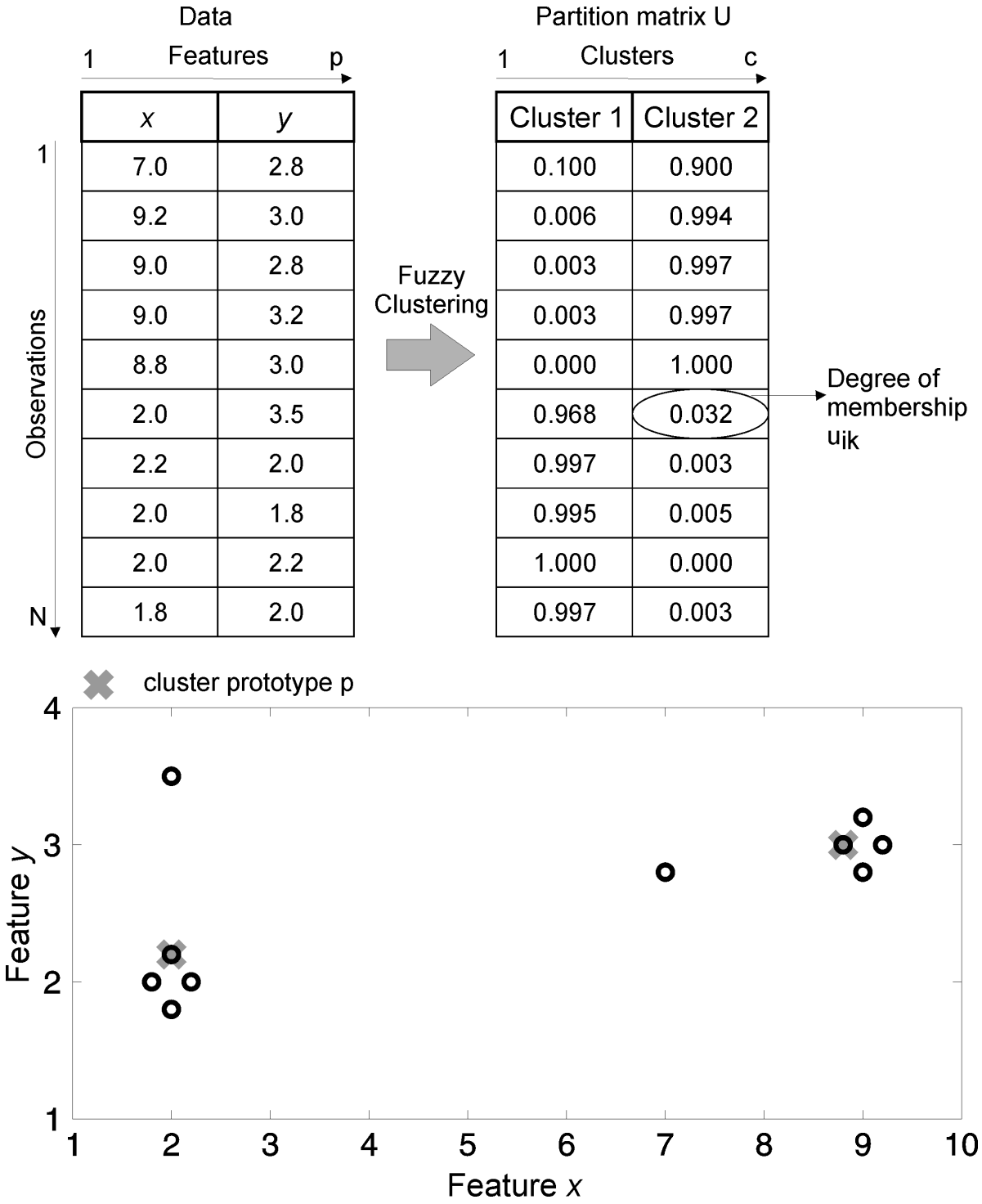

Figure 2.34: *An illustration for fuzzy clustering. A data set (black circles) consisting of 10 points is divided into 2 clusters with prototypes presented by gray crosses.* Adapted from [85].

2.5.4 Fuzzy clustering

In hard clustering approaches, partitions are generated with the constraint that each pattern belongs to one and only one cluster [83] within the specified partition. In fuzzy clustering each pattern is associated with every cluster using a membership function [88].

2.5.4.1 Fuzzy c-means clustering

The c-means algorithm (FCM) is the predominant fuzzy clustering algorithm. The FCM algorithm is an iterative optimization that minimizes the following cost function:

$$J_{FCM} = \sum_{i=1}^{c} \sum_{k=1}^{N} u_{ik}^{m} \|x_k - p_i\|^2, \tag{2.27}$$

where u_{ik} is constrained to be positive and represents the membership degree of the feature vector x_k in the i^{th} cluster, p_i is the prototype or centroid of the i^{th} cluster, $\|\cdot\|$ is a norm metric, and m is a so called fuzzification parameter, which controls the fuzziness of the resulting partition. Larger values of m result in fuzzier solutions.
The cost function J is a subject to the following constraint:

$$\sum_{i=1}^{c} u_{ik} \;=\; 1 \quad \forall k \in \{1, \ldots, N\}\,. \tag{2.28}$$

The cost function is minimized when feature data x close to the centroid of a cluster p_i are assigned high membership values u_{ik}, and low membership values are assigned to pixels with data far from the centroid [89]. The membership function represents the probability that data x belongs to a certain cluster. In FCM, this probability depends on the distance between the feature vector x_k and each individual cluster prototype p_i in the feature domain [89]. The objective function J is optimized alternately regarding the membership degrees u_{ik} and cluster centers p_i by the following conditions:

$$p_i = \frac{\sum\limits_{k=1}^{N} u_{ik}^{m}\, x_k}{\sum\limits_{k=1}^{N} u_{ik}^{m}}, \tag{2.29}$$

$$u_{ik} = \frac{1}{\sum\limits_{j=1}^{c} \left(\frac{\|x_k - p_i\|}{\|x_k - p_j\|} \right)^{2/(m-1)}}. \tag{2.30}$$

The FCM converges to a local minimum solution for p_i. A proof of the convergence to a local minimum can be found in Bezdek [82].

The algorithm

The FCM algorithm can be implemented as follows:

1. Initialization:
   - Choose the number of cluster c, $2 \leq c < N$. Each cluster is described by a prototype p_i.
   - Fix the fuzzification parameter m, $1 \leq m < \infty$.
   - Choose a termination accuracy ϵ and a maximum number of iterations.
   - Initialize cluster prototypes and the membership function U accordingly.
2. Calculate fuzzy cluster centers P using equation (2.29) for each cluster c.
3. Update the membership function U using equation (2.30).
4. Compare the change in the membership values, and if the change is smaller than ϵ, stop the procedure. Otherwise, return to step 2.

2.5.5 Medical image segmentation using clustering

Clustering provides a good framework for medical image analysis where segmentation is considered the main task [85]. In the clustering process, similar (tissue) pixels are grouped. It is assumed that mathematically similar pixels will belong to the same physical tissue types [90]. Segmenting images using clustering can be divided into three steps:

1. *Feature extraction* determines how the image data is presented to the clustering algorithm.
2. Selection and set up of the clustering algorithm.
3. *Post-processing* of the output from clustering.

Steps 1 and 3 are discussed in the following sections. In regards to step 2, there is a variety of clustering algorithms with descriptions can be found elsewhere (e.g. Jain et al. [83]). In this work we focused on fuzzy clustering, which was described in section 2.5.4.

2.5.5.1 Feature extraction

Feature extraction can be accomplished in three ways [85] using:

1. *Voxels intensities* only. The simplest way to extract a feature set is to use the available image measurements. This feature set consists of a given voxel's intensity in each image, acquired for example with different acquisition schemes, such as T_1 and T_2 weighting in MRI. By using this extraction approach, the voxel neighborhood information is not addressed in the feature set. Thus, it is possible

that two spatially distinct objects will be grouped into one cluster if they share approximately the same intensity level.

2. *Intensities and spatial coordinates.* The relationships between neighboring voxels can be included by incorporating the voxel's spatial coordinates into the feature set.
3. *Locality measures.* These features are measured over a small window centered around the voxel.

2.5.5.2 Post-processing

To obtain a final image segmentation, the output of the fuzzy clustering algorithm needs to be processed. The first possibility is to threshold the fuzzy membership images to obtain crisp segmentation. This approach means discards some information by transitioning from fuzzy to crisp segmentation. Nevertheless, beginning the process with the greatest amount of information (that may be reduced later) is recommendable to avoid errors introduced from starting directly with crisp segmentation (less information). One way to obtain crisp segmentation is to assign each pixel to a specific cluster for which the membership value is maximal [89]. An alternative is to identify the cluster of interest and to set a threshold for its membership values, obtaining a so-called α-cut of the cluster [85]. Furthermore, the membership values of a cluster can be used to enhance the contrast in the original image.

2.6 Wavelets

As wavelets are used for feature calculation in the clustering process, it is important to briefly detail the background of wavelet analysis.
Wavelets are small waves of varying frequency and limited duration [70]. Similar to sine and cosine functions in Fourier analysis, wavelets are used as basis functions in representing other functions. The basis functions are derived by scaling s and translation t [91] from a mother wavelet, $\psi(x)$, where:

$$\psi_{s,t}(x) = \frac{1}{\sqrt{s}}\psi\left(\frac{x-t}{s}\right).$$

It is a necessary condition that wavelets should integrate to zero:

$$\int_{-\infty}^{+\infty} \psi(x)\, dx = 0.$$

In contrast to the Fourier transform, where only the frequency information is provided, the wavelet transform is localized in both the frequency (via scaling) and spatial domain (via translation) [70]. Therefore wavelet analysis is suitable to analyze non-stationary signals.
Comparable to Fourier series expansion, the wavelet series expansion maps a function of a continuous variable into a sequence with coefficients W_ψ:

$$W_\psi = \frac{1}{\sqrt{s}}\int_{-\infty}^{+\infty} f(x)\, \psi\left(\frac{x-t}{s}\right)\, dx.$$

The continuous wavelet transform (CWT) is highly redundant and complex. As an illustration, a one-dimensional function $f(x)$ is represented by a two-dimensional function W_ψ.
If the function expansion is discrete (i.e. a sequence of numbers), the resulting expansion with complementary coefficients is called the *discrete wavelet transform* DWT. In the DWT, the redundancy and complexity of the continuous wavelet transform is decreased by reduction to a subset of the wavelets using a discrete set (power of two steps) of translations and scalings. Orthogonal basis wavelets are obtained starting from the mother wavelet $\psi_{0,0}(x)$:

$$\psi_{j,k}(x) = \frac{1}{\sqrt{2^{-j}}}\psi\left(\frac{x-2^{-j}k}{2^{-j}}\right) = 2^{j/2}\psi\left(2^j x - k\right) \begin{cases} j \in \mathbb{Z} \\ k = 0, 1, 2, \ldots, 2^j - 1 \end{cases} \tag{2.31}$$

There exist various wavelet families such as *Haar, Daubechies, Morlet, Mexican hat* and others, and their individual descriptions can be found in [92]. In the following section, the *Haar wavelet* is presented in more detail, since it best fits the requirements for 4D flow segmentation.

2.6.1 Haar wavelet

The Haar wavelet is the simplest and earliest proposed wavelet, was introduced by Alfred Haar [93]. The mother wavelet function $\psi_{0,0}(x)$ is defined as follows:

$$\psi(x) = \psi_{0,0}(x) = \begin{cases} +1 & 0 \leq x < 1/2 \\ -1 & 1/2 \leq x < 1 \\ 0 & \text{otherwise} \end{cases}$$

All child wavelets can be derived using equation 2.31. Examples of the Haar wavelet family are depicted in figure 2.35.
The Haar wavelet was selected as it provides, despite its simplicity, the best approach for the time courses of pulsatile flow and fluctuating noise (see figure 3.3) as encountered in 3D PC MR data. This data was the basis for segmentation and cluster analysis in this work.

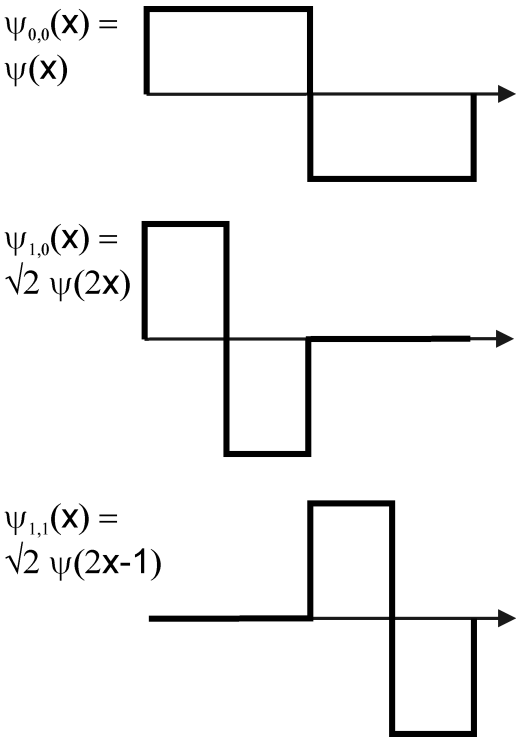

Figure 2.35: *The Haar wavelet: mother wavelet (top) and two child wavelets (middle, bottom).*

3 Processing of PC-MRI data

3.1 Pre-processing and background error corrections

In order to use PC-MR data for the analysis of blood flow, existent sources of errors such as eddy-currents or method-specific problems (e.g. velocity aliasing) should be eliminated in order to improve the data quality before further data processing or visualization.

3.1.1 Intensity non-uniformity correction

To correct for signal variations related to the multi-element coil used for data acquisition, a non-uniformity correction was performed on the magnitude data using LEMS (local entropy minimization with bicubic spline model), a technique introduced by Salvado et al. [60]. A brief description of the method is provided in the following, and further details regarding the algorithm and validation can be found in the original publication. The underlying MR signal model assumes that the intensity inhomogeneity is multiplicative, i.e. the image intensities are multiplied by the intensity inhomogeneity. Additionally, the MR image formation model includes additive noise. The noise has a Rician distribution, but for SNR > 3 noise can be approximated by a quasi-Gaussian distribution [94]. This approximation is valid for image areas containing tissues but not for those producing negligible signal, such as air [61]. According to this model, the observed image Y is obtained as

$$Y = X \times F + N, \tag{3.1}$$

where X is the inhomogeneity-free image, F is the bias field and N is noise.
The following overview of the correction method is taken from Salvado et al. [60]. First, background voxels are identified and a 4^{th} order polynomial function is fit to the non-background voxels in order to determine an initial estimate of the bias field F_0. Next, the bias field F is modeled as a bicubic spline with a rectangular grid of knots. The estimated F_0 is used for initialization followed by a piecewise optimization. Therefore, the knot k_1 with the highest corresponding F_0 value is used as the starting knot and the neighborhood (Ω_{k1}) with 8 adjacent knots is used for the optimization. Therefore, the

amplitude of the knot k_1 is adjusted such that the entropy, E, of the corrected image ($X = Y/F$) is minimized within the neighborhood Ω_{k1}. The entropy of an image X is defined as the following:

$$E(X) = -\sum_{\Omega} h_X(\Omega) \cdot \log\left(h_X(\Omega)\right),$$

where $h_X(\Omega)$ is the normalized histogram of the image X. Using the knot k_2 with the next highest F_0, the entropy of X is minimized in the region $\Omega_{k1} \cup \Omega_{k2}$. The process is repeated until all knots have been optimized. Additional passes are performed in the same manner, and the whole correction process stops when either the knots or the image entropy do not change significantly, or the maximum number of passes is reached.
In order to speed up the calculation process for time-resolved 3D data sets, bias field estimation was performed using only the first time frame. The calculated bias field was then used to correct all remaining time frames. An example of corrected versus uncorrected data is presented in figure 3.1.

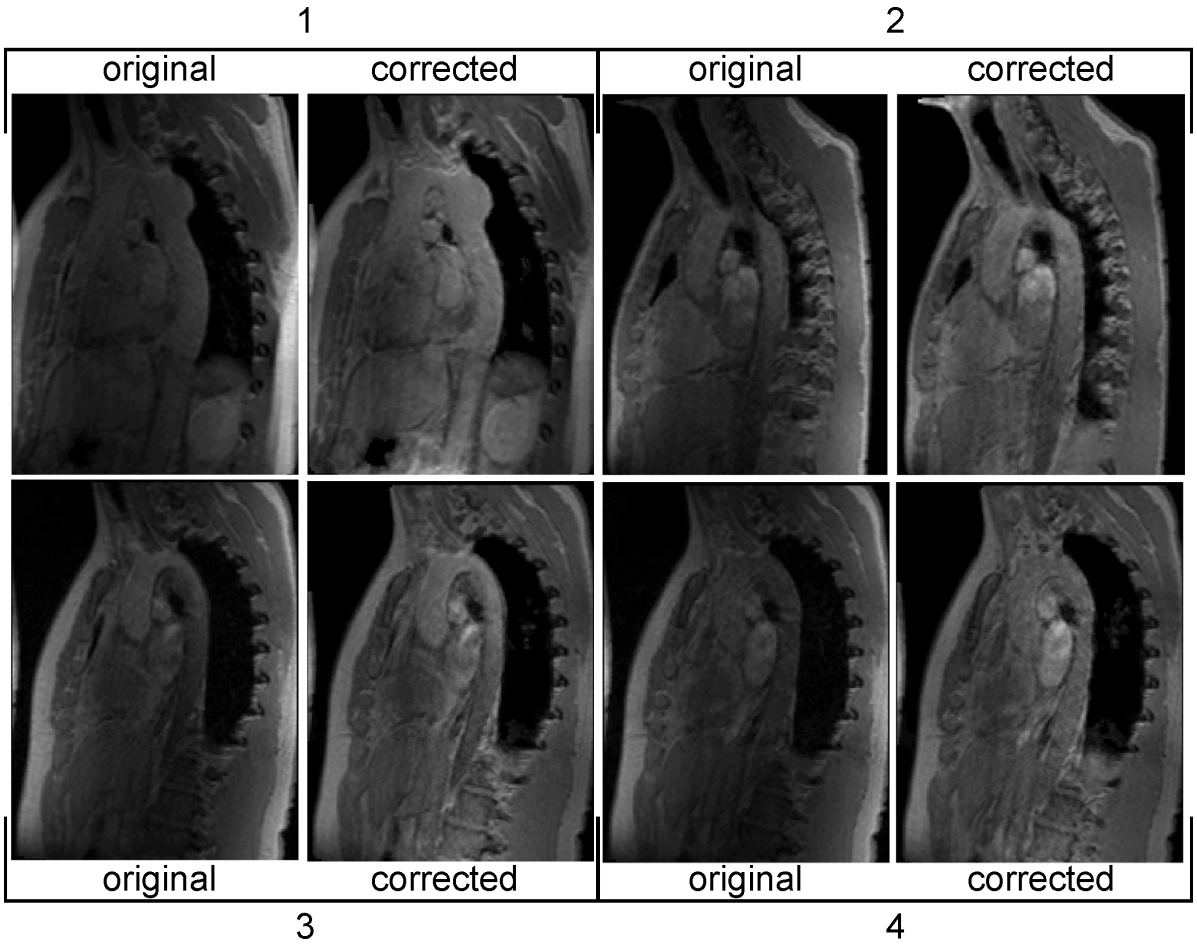

Figure 3.1: *Results for intensity non-uniformity correction demonstrated in four subjects.*

3.1.2 Noise masking

The areas with low MR signal intensity such as air in the lungs or outside the object, appear noisy on the velocity images, i.e. with randomly distributed intensity values. In order to improve data quality, noise masking was performed. Two noise masking approaches were implemented:

1. Noise masking can be performed by thresh-holding of the signal intensity in the magnitude data to exclude regions with low signal intensity (see figure 3.2), or
2. By comparing the standard deviation (*stdev*) of the velocity-time course for each pixel in the PC-MRI data set. Since velocity noise results in higher variations along the temporal direction compared to blood flow or static tissue (see figure 3.3), the standard deviation can be used to identify noisy regions [95] using thresholding.

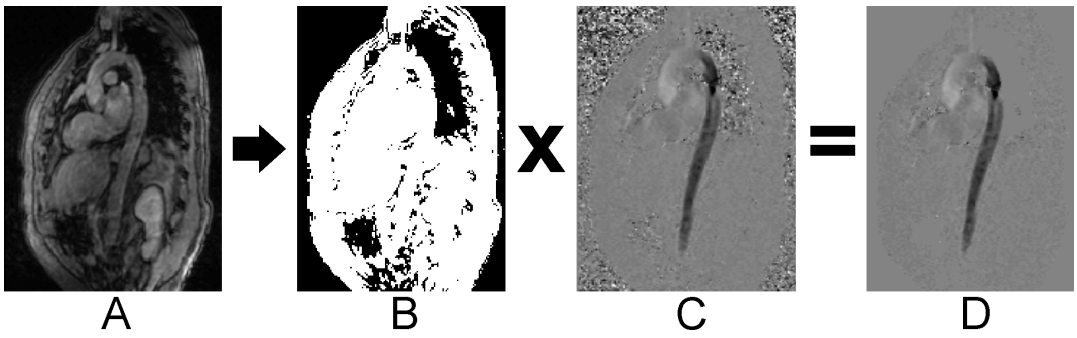

Figure 3.2: *A magnitude image (A) is used to generate a noise mask (B). This mask is then multiplied with the original velocity image (C) in order to mask out noise (D).*

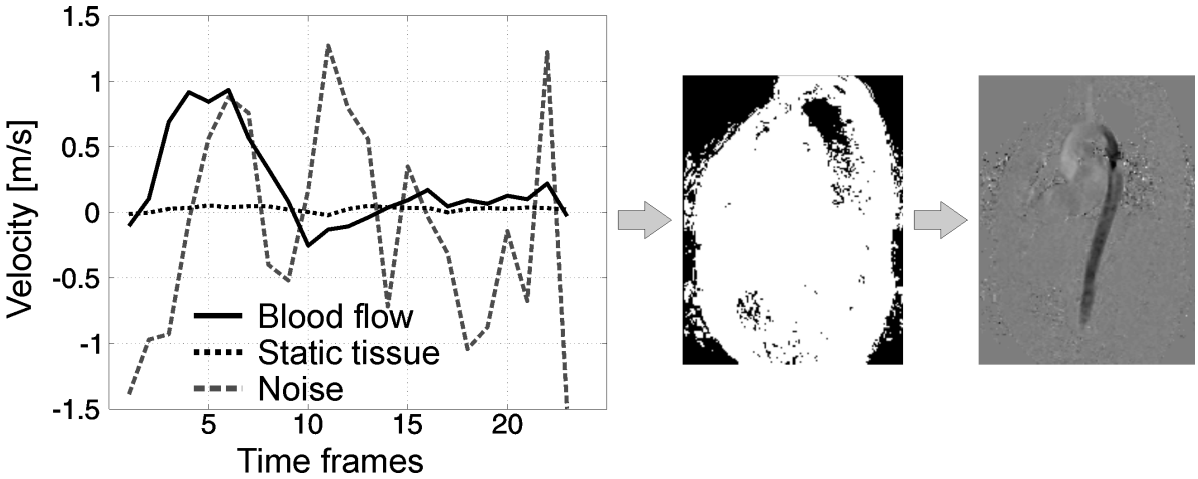

Figure 3.3: *Left: Typical velocity time course for blood flow (black solid line), static tissue (black dotted line) and noise (gray dashed line). The higher variability of the temporal dimension in noise pixels results in a larger standard deviation, which can be used to separate noise from tissue and blood. Middle: noise mask created on the basis of the standard deviation. Right: velocity after noise masking.*

For both cases, the adjustment of thresholds is performed interactively. Thus the determined noise pixels are set to zero and all others to one. The resulting mask is multiplied by the velocity data in order to reduce noise.

3.1.3 Eddy current correction

Eddy currents induce additional magnetic field gradients in the x-, y- and z-directions and thus leads to a phase shift. The correction of this shift (phase offset) can be performed from the acquired data by fitting and subtracting 1^{st}, 2^{nd}, or higher-order planes.

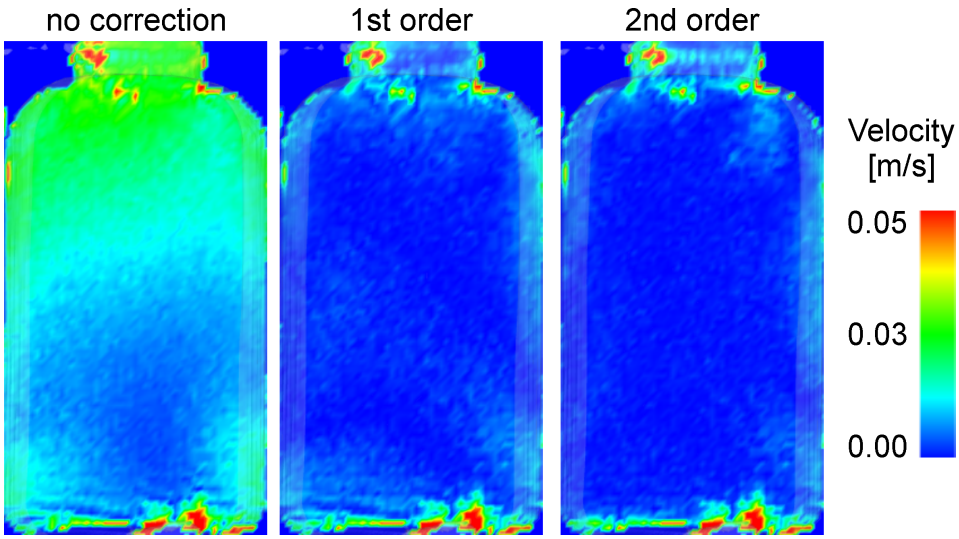

Figure 3.4: *Results of eddy current correction applied to a static phantom (water bottle). In a static phantom, the expected velocity is zero. However, eddy current influence results in a non-zero velocity (left image). Eddy current correction can improve the majority of the velocity values (middle and left images). Middle: phantom after 1^{st} order eddy current correction; right: data after 2^{nd} order eddy current correction.* Images are courtesy of Ramona Lorenz, University Medical Center Freiburg.

The correction process consists of three steps:

1. The separation of static tissue from blood flow and noise implemented with two different approaches.
   a) The standard deviation of the time course of each voxel can be used as it is smaller for static tissue than for blood flow or noise [96]. If the standard deviation is below a certain threshold (adjusted previously by the user), then the corresponding voxel is assigned to the static tissue voxels [56, 95].
   b) The PC-MRI data can be partitioned into three clusters: noise, blood flow/vessel and static tissue. The clustering approach is described in more details in the section 5.

2. A 2D fit to the previously determined static tissue of 1^{st} or 2^{nd} order is performed using a least squares method. This offset plane is computed for the last cardiac time frame only, since it takes place in late diastole and thus has the least cardiac motion.
3. The calculated offset plane is then subtracted from all pixels in each cardiac phase.

3.1.4 Phase unwrapping

Fully automated correction for velocity aliasing (phase wrapping), i.e. the measured velocity exceeded the user selected velocity sensitivity (v_{enc}), is based on the assumption that velocities measured in adjacent pixels in temporal or spatial directions should not differ by more than v_{enc} [95]. In the phase unwrapping process, each velocity direction is considered separately. Examples of phase wraps are shown in figure 2.31.
In the phase unwrapping process, the spatial and temporal neighborhood of each voxel is analyzed to detect signal variations, $\Delta\phi$, with magnitude greater than v_{enc}. When this condition is met, the spatial neighborhood (3x3) of the aliased pixel is searched to identify a pixel having no gradients $> v_{enc}$ during the time-course. This time-course is then used as a reference. If more than one pixel can be considered as a reference, than the one with the highest extreme value is selected in order to exclude static tissue and vessel wall [56]. The correction of the value is implemented as follows:

$$V_{new} = V_{old} - 2 \cdot v_{enc} \cdot (sign(V_{old})). \tag{3.2}$$

To improve the correction results, the above described steps can be repeated and the number of iterations can be adjusted by the user. An example of a phase wrapped versus a phase unwrapped velocity image is presented in figure 3.5.

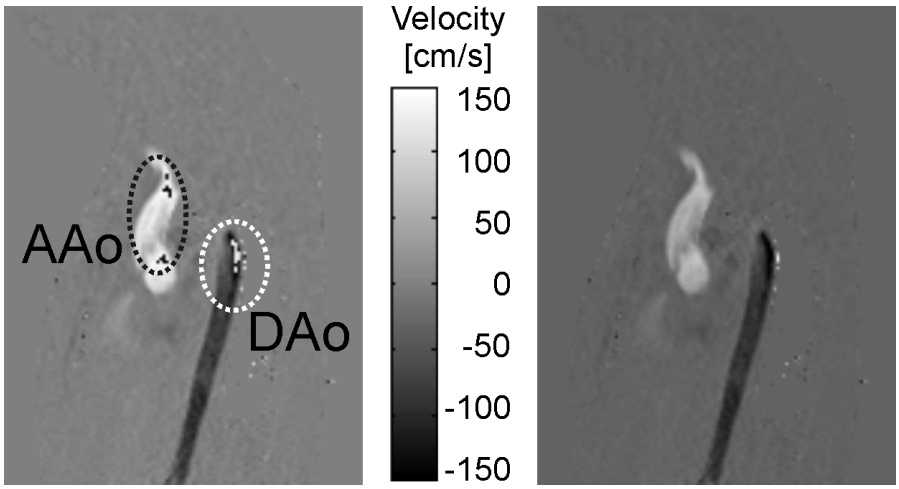

Figure 3.5: *Left: noise-masked velocity image with phase wraps in the ascending (black dotted ellipse) and descending aorta (white dotted ellipse). Right: the identical velocity image after fully automated phase unwrapping with 1 iteration.*

4 3D PC MR angiography

The methods and results of time-averaged 3D phase contrast MR angiography (PC-MRA) presented below have been partially published in J. Bock et al.: *4D Phase Contrast MRI at 3T: Effect of standard and blood-pool contrast agents on SNR, PC-MRA, and blood flow visualization*; in Magnetic Resonance in Medicine, 63(2):330–338, 2010.

4.1 Methods

In the following section the methods of extraction (section 4.1.1) and evaluation (section 4.1.2) of 3D PC-MRA data are described.

4.1.1 Different algorithms

In PC-MRI, magnitude data have high intensity values for static tissue and blood flow and low intensities for noise. In contrast, velocity data have highly variable values for noise, high intensities for blood flow during systole, and in contrast, values near zero for static tissue. By an appropriate combination of velocity and magnitude data, the blood flow can be accentuated while suppressing noise and static tissue in PC-MRA calculation.
Eight strategies for the calculation of time-averaged 3D PC-MRA (I^{PCMRA}) were implemented using the following relations [97, 98]:

$$I_1^{PCMRA}(\vec{r}) = \frac{1}{N}\sqrt{\sum_{t=1}^{N}(M_t(\vec{r})V_t(\vec{r}))^2}, \tag{4.1}$$

$$I_2^{PCMRA}(\vec{r}) = \frac{1}{N}\sqrt{\sum_{t=1}^{N}(M_t(\vec{r})V_t^2(\vec{r}))^2}, \tag{4.2}$$

$$I_3^{PCMRA}(\vec{r}) = \overline{M(\vec{r})}\ \overline{V(\vec{r})}, \tag{4.3}$$

$$I_4^{PCMRA}(\vec{r}) = \overline{M^2(\vec{r})}\ \overline{V(\vec{r})}, \tag{4.4}$$

$$I_5^{PCMRA}(\vec{r}) = \overline{M^2(\vec{r})}\ \overline{V^2(\vec{r})}, \tag{4.5}$$

$$I_6^{PCMRA}(\vec{r}) = \overline{M(\vec{r})\ V(\vec{r})}, \tag{4.6}$$

$$I_7^{PCMRA}(\vec{r}) = \overline{M^2(\vec{r})\ V(\vec{r})}, \tag{4.7}$$

$$I_8^{PCMRA}(\vec{r}) = \begin{cases} \overline{M_t(\vec{r})\ \sin\left(\frac{\pi V_t(\vec{r})}{2v_{enc}}\right)} & V_t < v_{enc} \\ \overline{M_t(\vec{r})} & otherwise \end{cases} \tag{4.8}$$

where t represents the measured time frame within the cardiac cycle with a total of N frames, $\vec{r}$ is the spatial location within the 3D volume. M and V denote magnitude and velocity data, respectively, and are calculated as follows:

$$V_t = \sqrt{V_{t,x}^2 + V_{t,y}^2 + V_{t,z}^2}, \tag{4.9}$$

$$\overline{V} = \frac{1}{N}\sum_{t=1}^{N} V_t, \tag{4.10}$$

where x, y, z are the velocity encoding directions in image coordinates (x = read, y = phase, z = slice). $\overline{M}$ is calculated in a similar manner as $\overline{V}$.
The computational methods can be divided into three basic types:

i. Algorithms using absolute velocity and magnitude weighting for each time frame and sum of squares (equations 4.1 and 4.2),
ii. algorithms using the temporal absolute velocity average with magnitude weighting (equations 4.3 - 4.7), and
iii. methods implementing piecewise pseudo complex difference (equation 4.8).

4.1.2 Evaluation of PC-MRA

The purpose of this study was to acquire data without and with two contrast agents, which differ in their molecular size and vascular dwell time, in order to:

1. Evaluate several new algorithms for the optimal extraction of PC-MRA data from flow-sensitive 4D MRI,
2. analyze the general effect of different contrast agents on vascular SNR and velocity noise,
3. evaluate PC-MRA quality in the subgroup with contrast agent administration compared to the reference standard (CE-MRA), and
4. study the effect of contrast agent on 4D flow visualization quality compared to visualization without contrast agent.

4.1.2.1 Experimental setup

Study population

30 healthy volunteers (mean age 23.7 years; eight female) were included in the study. Of all the 30 volunteers, 9 subjects received the extracellular contrast agent (ECA) and 10 subjects received the blood-pool contrast agent (BPA). Details on contrast agents are summarized in table 4.1. The remaining 11 subjects were examined without contrast agent administration.

		ECA	**BPA**
Generic name		Gadobenate dimeglumine [Gd-BOPTA]	Gadofosveset trisodium
Single dose	[mmol/kg]	0.1	0.03
Vial concentration	[mmol/ml]	0.5	0.25
Relaxivity at 3T	[$mmol^{-1}s^{-1}$]	5.5 ± 0.3 [99]	9.9 ± 0.5 [99]

Table 4.1: *Characteristics of extracellular (ECA) and blood-pool (BPA) contrast agents.*

Measurement parameters

All measurements were performed using a standard eight-channel phased-array surface coil on a routine 3T MR system (Magnetom Trio; Siemens AG, Germany).
For all 19 volunteers who received contrast agent, time-resolved CE-MRA (injection rate 3.5 ml/sec) of the thoracic aorta was performed during free breathing.
Additionally, flow-sensitive 4D MRI in a sagittal oblique 3D slab covering the entire thoracic aorta was performed for all 30 volunteers, using a respiration-controlled and ECG-gated RF-spoiled gradient echo sequence [51]. Pulse sequence parameters for both measurements are summarized in table 4.2. For volunteers who received contrast agent, flow-sensitive 4D MRI measurements were performed 20 ± 7.5 min after contrast agent administration.

4.1.2.2 Comparison of different algorithms

PC-MRA was calculated for 9 subjects with ECA using 8 different algorithms as described in 4.1.1 without applying any pre-processing and after noise masking (section 3.1.2) and static tissue removal (section 3.1.3). PC-MRA were compared qualitatively. Additionally, vessel-background contrast (CNR, equation (4.11)) was quantified for all algorithms using region of interest (ROI) analysis of vessel lumen and background signal

		CE-MRA	**PC-MRI**
Voxel size:			
- Phase-encoding direction	[mm]	2.22-2.24	2.57-2.93
- Readout direction	[mm]	1.25	1.48-1.69
- Slab direction	[mm]	1.5-1.7	2.6-3.5
$FOV_{phase \times freq}$	[mm^2]	400 × 400	300-320 × 200-240
Matrix size		320 × 320	192 × 120-144
Slab thickness	[mm]	96-108.8	61.6-84
# of slices/slab		64	22-24
Temporal update	[s]	2.84-2.87	N/A
Temporal resolution	[ms]	N/A	48.8
TE/TR	[ms]	0.78-0.88/2.08-2.13	3.67/6.1
Bandwidth	[Hz/pixel]	1040	480
Flip angle	[°]	8-25	15
Acquisition time	[min]	≈ 1	9-23
v_{enc}	[cm/sec]	N/A	150

Table 4.2: *Pulse sequence parameters used for CE-MRA (left) and for time-resolved 3D PC-MRI (right). (N/A = not applicable).*

(see figure 4.1):

$$CNR = mean\,(vesselROIs) - mean\,(backgroundROIs)\,, \tag{4.11}$$

where *mean* denotes the average signal intensity of all pixels within the ROI.

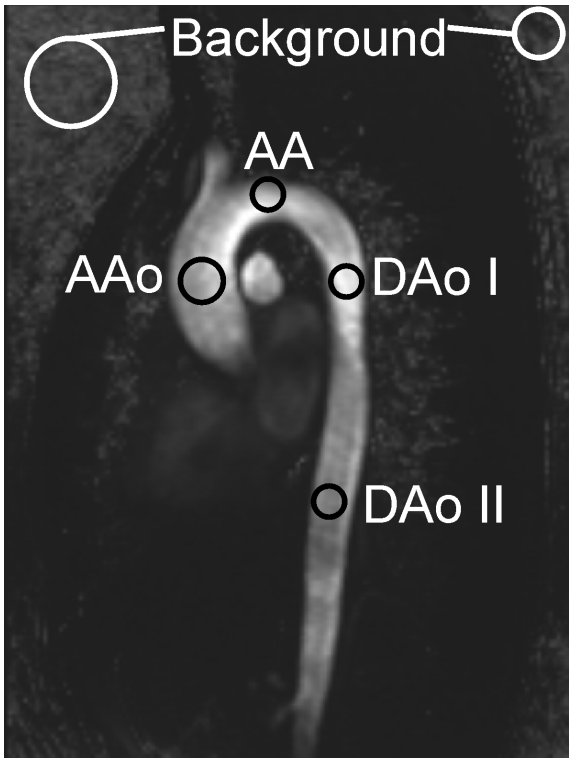

Figure 4.1: *ROI used for SNR and CNR calculations: vessel ROIs = black circles, background ROIs = white circles.*

4.1.2.3 Comparison with standard CE-MRA

In the subgroup of 19 volunteers who received contrast agent, time-averaged PC-MRA was derived using equation (4.1). In order to exclude regions with low signal intensity such as air in the lungs and outside the object, noise masking was performed by thresholding of the signal intensity in the magnitude images. The threshold value was set to 10% of the maximum value in the magnitude data.
Quantitative data analysis was performed by comparing the diameters of the thoracic aorta and supra-aortic branches (brachiocephalic artery BCA, left common carotid artery LCCA, left subclavian artery LSCA) in PC-MRA with CE-MRA as the reference standard. For CE-MRA the time frame with maximal arterial enhancement was chosen for comparison.
Diameters were measured by two independent readers in the ascending aorta (AAo) and descending aorta (DAo) at the level of the pulmonary artery and at the aortic arch (AA) at the 12 o'clock position as well as at the 3 supra-aortic branches (BCA, LCCA, LSCA) 1cm above the aortic arch (see figure 4.2 C). For the exact evaluation of the diameters, a standard diagnostic workstation (TIANI, Tiani Medgraph, Austria) was used. In order to accurately define diameters, a multi-planar reformatting tool was employed. Planes were positioned normal to the vascular lumen. On the resulting axial analysis plane, two diameters for each location were averaged to represent the local diameter.
In order to evaluate the agreement between vessel diameter measurements in PC-MRA and in CE-MRA, Bland-Altman plots were created [100, 101]. The data measured with CE-MRA were taken to be the reference standard. Furthermore, the ratios (diameters PC-MRA /diameters CE-MRA) for each subgroup were calculated.

4.1.2.4 Influence of different contrast agents

For all 30 cases, time-averaged PC-MRA was derived and pre-processed as described above (4.1.2.3).

SNR analysis

Since flow-sensitive 4D MRI requires long scan times (up to 20 min), it is not possible to acquire all the data during the first pass of the contrast agent. To evaluate the general influence of contrast agent remaining in the vascular system during the flow-sensitive 4D MRI scan, the signal-to-noise-ratios (SNR) of flow-sensitive 4D magnitude data were measured for each volunteer. Relative SNR evaluation could be carried out using different regions of interest (ROIs) for the estimation of signal intensity and noise [102]. In the central slice of the 3D magnitude data for each time frame, three ROI

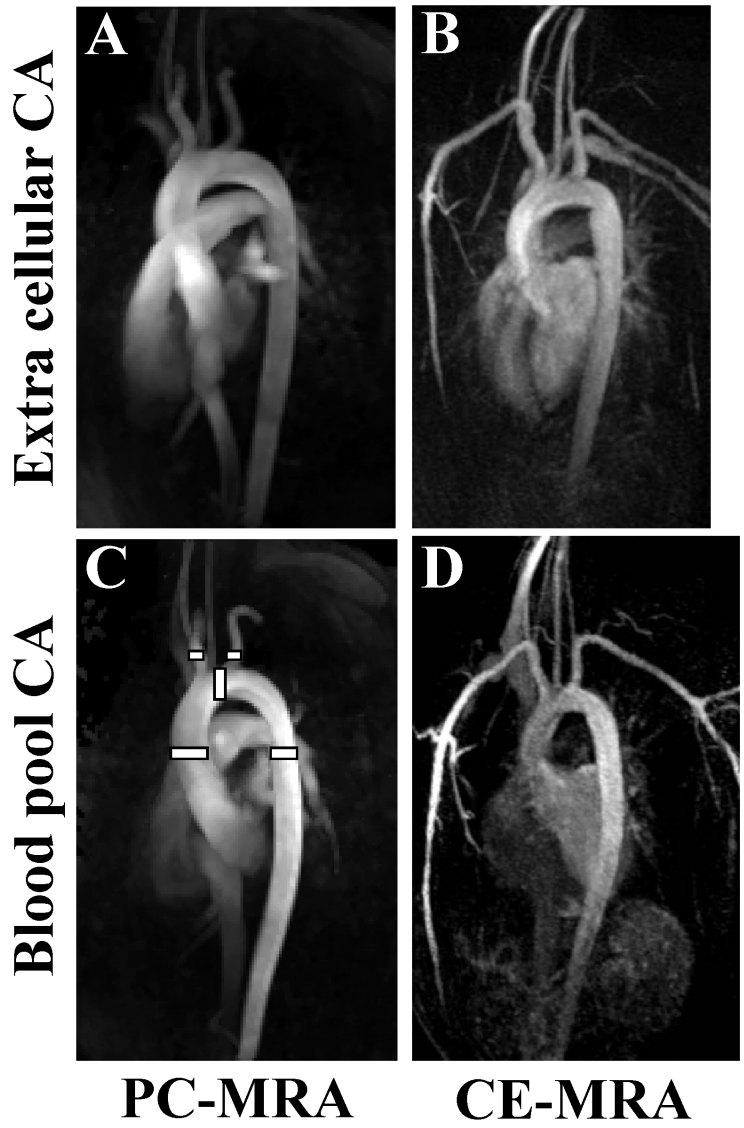

Figure 4.2: *Left column: maximum intensity projections (MIPs) derived from PC-MRA data for data with extra cellular CA (A), with blood pool CA (C); Right column: MIPs derived from CE-MRA for data with extra cellular CA (B), with blood pool CA (D). Left lower image (C): Positions used for diameter measurements (solid gray lines) in the thoracic aorta and supra-aortic branches. Note that the full left and right subclavian arteries as seen in B and D are not visible in the PC-MRA images since a narrow sagittal oblique volume was used for data acquisition.*

were interactively placed within the vessel lumen in the ascending aorta, aortic arch, and descending aorta. Additionally, two regions were positioned in the background of the image (figure 4.3) and SNR was calculated as:

$$SNR = \frac{mean(vesselROIs)}{SD(backgroundROIs)}, \tag{4.12}$$

where *mean* denotes the average signal intensity and SD the standard deviation of the signal intensity of all pixels within the ROI.
Since the number of time frames acquired during the cardiac cycle varied for each volunteer (mean 13.2 time frames), averaged SNR was calculated among volunteers of each subgroup for the time frames 1-13. In order to assess SNR differences, an unpaired t-test was performed for each subgroup with every other subgroup. A p value smaller than 0.05 was considered statistically significant.

Figure 4.3: *ROIs used for SNR calculations (vessel ROIs = solid line circles, background ROIs = dotted line circles). The dashed line represents a middle line along the thoracic aortic lumen used for measurements of individual thoracic aorta length, starting at the level of the lower edge of the pulmonary artery and ending in the descending aorta at the level of the vertebral end plate of the 11th thoracic vertebra.*

Flow Visualization

The effect of different contrast agents on 3D flow visualization was investigated using a commercial visualization tool (EnSight; CEI, USA). For quantitative data comparison, an isosurface representing the vessel walls was created from PC-MRA. For all 30 volunteers, the isovalue threshold was individually set to ensure that at least the first supra-aortic branch was fully visualized (figure 4.4). Flow visualization was performed using 3D stream-lines which resemble traces tangential to the measured velocity vector field for a given time-frame within the cardiac cycle [103, 104].
An emitter plane (30x30 mm) with 150 equidistantly spaced emitter points was manually placed in each data set in the descending aorta at the level of pulmonary artery and streamlines were emitted up- and downstream for all time frames (figure 4.4 A). All streamlines were restricted to an isovolume defined by the PC-MRA data by setting all velocity values outside of the created isovolume equal to zero.
Analysis of 3D visualization quality was performed using following evaluation of streamlines :

1. Four further planes were placed 5 cm, 10 cm, 15 cm and 20 cm downstream in the descending aorta (figure 4.4 B). Both the number of effectively emitted streamlines and the relative number of streamlines which reached each of the four planes were determined for all time points.
2. The length of detected streamlines was determined and normalized with respect to the individual length of the thoracic aortic lumen. Therefore for each volunteer the individual length of the thoracic aorta was determined by interactively measuring the end-to-end lumen distance starting in the ascending aorta at the level of the lower edge of pulmonary artery and ending in the descending aorta at the level of the vertebral end plate of the 11th thoracic vertebra (see figure 4.3). For these length measurements a standard diagnostic workstation (TIANI) was used. The accuracy is expected to be in order of the magnitude of the data's spatial resolution, which was approximately 2.5 mm.

Multiple comparison tests were performed in order to determine statistically relevant differences.

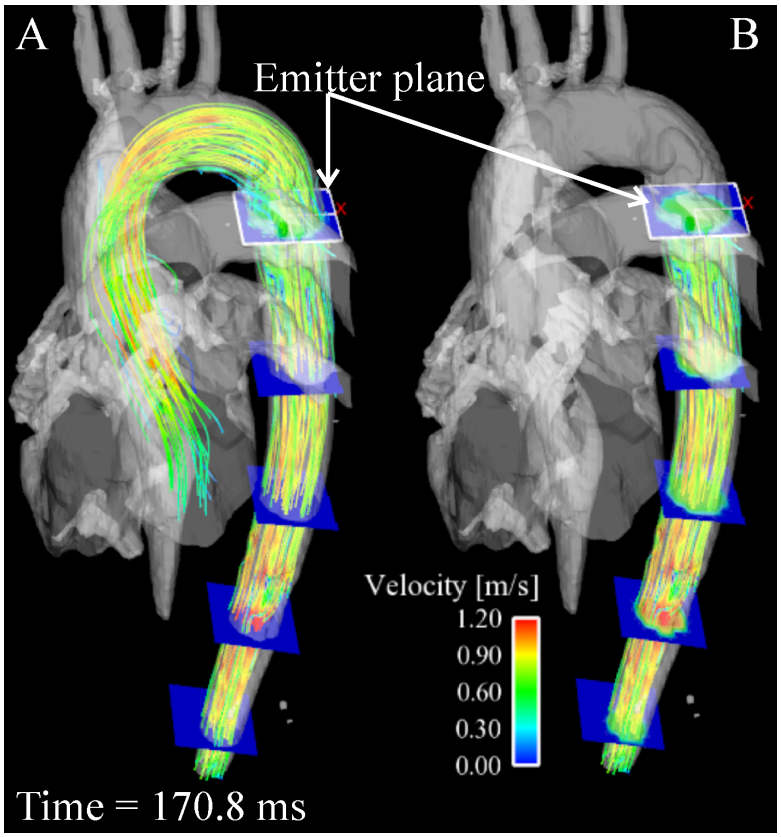

Figure 4.4: *A) 3D Streamlines inside the PC-MRA isosurface originating from the emitter plane down and upstream, B) 3D Streamlines emitted from the emitter plane only downstream and 4 further planes (5, 10, 15, 20 cm distant from emitter plane) used for data analysis.*

4.2 Results

4.2.1 Comparison of different algorithms for PC-MRA

Figure 4.6 shows results for PC-MRA calculation based on flow-sensitive 4D-MRI after the injection of extracellular contrast agent. Comparing data without (upper row) and after pre-processing (lower row) it is evident that PC-MRA profits from applying noise masking and removing static tissue. Note that algorithms 4, 5 and 7 provide good background suppression even without pre-processing. For pre-processed data, it is evident that best background suppression was achieved by algorithms 2, 5 and 7, while algorithms 1, 6 and 8 demonstrated more homogeneous aortic lumen. Additionally, algorithm 8 shows best depiction of smaller vessels.
These findings are also reflected in the quantitative lumen-background contrast analysis in figure 4.5 with maximum contrast for good lumen depiction in combination with high background suppression for algorithms 1, 6 and 8.

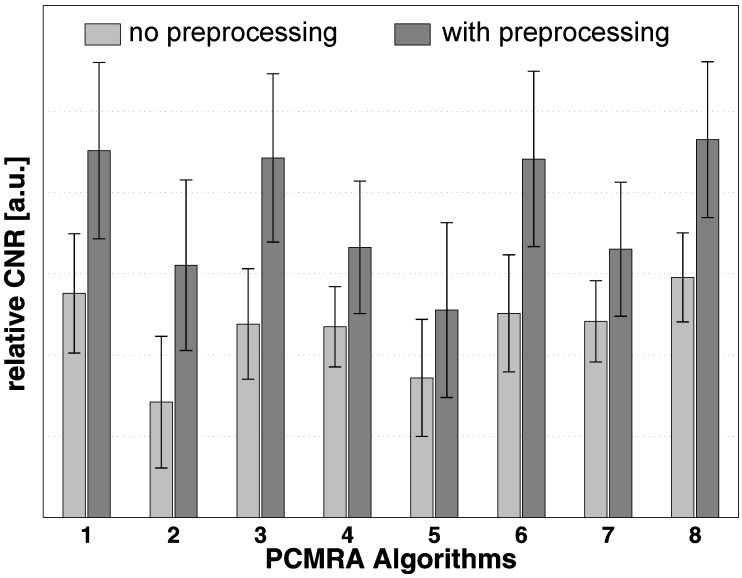

Figure 4.5: *CNR analysis results for 8 different PC-MRA calculations without pre-processing (light gray) and with pre-processing (dark gray). The data were averaged over 10 healthy subjects with extracellular contrast agent.*

4.2.2 Comparison to standard CE-MRA

Measurements of vessel diameters in thoracic aorta (figure 4.7, upper part) and supra-aortic branches (figure 4.7, lower part) presented as Bland-Altman plots demonstrated good agreement with the reference standard CE-MRA for both contrast agents (extracellular ECA and blood-pool contrast agent BPA). Improved PC-MRA performance was evident for BPA, particularly for the smaller supra-aortic branches. No clear trend

Figure 4.6: *PC-MRA calculations with and without pre-processing, performed on one data set (with extracellular contrast agent) using different algorithms 1-8 as listed in section 4.1.1.*

toward over- or underestimation of the vessel lumen diameter was observed, which is also reflected by the diameter ratios as shown in table 4.3.

	Thoracic aorta	**Supra-aortic branches**
ECA	0.99 ± 0.05	1.03 ± 0.04
BPA	1.02 ± 0.18	0.98 ± 0.13

Table 4.3: *Diameter ratios: diameters PC-MRA/diameters CE-MRA for thoracic aorta and supra-aortic branches.*

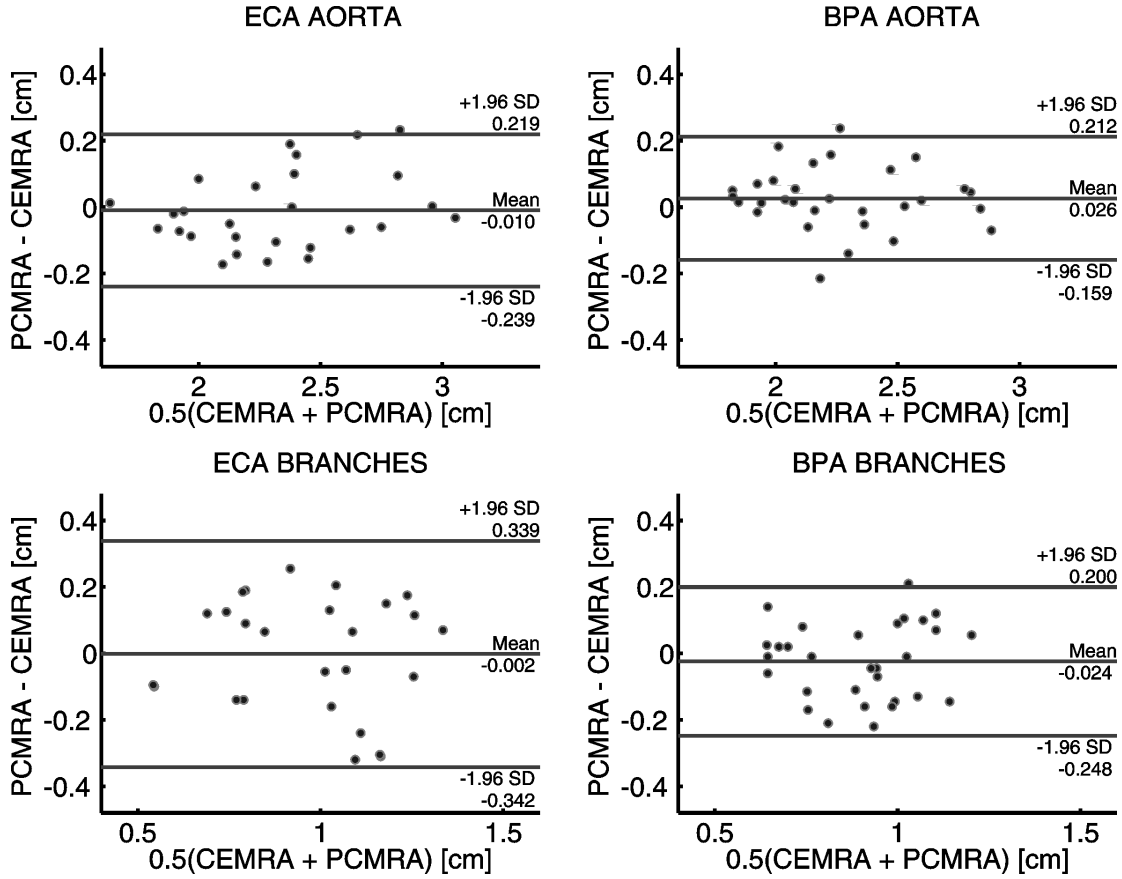

Figure 4.7: *Bland-Altman plots for thoracic aortic and supra-aortic diameters measured in PC-MRA data compared to the reference standard CE-MRA (left: thoracic aorta [upper plot] and supra-aortic [lower plot] diameters from data with ECA, right: thoracic aorta [upper plot] and supra-aortic [lower plot] diameters from data with BPA).*

4.2.3 Applications of different contrast agents

4.2.3.1 SNR analysis

The results for SNR analysis of the flow sensitive 4D MRI magnitude data are shown in figure 4.8. All data is displayed as an average over all volunteers from each subgroup

(without contrast agent injection *no CA*, with *ECA* and with *BPA*) for 13 consecutive time frames within the cardiac cycle. Data with contrast agent administration provided significantly higher SNR compared to data without contrast agent: $p < 0.0001$ for no CA/BPA and $p = 0.003$ for no CA/ECA. Differences in SNR between data with *ECA* and *BPA* remained insignificant, but improved SNR value for blood pool contrast agent was seen for all time frames.

As expected, due to higher blood-flow velocity during the systolic period and thus increased in-flow signal enhancement, SNR as a function of time reflected the pulsatile nature of blood flow and generally increased SNR during systole was observed.

Using equation 2.19, the standard deviation of measured velocities was also estimated from calculated SNR data. The results show a reduction of velocity noise by 32.3 ± 18.8% for data with ECA and 39.2 ± 13.1% for data with BPA compared to the data acquired without contrast agent administration.

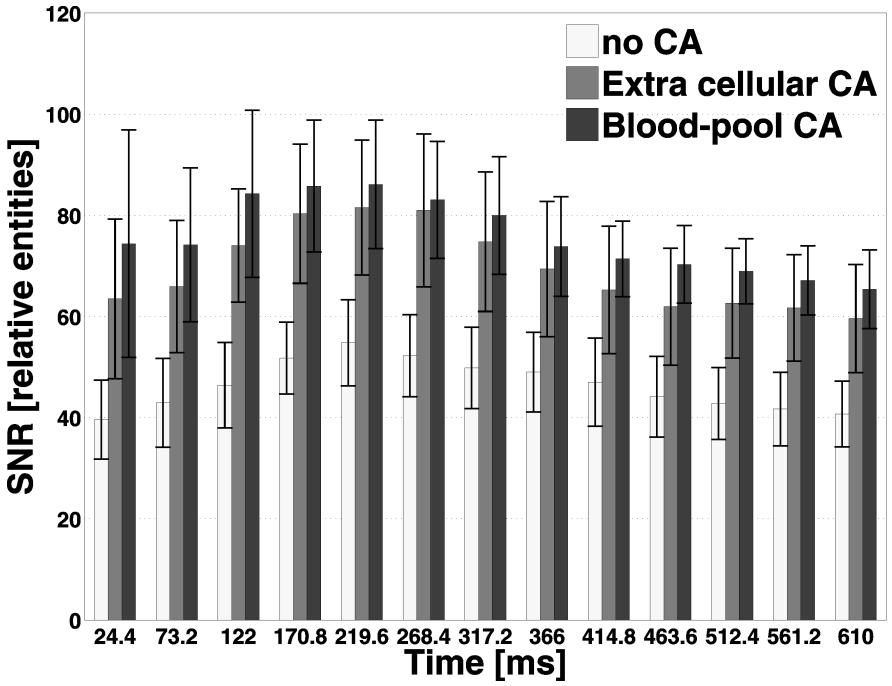

Figure 4.8: *Results for time-resolved SNR analysis for data without contrast agent (white), with extracellular CA (gray), and blood pool CA (black).*

4.2.3.2 Flow visualization

Figure 4.9 shows results of isosurface-rendered 3D-PCMRA data and systolic 3D stream lines derived from the flow-sensitive 4D MRI data. Improved quality of the 3D thoracic aortic surface for data including contrast agent can clearly be seen.

The results of visualization quality analysis using relative length of stream lines are

shown as the mean trace length over time in figure 4.10. Contrast agent data showed a trend toward improved stream-line length during systolic time frames (duration approximately 300 ms). Multiple comparison tests revealed no significant improvement.

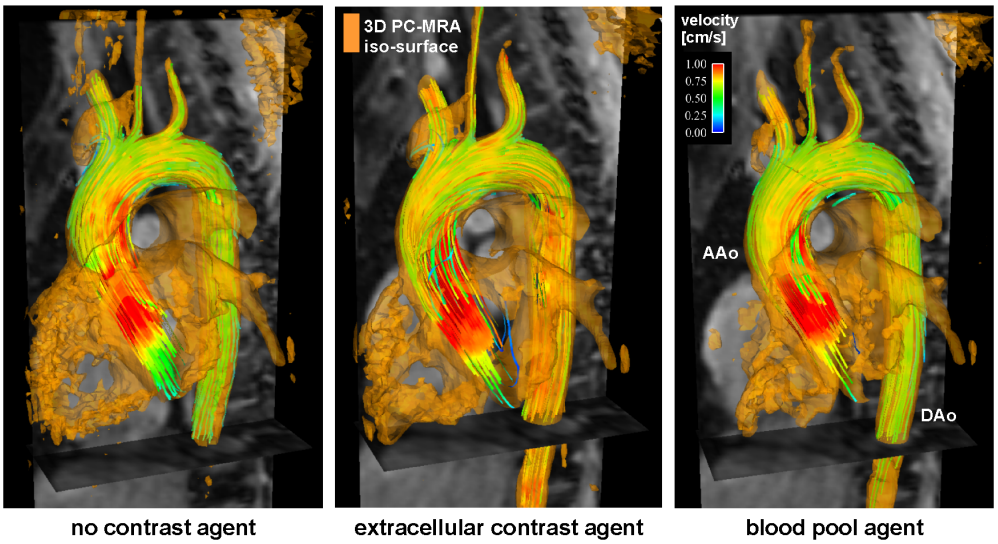

Figure 4.9: *3D Blood flow visualization in the thoracic aorta using systolic stream lines (at 122 ms after R-wave) and isosurface rendering of PC-MRA data. Best results, i.e., only minor background PC-MRA signal and improved downstream tracing of velocities, were achieved for data with contrast agents.*

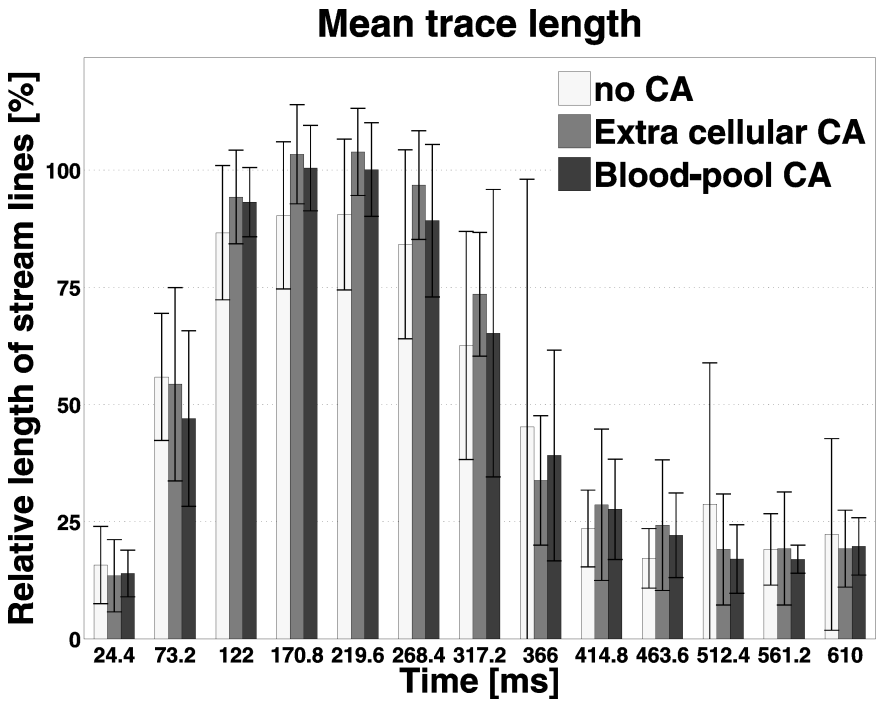

Figure 4.10: *Evaluation of 4D visualization quality: relative length of stream lines (normalized to the individual span of the thoracic aorta) for all cardiac time frames.*

5 Clustering of PC-MRI data

Clustering algorithms (here fuzzy c-means, FCM) classify the image by grouping similar data points in the feature space into clusters [89]. For the calculation of temporally segmented aortic PC-MRA, the aim was to group voxels of the time-resolved 3D PC volume into 3 clusters labeled as noise, static tissue and flow/vessel lumen for each time frame.
This classification allows a fully automatic separation of the major data components and is useful for the further processing of the data. Thus, the "noise" cluster can be used for automatic noise masking or estimation of background noise for the calculation of SNR; "static tissue" can be used for automatic eddy current correction (s. section 3.1.3); and "vessel" cluster depicts 4D segmentation of the moving aorta and can be used for further calculation of hemodynamic parameters (s. chapter 6).

5.1 Methods

In the following section the methods used for clustering of time-resolved 3D PC-MRI data are presented.

5.1.1 Data pre-processing

Magnitude data

Due to the characteristics of the MR imaging, similar tissue types have also similar signal properties, e.g. similar gray values in the images. However, intensity non-uniformity artifacts can occur (s. section 2.3.2.2) in the magnitude images and need to be corrected before the clustering process. The correction approach is described in section 3.1.1.

Velocity data

One major challenge in clustering of time-resolved PC-MRI data is that blood flow velocity in diastolic time-frames is low, thus the distinction between static tissue and vessels becomes challenging, since there is no difference in gray values between vessels

and static tissue.

In order to account for this, information derived from the velocity data from a time frame with high flow needs to be propagated to the time frames with low flow. The idea of the propagation process is to use information derived from the systolic time frames to influence the values in the diastole. The propagation is performed as follows:

1. Determine peak systolic time frame (TF_{peak}): calculate mean value of sum of squares PC-MRA (equation 4.1) over volume for each time frame and choose the position of the maximum in the time course as peak systolic time frame.
2. For all post-systolic time frames ($t > TF_{peak}$) following propagation approach is used:
   a) use TF_{peak} as the start time frame,
   b) calculate mean value from each voxel's neighborhood m_t within the neighborhood NB = [x-1:x+1, y-1:y+1, z-1:z+1, t-1:t]:

$$m_t = \frac{1}{N} \sum_{k \in NB} vox_{k,t}, \tag{5.1}$$

      where N is the number of the neighbors and vox is the voxel,
   c) calculate new value for each voxel in the successor time frame $(t + 1)$ as follows:

$$vox_{t+1} = \frac{m_t + vox_{t+1}}{2}. \tag{5.2}$$

   d) Repeat steps 2b and 2c recursively for all post-systolic time frames.
3. For all pre-systolic time frames ($t < TF_{peak}$) following propagation approach is used:
   a) use TF_{peak} as the start time frame,
   b) calculate mean value from each voxel's neighborhood m_t within the neighborhood NB = [x-1:x+1, y-1:y+1, z-1:z+1, t:t+1]:

$$m_t = \frac{1}{N} \sum_{k \in NB} vox_{k,t}, \tag{5.3}$$

   c) calculate new value for each voxel in the predecessor time frame $(t - 1)$ as follows:

$$vox_{t-1} = \frac{m_t + vox_{t-1}}{2}. \tag{5.4}$$

   d) Repeat steps 3b and 3c recursively for all pre-systolic time frames.

5.1.2 Feature extraction

The following section provides an overview over features that have been implemented in this work as well as their properties, advantages and disadvantages. Features were calculated for each voxel and scaled in the range of [0...1] to provide identical value range for all data. Scaling was performed in two ways: "minmax" scales each feature so that minimum becomes 0 and maximum becomes 1; "stdev" scales each feature so that mean value is 0 and two standard deviations is 1.

Voxels intensity features

The following signal intensity based features were constructed:

- **Non-uniformity corrected magnitude data** (s. section 3.1.1): In the non-uniformity corrected magnitude images, noise regions are typically of low signal intensity (intensity value close to 0) and regions with static tissue and flow are having values ≈ 1. Therefore, if a pixel has a intensity closer to 0, it has higher probability of being noise pixel, whereas if pixels have intensities closer to 1, then they are probable vessel or static tissue pixels. Thus this feature is used to identify noise in the data.
- **Sum of squares PC-MRA**: Combination of magnitude (M_t) and speed (V_t) information

$$I_{PCMRA}\left(\vec{r}\right) = \left(M_t(\vec{r})V_t(\vec{r})\right)^2 . \tag{5.5}$$

  Scaled with "stdev" approach, regions with flow show intensity values close to 1, static and noisy regions have intensity values close to 0. By using velocity vector magnitude (speed) V_t, aliased (wrapped) velocity values do not have any undesired influence on the feature values.
  This feature helps to distinguish between vessel and noise/static tissue.
- **Pseudo-complex PC-MRA**:

$$I_{PCMRA}\left(\vec{r}\right) = \begin{cases} M_t(\vec{r})\ \sin\left(\frac{\pi V_t(\vec{r})}{2v_{enc}}\right) & V_t < v_{enc} \\ M_t(\vec{r}) & otherwise \end{cases} \tag{5.6}$$

  Scaled with "stdev" approach, regions with flow have intensities values close to 1, static and noisy regions show intensity values close to 0. Similar to *sum of squares PC-MRA*, aliased voxel don't influence this feature allowing for differentiation between flow and static tissue/noise. Three different v_{enc} threshold were used: $\frac{1}{2}$, $\frac{1}{3}$ and $\frac{1}{4}$ of the original v_{enc} used to acquire the data.

Features derived from locality measures

Locality measures are features, that are measured over a small window centered around the voxel.

- **Velocity vector direction homogeneity**, VDH:

$$VDH\left(\vec{k}\right) = \sum_{j=1}^{w} d_i\left(j\right), \tag{5.7}$$

  where d_i represents the difference in orientation between two velocity vectors $\vec{v_i}$ and $\vec{v_k}$, where the interrogation window is centered on k:

$$d_i\left(\vec{k}\right) = \frac{\vec{v_i} \cdot \vec{v_k}}{\|\vec{v_i}\| \cdot \|\vec{v_k}\|}.$$

  For noise, where the orientation of velocity vector directions is random, VDH tend to be 0, for static tissue and blood flow VDH has a high value close to 1 [76]. Thus this feature is useful to identify the noise. The main disadvantage of this feature is, that interrogation windows with aliased velocity vectors do not have high VDH value as expected for blood flow, but show low VDH values because of the different orientations of the neighboring vectors.

- **Vector field standard deviation**, SD: Standard deviation of the velocity vector field within the scanned window, evaluated for each velocity component [76]:

$$SD = \sqrt{\frac{\sum_{j=1}^{3}\left(v\left(\vec{k}, j\right) - \mu\left(j\right)\right)^2}{3}}, \tag{5.8}$$

  where μ is the mean of velocity component of each the three-vector components within the interrogation window w. SD feature has high values for noise, but unfortunately for areas with aliased velocity components as well. Blood flow and static tissue have SD-values around zero. Similar to VDH, the SD-feature can be used to separate noise from blood flow and static tissue.

- **Haar wavelet coefficients** (s. section 2.6.1): mean value of the Haar wavelet coefficients (for 2 scaling values) of the speed-time course in a temporal neighborhood of 5 voxels. The regions with noise or flow have values close to 1, static regions have values close to 0. This feature is helpful for separation of static tissue from blood flow and noise.

The most appropriate feature combination has been determined empirically and consists of 4 features: non-uniformity corrected magnitude data, pseudo-complex PC-MRA, sum

of squares PC-MRA and Haar wavelet coefficients. All chosen features are not susceptible to the possible velocity aliasing, making them more robust in comparison with features using vector orientation.

5.1.3 Spatio-temporal FCM algorithm

One can assume that adjacent pixels in PC-MRI images are highly correlated, therefore these neighboring pixels have a high probability of belonging to the same cluster [89]. However, this spatial relationship is not used in a standard FCM algorithm. Chuang et al. [89] has introduced a spatial function incorporated into membership function. In the work presented here, the FCM algorithm has been modified by incorporating spatio-temporal neighborhood information into the membership assignment function. The spatio-temporal function has been defined as following:

$$h_{ik} = \sum_{n \in NB(x_k)} u_{in}, \tag{5.9}$$

where $k \in NB(x_k)$ represents the spatio-temporal neighborhood of the pixel x_k. Just like the membership function, the spatio-temporal function h_{ik} represents the probability that pixel x_k belongs to ith cluster. The function h_{ik} for a pixel x_k is large, if the majority of its neighboring pixels belongs to the same cluster [89]. This function is incorporated into the membership function as follows:

$$u_{ik}^{'} = \frac{u_{ik}^{q}\, h_{ik}^{s}}{\sum_{m=1}^{c} u_{mk}^{q}\, h_{mk}^{s}}, \tag{5.10}$$

where q and s are the parameters controlling the relative influence of both functions. Inserting q=1 and s=0 will result in an algorithm identical to the conventional FCM. The modified FCM is a two-pass process. In the first pass, the membership function u_{ik} is calculated using standard FCM algorithm. In the second pass, the modified membership function $u_{ik}^{'}$ is computed. In the next iteration, FCM proceeds with the modified membership function $u_{ik}^{'}$. The iteration process is stopped when a predefined convergence criterion has been satisfied. Subsequently, each voxel is assigned to a specific cluster for which the membership was maximal. The modified FCM helps to yield more homogeneous regions and to remove outliers in the PC-MRI data [89].
In the presented work following settings were used:

- spatio-temporal neighborhood: 1 voxel in each ± direction of spatio-temporal directions (x, y, z, t),
- q=1 and s=1, and

- convergence criterion: the maximum difference between cluster centers at two successive iterations is $< 0.2\%$

5.1.4 Post-processing

A spatio-temporal FCM algorithm was applied until convergence was achieved. Subsequently, voxels were assigned to the vessel cluster if their membership values in vessel cluster were ≥ 0.75 (see section 2.5.5.2).
A flood fill algorithm which determines the volume connected to a given voxel, was applied in order to exclude all voxels not connected to the vessel tree. Furthermore to improve the segmentation of diastolic time frames, voxels in the peak systolic time frames were labeled according to their distance from the vessel boundaries; core voxels (with distance > 3 voxels) were copied to all diastolic time frames. Additionally, a 3D holes closing algorithm was applied for each time frame.
The data processing work-flow is illustrated in figure 5.1.

5.1.5 Experimental setup

The purpose of this study was to extract time-resolved 3D PC-MR angiography from ECG gated PC-MRI data with 3-directional velocity encoding using fully automated feature based fuzzy clustering for dynamic aortic lumen segmentation.

Study population

11 young healthy subjects (mean age 24.6 years, 4 females) and 11 patients with different cardiovascular pathologies (mean age 29.7 years, 5 females; 8 patients with coarctation, 1 with aortic aneurysm, 1 with bicuspid aortic valve and 1 with aortic insufficiency) were included in our study. All patients received contrast agent.

Measurement parameters

Data were acquired on 1.5T and 3T systems (Avanto and TRIO, respectively, Siemens, Germany) using an ECG gated and respiration controlled rf-spoiled gradient echo phase contrast sequence with three-directional velocity encoding. Imaging parameters are summarized in table 5.1.

Data Analysis

For all subjects, time-resolved PC-MRA was calculated as described above (sections 5.1.1-5.1.4). To enable the calculation of hemodynamic parameters (flow, mean velocities, etc.) in the aorta only, automatic removal of the pulmonary system was performed

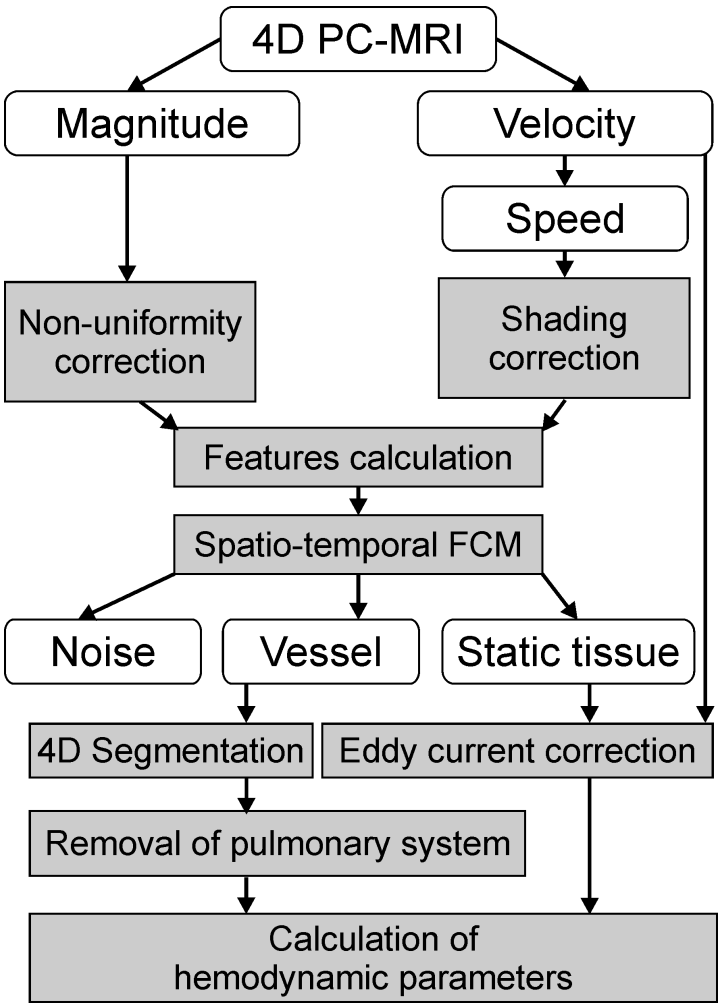

Figure 5.1: *Flow chart for processing of time-resolved PC-MRI data.*

based on vector field homogeneity [76] and a subsequently applied flood fill algorithm as described in more details in section 6.1.1.1. Voxels classified by FCM algorithm as static tissue were used for eddy current correction of the velocity data [62]. The data processing work-flow is illustrated in figure 5.1.

5.1.6 Validation

For validation of the geometric accuracy of the derived time-resolved aortic geometry, 3 planes were placed at anatomical landmarks (see figure 5.2):

1. in the ascending aorta at the level of the lower edge of the pulmonary artery (AAo),
2. proximal to the first branch of the supra-aortic vessels (FB), and
3. at in the descending aorta (DAo) at the same height as plane 1.

As reference standard, the aortic lumen contours in all 3 planes were segmented manually for each time frame in the cardiac cycle. Area, mean velocity and flow were calculated

		PC-MRI
Voxel size:		
- Phase-encoding direction	[mm]	1.9-2.9
- Readout direction	[mm]	1.6-1.7
- Slab direction	[mm]	2-3.5
$FOV_{phase \times freq}$	[mm^2]	320-340 × 213-293
Matrix size		192 × 128-144
Temporal resolution	[ms]	39.2 - 48.8
TE/TR	[ms]	2.38-3.67/ 4.9-6.1
Bandwidth	[Hz/pixel]	440 - 480
Flip angle	[°]	7 or 15
v_{enc}	[cm/sec]	150-230

Table 5.1: *Pulse sequence parameters used for time-resolved 3D PC-MRI.*

for manual (reference standard), time-resolved and time-averaged (static) PC-MRA. Bland-Altman analysis was performed (table 5.2) and flow and area time-curves were plotted for each position (figures 5.6, 5.7).
Additionally, the distance between manually segmented vessel contour and automatic vessel contour segmentation was determined. Distance to the contour is a more sensible parameter as the area, since the area might not change much but moves strongly in the plane. When one considers the distance to the contour, it is more informative about how well the automatically determined contour follows the movement of the manually segmented.

5.2 Results

5.2.1 Validation

The time-resolved 3D PC-MR angiography in figure 5.2 shows good vessel depiction in peak systolic time frames (180-340 ms). During early systole (100 ms) and in diastole (420 ms), the vessel boundaries especially in the distal descending aorta are not completely depicted. Similar results were obtained for all other volunteers and patients. Further results for time-resolved 3D PCMRA are presented in figure 5.4. Different pathologies had no influence on the segmentation quality. However, in 10 of 11 patients the automatic removal of the pulmonary system was incomplete; in healthy subjects, the removal was incomplete for 3 of 11 data sets. Incomplete removal occurs if the pulmonal artery and aorta are very close (e.g. $\leq$ 1 voxel) to each other and show a similar flow direction, e.g. between pulmonary trunk and ascending aorta and between left pulmonary artery and descending aorta (see figure 5.4).

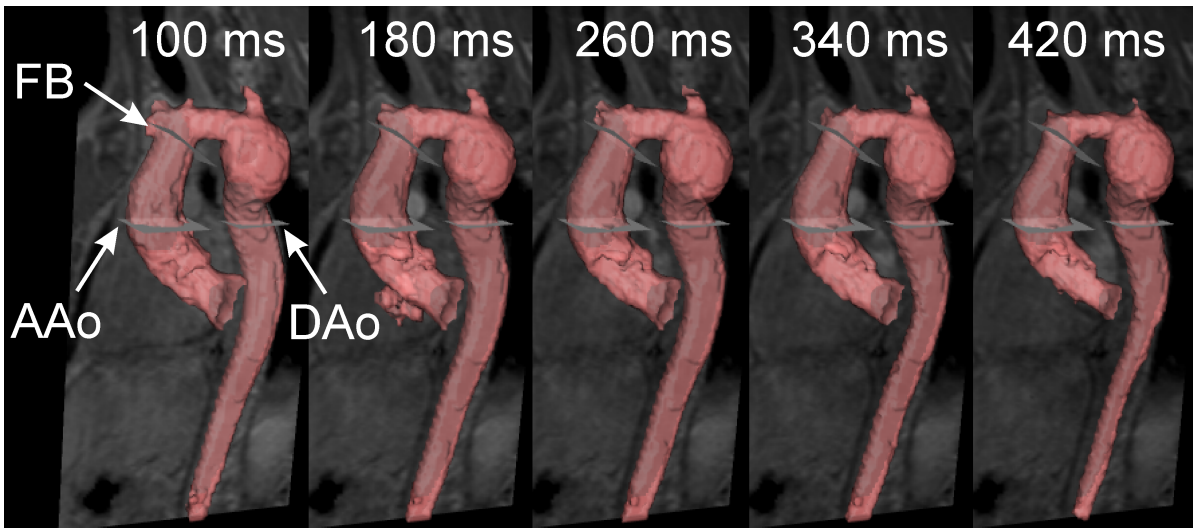

Figure 5.2: *Time-resolved 3D PCMRA in a patient with aneurysm in DAo, displayed at 5 time frames; white arrows indicate the position of the analysis planes: AAo - plane in the ascending aorta at the height of the lower edge of the pulmonary artery, FB - plane before first supra-aortic branch, DAo - plane in the descending aorta at the same height as in the ascending aorta.*

Figure 5.3 shows an example for the comparison between time-resolved and static PC-MRA and manually segmented vessel lumen contours (gold standard) for different time points in a plane through the ascending aorta. It is clearly visible that time-resolved segmentation follows the general motion and diameter changes of the aorta during

cardiac cycle better than the static segmentation.

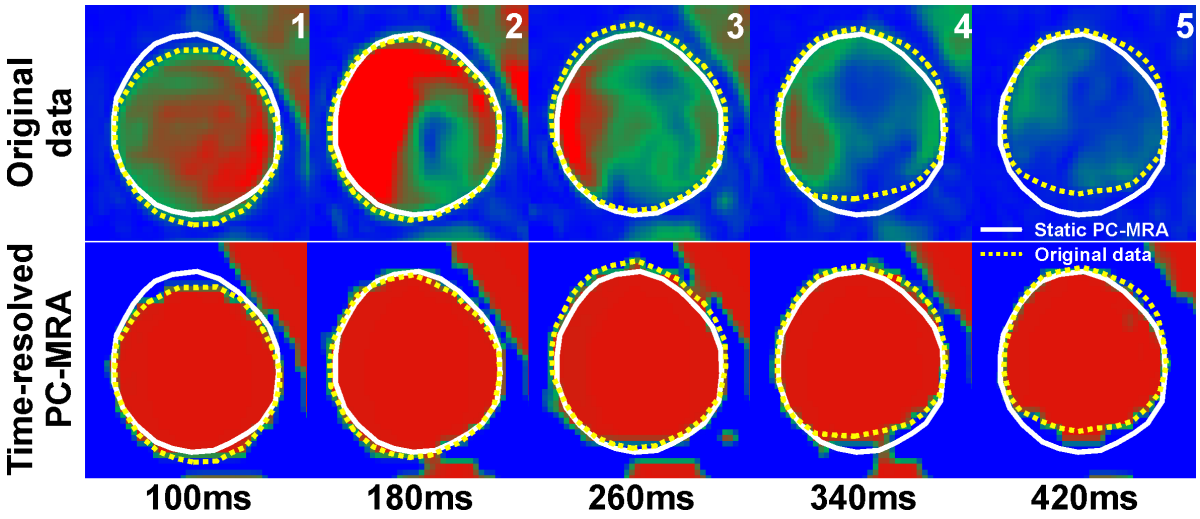

Figure 5.3: *A 2D analysis plane through the ascending aorta. Upper row color images: original data (magnitude weighted with velocity); bottom row color images: calculated time-resolved PCMRA; White solid contour: contour of static PC-MRA; yellow dashed contour: manual segmentation of original data.*

Bland-Altman analysis (table 5.2) revealed that time-resolved PC-MRA in most cases underestimated hemodynamic parameters compared to manual segmentation approach; but in some cases (AAo position in patients), time-resolved PC-MRA overestimated values probably due to the incomplete removal of pulmonary system and thus incorporating values from other vessels into the calculations. Bland-Altman plots for area are depicted in figure 5.5.

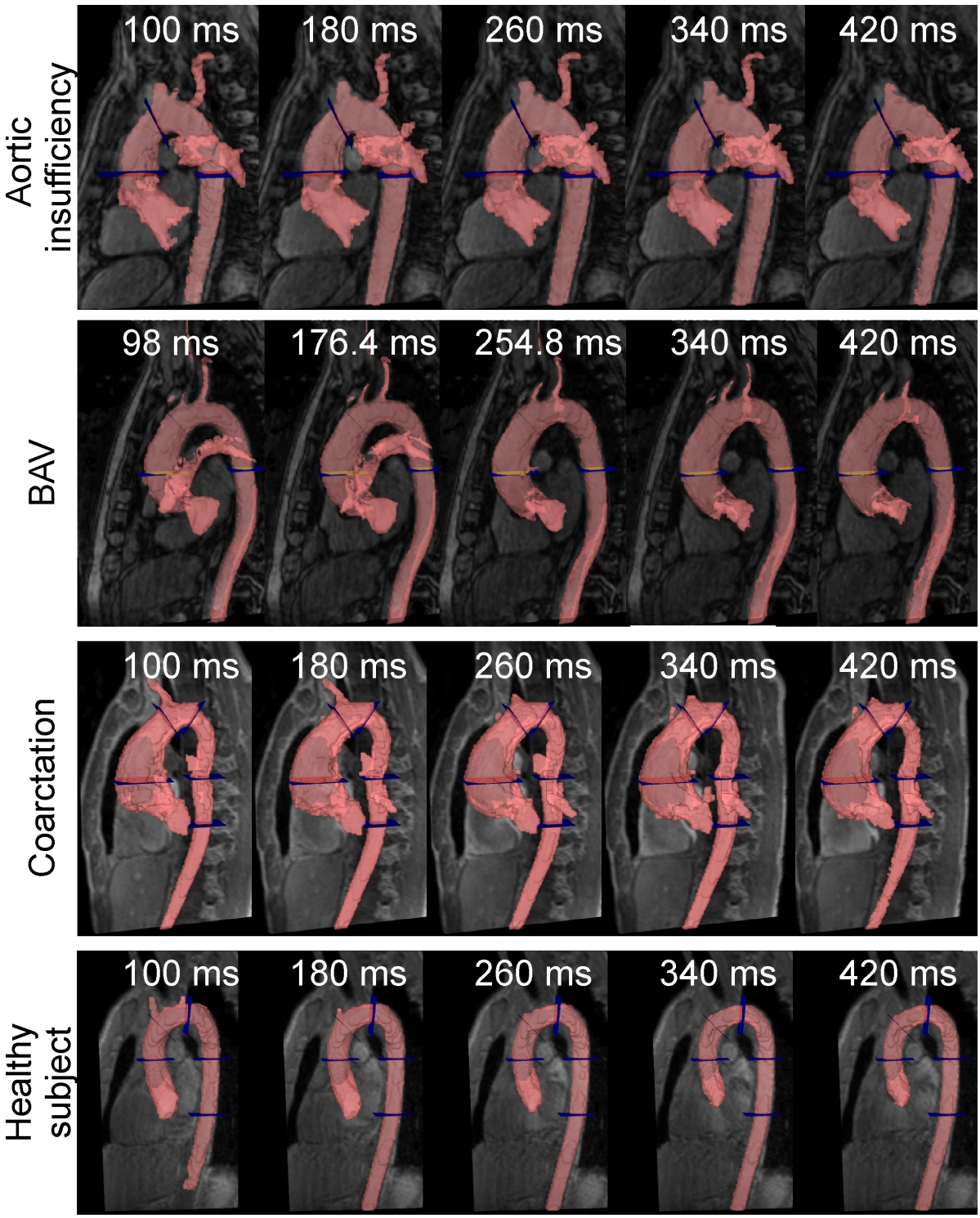

Figure 5.4: *Results for time-resolved 3D PCMRA demonstrated in three patients with different pathologies and in a healthy subjects displayed at 5 time frames.*

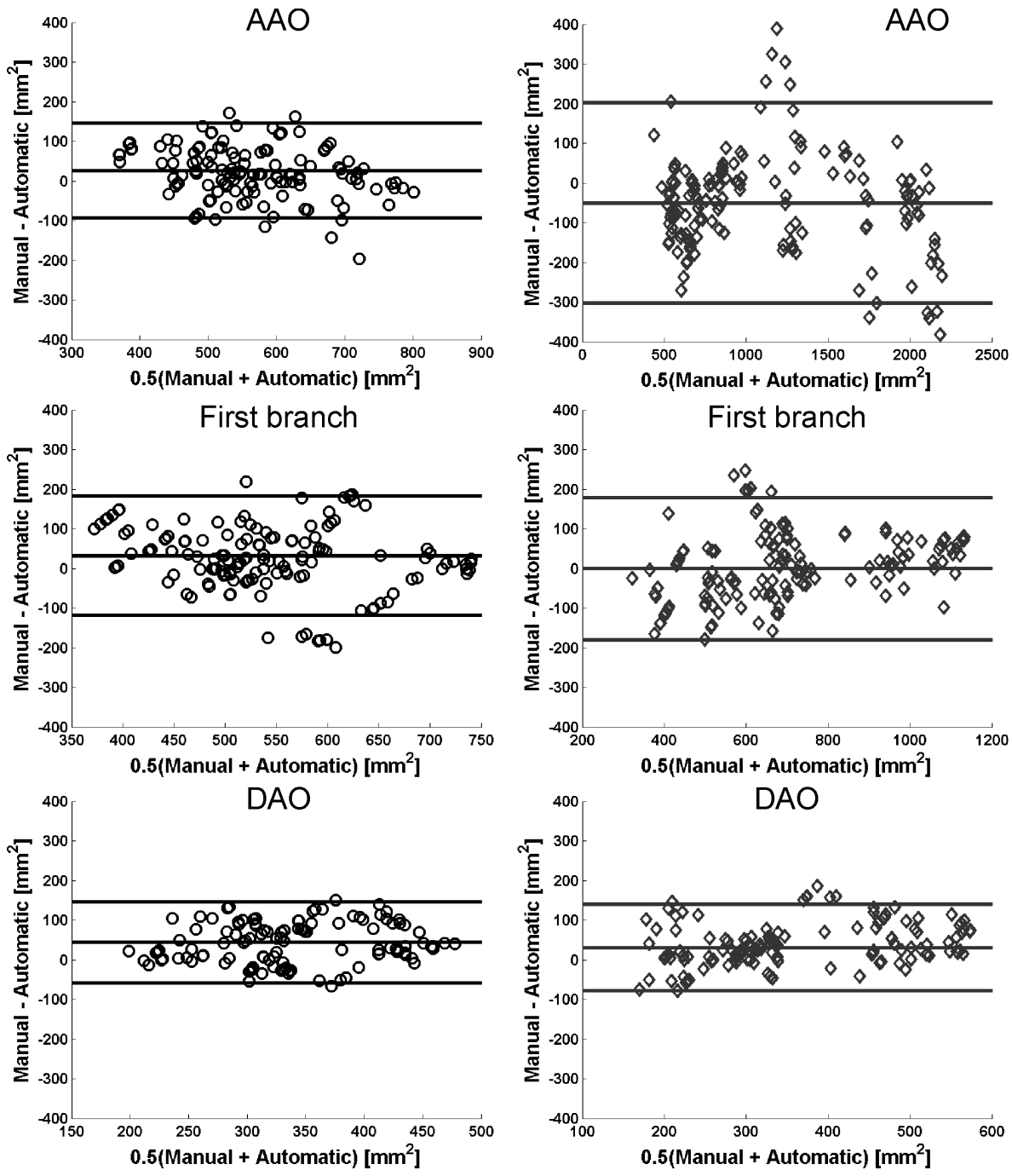

Figure 5.5: *Results from Bland-Altman-Analysis for area at 3 defined positions (AAo, First Branch and DAo) for healthy subjects (left) and patients (right).*

		Area [mm^2]	Mean Vel. [m/s]	Flow [ml/s]
		Mean Difference ± 1.96 Standard Deviation (minimum - maximum)		
AAo	Healthy subjects	25.8 ± 119.8 (337.0 - 819.4)	0.002 ± 0.053 (0.1 - 0.9)	5.5 ± 24.5 (19.3 - 629.5)
	Patients	-50.4 ± 252.2 (377.2 - 2374.5)	0.019 ± 0.067 (0.0 - 1.2)	2.7 ± 66.8 (15.5 - 1753.3)
FB	Healthy subjects	31.8 ± 150.5 (321.9 - 752.1)	-0.005 ± 0.056 (0.0 - 1.0)	5.3 ± 66.6 (15.1 - 669.6)
	Patients	-1.4 ± 179.1 (294.3 - 1171.9)	0.017 ± 0.081 (0.0 - 1.1)	9.8 ± 76.8 (13.9 - 1003.3)
DAo	Healthy subjects	43.6 ± 102.7 (184.1 - 497.9)	0.012 ± 0.065 (0.1 - 1.0)	7.9 ± 25.9 (14.6 - 390.6)
	Patients	30.1 ± 109.4 (127.3 - 615.4)	0.002 ± 0.074 (0.1 - 1.2)	7.6 ± 28.1 (8.9 - 440.0)

Table 5.2: *Results from Bland-Altman-Analysis for area, mean velocity and flow at 3 defined positions for healthy subjects and patients. Values are given as bias ± limits of agreement; in brackets minimum-maximum range of area, mean velocity and flow is given.*

The results for hemodynamic parameters derived with automatic and manual segmentations are shown in figures 5.6 and 5.7. Data are displayed as an average over subgroup with healthy subjects and over subgroup with patients for 18 consecutive time frames within the cardiac cycle. The deviation from the standard method (manual segmentation) was calculated as normalized root-mean-square deviation ($NRMSD$) for each subgroup:

$$NRMSD = \frac{1}{x_{max} - x_{min}} \cdot RMSD = \frac{1}{x_{max} - x_{min}} \cdot \sqrt{\frac{\sum_{i=1}^{N} (x_i - x_{ref,i})^2}{N}}, \tag{5.11}$$

where N is the number of time frames, $x_{ref,i}$ is the reference measurement (= manual segmentation), x_i is time-resolved or static segmentation and $[x_{max}, x_{min}]$ is the range of the observed values. The results for $NRMSD$ are provided in table 5.3 and show that time-resolved segmentation performs generally better than the static segmentation with the exception of the area in the descending aorta, which can be explained with a worse area representation in the diastole of the time-resolved segmentation.
The results for the comparison of manual determined vessel contour with automatic segmentation approaches are shown in figure 5.8. The data represent average distance to the vessel contour obtained with manual segmentation which provides the reference standard. Data are displayed for healthy subjects and patients for 23 consecutive time frames within the cardiac cycle. With the exception of some diastolic points in time at the first-branch position, the time-resolved segmentation shows smaller distance and

			Time-resolved PC-MRA	Static PC-MRA
AAo	Area	Healthy	0.240	0.371
		Patients	0.138	0.409
	Mean Velocity	Healthy	0.018	0.024
		Patients	0.053	0.045
	Flow	Healthy	0.024	0.042
		Patients	0.014	0.101
FB	Area	Healthy	0.283	0.367
		Patients	0.070	0.488
	Mean Velocity	Healthy	0.015	0.027
		Patients	0.044	0.038
	Flow	Healthy	0.026	0.051
		Patients	0.031	0.076
DAo	Area	Healthy	0.394	0.188
		Patients	0.353	0.475
	Mean Velocity	Healthy	0.028	0.046
		Patients	0.011	0.034
	Flow	Healthy	0.047	0.042
		Patients	0.044	0.040

Table 5.3: *Results for normalized root-mean-square deviation for area, flow and mean velocity. Values were calculated for each subgroup (healthy subjects and patients) at different positions in the aorta (ascending aorta, first branch and descending aorta) as illustrated in figure 5.2.*

thus better tracking of the manually segmented contour than the static segmentation. The distance for time-resolved contour to the manual segmented contour is in average under 2 voxels.

All segmentation was performed using Matlab (Mathworks, USA) on a Linux workstation (64 bit, 96GB RAM, 2x8 cores). Average computation times for all 22 subjects for each step are summarized in table 5.4. Main computation time is used for feature calculation.

	Computation time [s]
Bias correction	112 ± 13
Shading correction	104 ± 29
Features calculation	326 ± 57
Spatio-temporal FCM	138 ± 30
Post-processing	96 ± 14

Table 5.4: *Average computation times ± standard deviation for each performed step.*

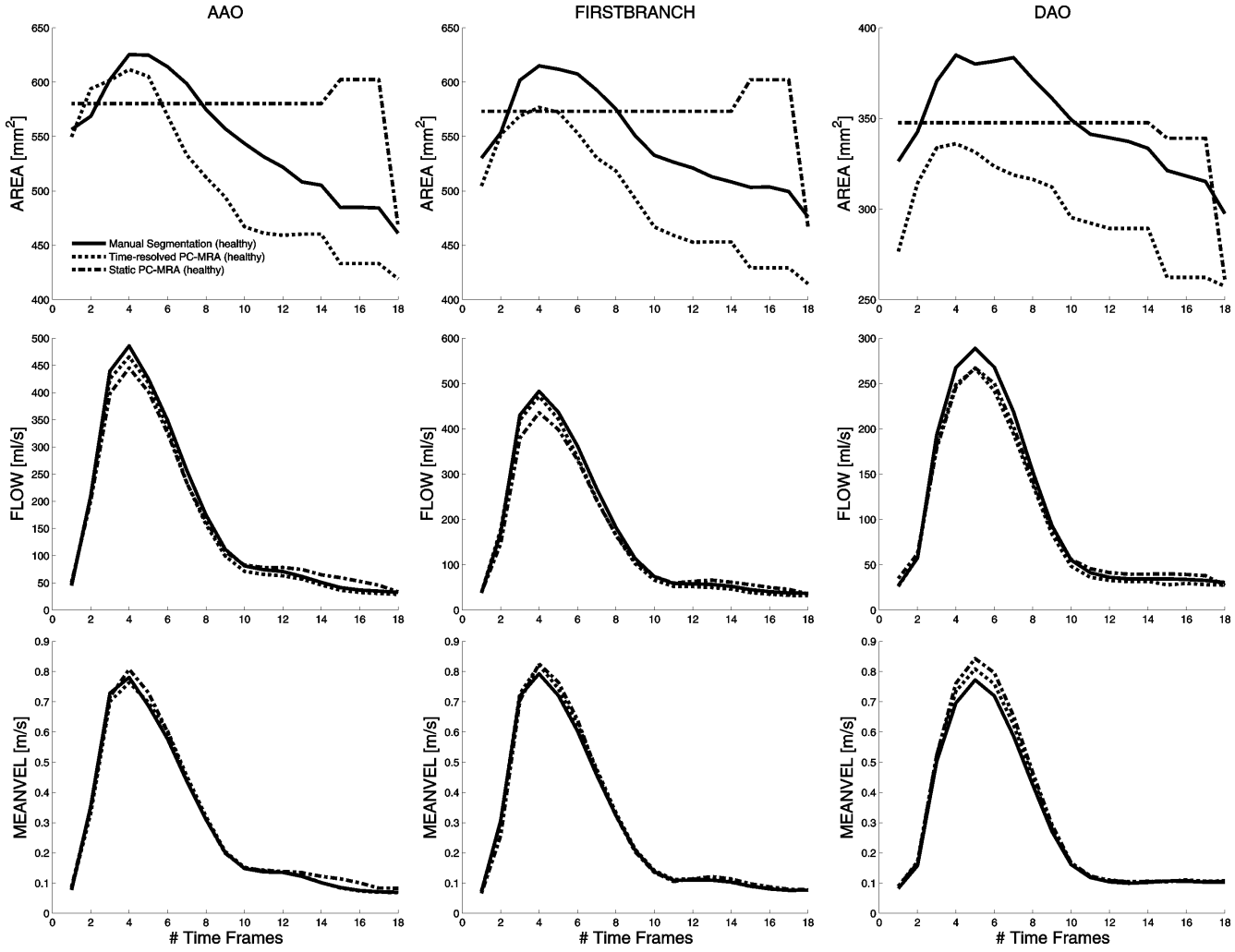

Figure 5.6: *Time-resolved curves averaged over healthy subjects for mean area (upper row), mean flow (middle row) and mean velocity (bottom row) at three positions (AAo, first branch, DAo as illustrated in figure 5.2). Solid lines represent manual segmentation; dotted lines - time-resolved and dashed lines - averaged 3D PC-MRA.*

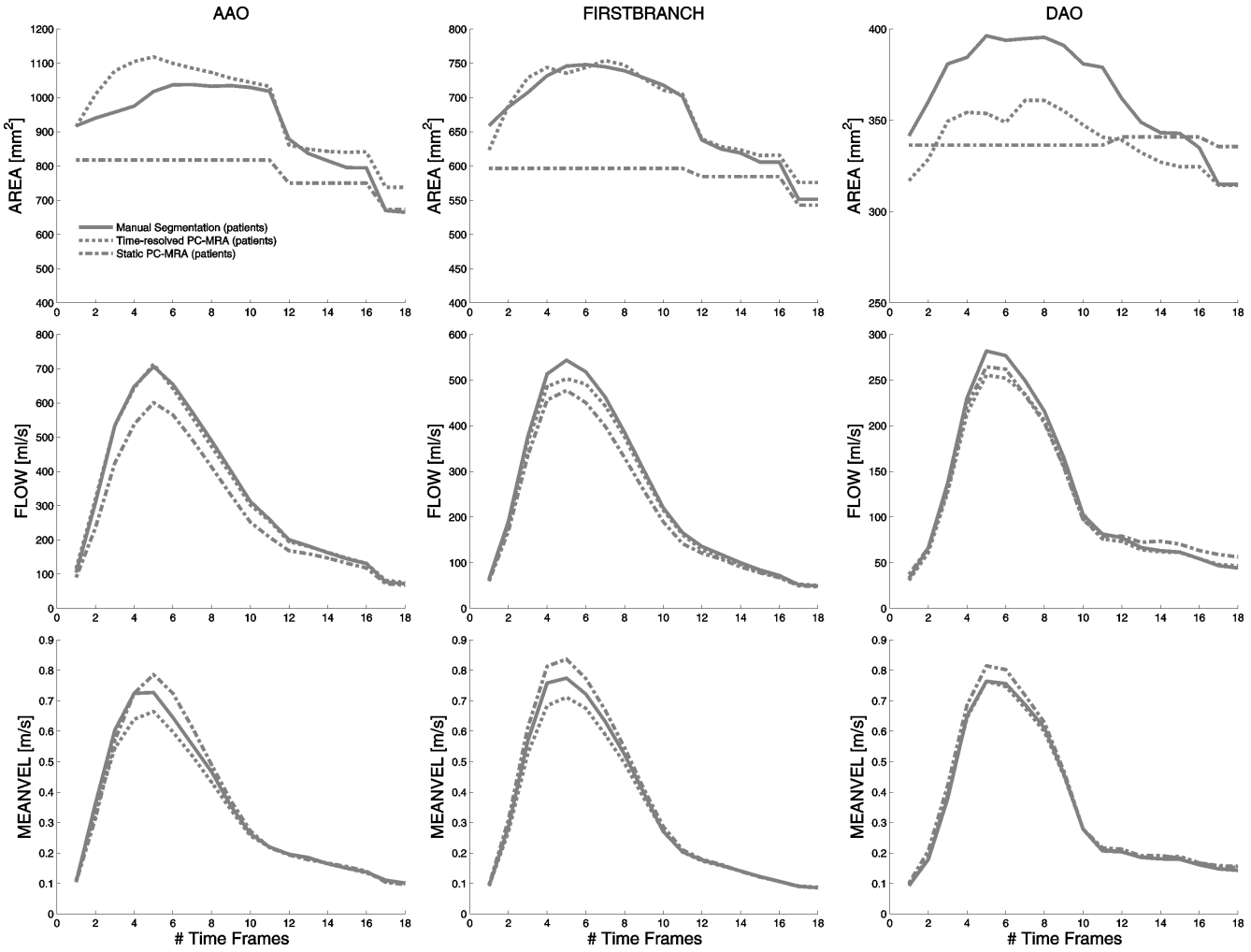

Figure 5.7: *Time-resolved curves averaged over all patients for mean area (upper row), mean flow (middle row) and mean velocity (bottom row) at three positions (AAo, first branch, DAo as illustrated in figure 5.2). Solid lines represent manual segmentation; dotted lines - time-resolved and dashed lines - averaged 3D PC-MRA.*

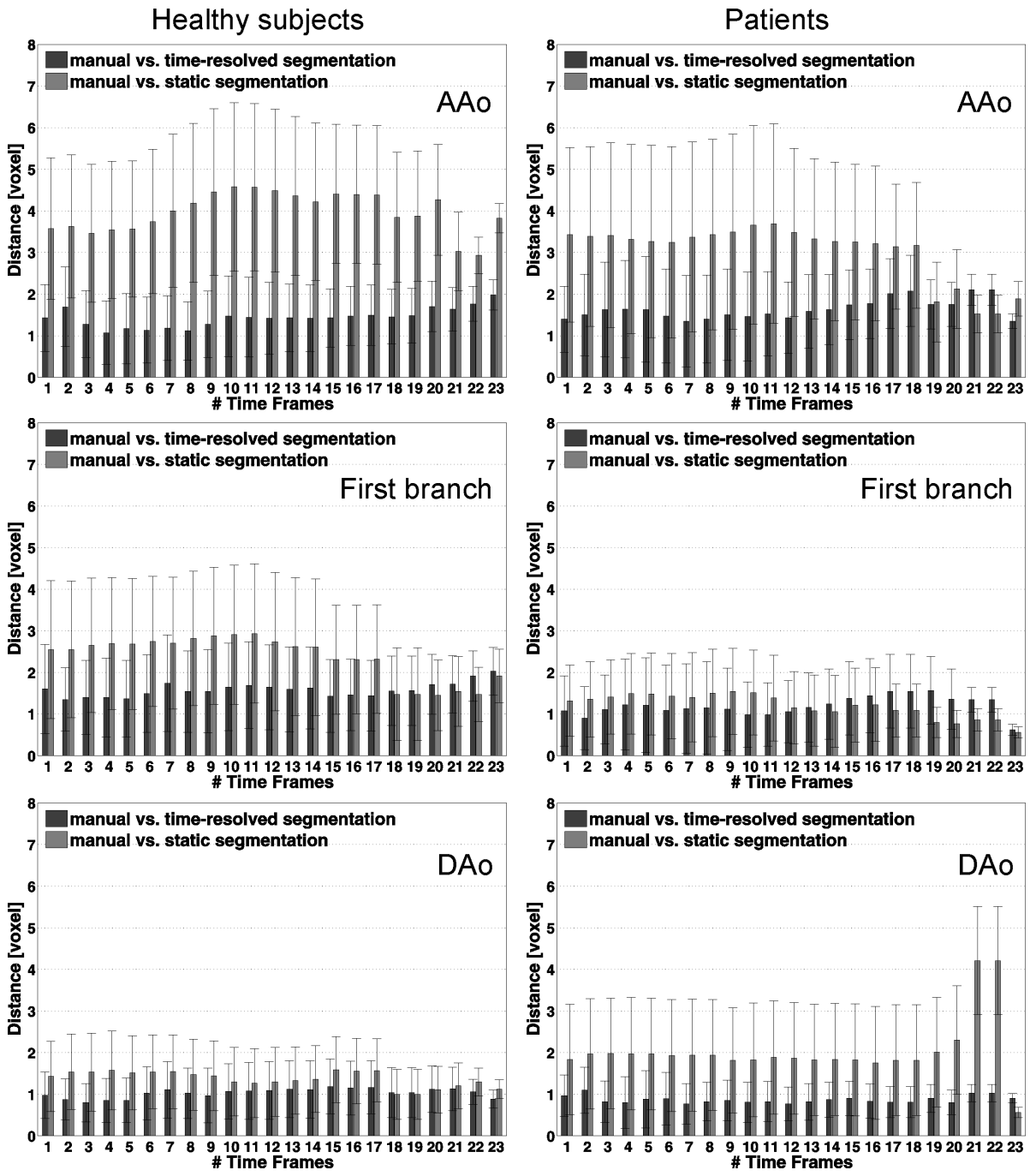

Figure 5.8: *Comparison of manual with automatic segmentation approaches shown. The data represent mean distance to the vessel contour obtained with manual segmentation. Black bars represent manual vs. time-resolved segmentation, gray bars - manual vs. static segmentation for 23 consecutive time frames within the cardiac cycle. The data were averaged over 11 healthy subjects (left plots) and 11 patients (right plots), standard deviations represent inter-subject variations. Data are provided for 3 plane positions (AAo, first branch, DAo as illustrated in figure 5.2).*

6 Applications using vessel boundaries

Once the vessel boundaries are determined using PC-MRA or cluster analysis, hemodynamic parameters can be derived using the velocity field inside these boundaries. Methods and results described below have been partially published in J. Bock et al.: *In vivo noninvasive 4D pressure difference mapping in the human aorta: Phantom comparison and application in healthy volunteers and patients*; in Magnetic Resonance in Medicine, 66:1079–1088, 2011.

6.1 Methods

In the following section, all the steps for the calculation of pressure gradients/differences are described.
In the presented work following experiments were performed:

1. *In vitro* experiments in a controlled environment using stenosis phantoms were performed to compare the pressure difference mapping technique with the established Bernoulli approach before a transfer to *in vivo* data.
2. Three *in vivo* pressure difference studies were performed:
   I. pressure differences using static 3D PC-MRA in healthy young and old control subjects in comparison to atherosclerosis patients, and
   II. a study with healthy subjects and patients with coarctation using static 3D PC-MRA for pressure calculations and pressure gradient values from echocardiography as standard reference, and
   III. a study in patients with coarctation using different modalities for gradient measurements (catheter, echocardiography and PC-MRI with static and time-resolved 3D PC-MRA).

6.1.1 Pressure difference calculation

Pressure gradients are an important clinical marker for the severity of cardiovascular disease such as aortic valve stenosis and aortic coarctation [13, 105]. In the clinical routine, catheter measurements are considered the gold standard to determine the pres-

sure gradients *in vivo*. Although this method is reported to be reliable and of low risk [106, 107], it remains an invasive procedure with its associated potential risk of severe side-effects and involves radiation exposure for catheter guidance [108].
Alternatively, in the clinical routine pressure gradient Δp can also be estimated using the simplified Bernoulli equation [109]:

$$\Delta p = 4\, v_{max}^2, \tag{6.1}$$

where v_{max} represents the peak velocity derived from clinical standard Doppler ultrasound. However, as described in section 2.2.2, measured v_{max} is operator dependent and subject to errors from poor acoustic windows and spectral broadening. Pressure gradient estimation is highly sensitive to velocity measurements errors of v_{max} due to the exponentiation of velocities in the Bernoulli equation (6.1). Furthermore, the simplified Bernoulli equation neglects important boundary conditions such as the velocity proximal to the stenosis and the shape of the stenosis as discussed by Oshinski et al. [110]. Although the immediate output of the Bernoulli equation is useful to obtain a value representing hemodynamic pressure drops in region of interest, it does not easily provide information regarding temporal and spatial variations across the stenosis.
As an alternative, it is possible to noninvasively and without user-dependency derive relative pressure gradients by using the time-resolved velocity field measured with time-resolved (CINE) three-directionally encoded phase contrast MRI. This approach is described in the following sections.

6.1.1.1 Separation of the aortic system

To estimate pressure differences *in vivo*, a reliable identification of the vessel lumen is required, so that neither noise nor static tissue are incorporated into the calculation. Additionally, it must be ensured that no connection between the aorta and the pulmonary system exists, because pulmonary system originates from low pressure system (right heart) and the aorta from high pressure system (left heart).
In *3D PC-MRA*, simple thresholding of the data was performed to create a three-dimensional binary mask. By using morphological operations such as thinning, the connectivity between the aorta and the pulmonary system can be broken. Next a flood filling algorithm, which determines the volume connected to a given voxel, was applied to generate a mask containing only voxels from the aorta.
In *4D PC-MRA*, in order to separate voxels containing veins and heart, the time course of each voxel is examined. If the peak velocities appear in the diastole, these voxels are set to zero. If the vena cava is still present, the user can manually set a seed voxel.

Starting from this point, all voxels which have similar flow direction and are connected in 3D to the starting voxel will be removed. This approach works reliably because the veins have opposite flow directions compared to the aorta.
The pulmonary artery and pulmonary trunk are more difficult to separate due to partial volume effects and relatively similar flow direction at various places (ascending aorta vs. pulmonary trunk and descending aorta vs. left pulmonary artery). The feature vector direction homogeneity VDH (see section 5.1.2) was used to separate pulmonary system from the aorta. VDH was calculated in a interrogation window containing 8 in-plane and 2 slice neighboring voxels. The mean value of the VDH over the systolic time points was calculated and a mask with all values greater or equal than 0.95 was created. The user manually selects two starting points: one in the right and one in the left pulmonary arteries. Starting from these points a pulmonary mask is created, containing all the voxels connected to the starting points in 3D. The created volume is used to mask out the pulmonary system for every time point.

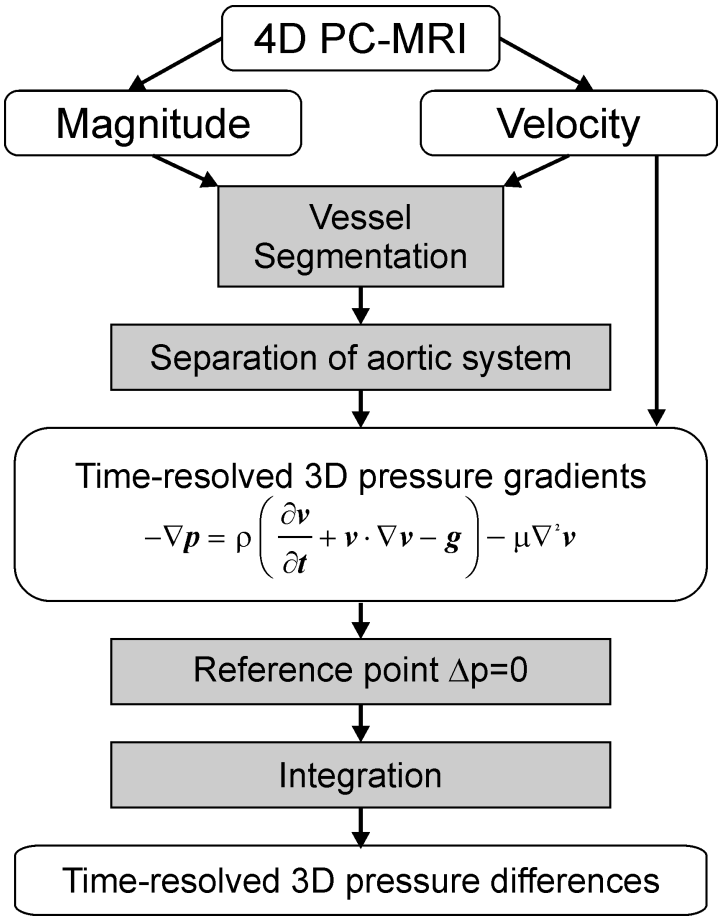

Figure 6.1: *Flow chart representing the necessary steps to calculate pressure difference maps for in-vivo data.*

6.1.1.2 Pressure gradients

For a viscous, incompressible fluid, pressure gradients can be calculated using the Navier-Stokes equation:

$$-\nabla p = \rho\left(\frac{\partial v}{\partial t} + v \cdot \nabla v - g\right) - \mu\nabla^2 v, \tag{6.2}$$

where p is the pressure gradient, μ is the dynamic fluid viscosity, v is the measured three-directional velocity, ρ is the fluid density, and g is the gravitational force. The terms on the right-hand side represent from left to right: the transient inertia, the convective inertia, gravitational force, and viscous resistance. As objects (phantom or human subjects) are placed in a horizontal position in the scanner, the gravitational force can be neglected for all calculations.

For a given voxel in the imaging volume, velocity values of the nearest temporal and spatial neighbors can be used for calculation of a central difference as an approximation for temporal ($\frac{\partial v}{\partial t}$), spatial first-order ($\nabla v$) and second-order ($\nabla^2 v$) velocity derivatives [10, 11, 108, 111, 112].

Pressure gradient can be calculated using equation (6.2) at all points within the imaging volume. Values used for density ρ and viscosity μ are summarized in table 6.1.

		in vitro	***in vivo***
Density ρ	[kg/m^3]	1105	1060
Viscosity μ	[Pa· s]	4.96x10^{-3}	3.2x10^{-3}

Table 6.1: *Density and viscosity values used to derive pressure gradients.*

6.1.1.3 Pressure difference

Based on derived pressure gradients, pressure differences $\Delta p\,(\vec{r}, t)$ were calculated by iteratively solving the Poisson pressure equation using a similar approach as described by Tyszka et al. [10]. Thereby the pressure is initialized by region growing integration of the pressure gradient ∇p with a user defined reference point ($\Delta p = 0$). Per iteration, the resulting $\Delta p^{'}\,(\vec{r})$ at each voxel position $\vec{r}$ was calculated as a weighted sum of the current $\Delta p\,(\vec{r})$ and the mean of the six possible pressures calculated from the neighboring voxels [10]:

$$p^{'}\,(\vec{r}) = (1-\alpha)\,p\,(\vec{r}) + \frac{1}{6}\alpha\left(\sum_n p_n(\vec{r}) + \nabla p_n \cdot \Delta r_n\right),$$

where n indicates one of the six orthogonal neighbors, ∇p_n is the pressure gradient at the n^{th} neighbor and Δr_n is the vector displacement from the current voxel to the n^{th} neighbor. The value of α was set to 0.5 for all calculations. This recurrence relation

was repeated until convergence, where relative change in the mean pressure in the entire volume of less than 0.1% between two successive iterations was set as convergence criterion. As data represent a real incompressible fluid, the assumption was made that the flow obeys the divergence-free condition (e.g. is incompressible) but this condition was not explicitly enforced [10].
All calculations were performed independently for each time frame. Unlike simplified Bernoulli, the latter described approach apparently offers the advantage to estimate temporally and spatially distributed pressure gradients within a vessel segment.

6.1.2 In vitro experiments and validation of pressure mapping

Measurement parameters

In vitro measurements were performed using time-resolved three directionally encoded PC-MRI on a 3 T MR-System.
A stenosis model (pipe ⌀ 26.8 ± 2.0 mm, stenosis ⌀ 17.1 ± 0.1 mm) was connected to a pneumatically driven ventricular assist device (Medos Medizintechnik AG) used as pump for the generation of pulsatile flow (pump cycle = 60 ms, flow rate = 66 mL/cycle, prestenotic systolic peak velocity = 0.7 m/s). Figure 6.2 shows the schematic setup of the *in vitro* experiment. Blood-mimicking fluid (60% water, 40% glycerol) was used as blood substitute. Measurements were synchronized with the pulsatile flow cycle. Acquisition parameters are summarized in table 6.2. The measurement was repeated once with identical parameters but with flow off. This measurement was subtracted for correction of eddy currents and Maxwell terms [62].

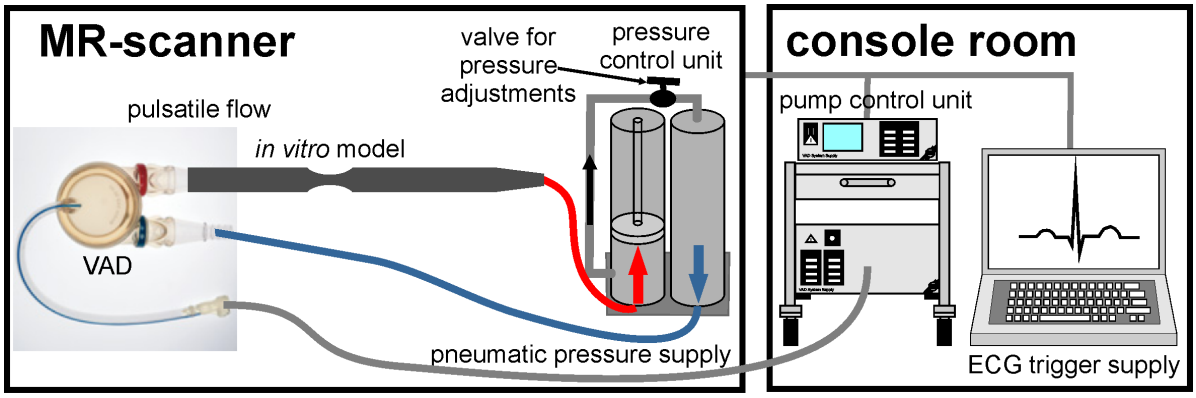

Figure 6.2: *Setup of the pneumatically driven ventricular assist device pump system in the MR-scanner (left) and the console room (right). The in vitro stenosis model was integrated into a closed flow circuit.* Image adapted from [113].

		in vitro
Voxel size:		
- Phase-encoding direction	[mm]	1.4
- Readout direction	[mm]	1.2
- Slab direction	[mm]	1.2
$FOV_{phase \times freq}$	[mm^2]	284 × 350
Matrix size		234 × 288
Temporal resolution	[ms]	42.4
TR	[ms]	5.3
TE	[ms]	2.7
Bandwidth	[Hz/pixel]	457
Flip angle	[°]	15
v_{enc}	[cm/sec]	150

Table 6.2: *Pulse sequence parameters used for in vitro measurements.*

Data analysis

3D pressure difference maps were calculated for each of 22 acquired time-frames using Navier-Stokes modeling (equation (6.2)). The reference point ($\Delta p = 0$) was set directly in the stenosis at the site of the minimal diameter. In addition, analysis planes located proximal and distal to the phantom stenosis (see figure 6.3) were used to extract maximum velocities measured with MRI. These were used to determine time-resolved pressure differences (PD), according to the simplified (6.1) and modified (6.3) Bernoulli equations:

$$\Delta p = \frac{1}{2}\rho \left(v_2^2 - v_1^2 \right), \tag{6.3}$$

where v_1 and v_2 are velocities at locations proximal and distal of the stenosis.
Calculated PD dynamics was compared with results from Navier Stokes modeling.

6.1.3 In vivo studies

6.1.3.1 In vivo study I

Measurement parameters

12 healthy young subjects (mean age 24.5 years), 5 healthy elder subjects (mean age 61.2 years) and 6 patients with severe aortic atherosclerosis (aortic plaques > 4 mm as demonstrated by trans-esophageal echocardiography (TEE), mean age = 73.7 years) were included in our study after approval by the local ethic committee and written informed consent. All measurements were performed on a 3T system (Magnetom TRIO, Siemens, Germany) using an ECG gated and respiration controlled rf-spoiled gradient echo sequence. Flow sensitive 4D MRI data were acquired covering the entire thoracic aorta. Measurements parameters are summarized in table 6.3.

		***in vivo* I**
Voxel size:		
- Phase-encoding direction	[mm]	2.0 - 3.2
- Readout direction	[mm]	1.7 - 2.7
- Slab direction	[mm]	2.2 - 3.0
$FOV_{phase \times freq}$	[mm^2]	240-306 × 320-350
Matrix size		96-168 × 128-192
Temporal resolution	[ms]	38.4 - 40.8
TR	[ms]	4.8 - 5.1
TE	[ms]	2.4 - 2.5
Flip angle	[°]	7
v_{enc}	[cm/sec]	150

Table 6.3: *Pulse sequence parameters used for atherosclerosis in vivo study.*

Data analysis

For each *in vivo* data set, time-averaged PC-MRA using equation (4.1) with additional noise masking and static tissue removal was calculated and the pulmonary system was separated from the aorta as described in 6.1.1.1. All calculations regarding pressure gradients and differences were then restricted to the calculated aortic lumen.

In order to compare the data between subjects, a reference point (pressure difference Δp =0) was set manually in the ascending aorta at the level of the lower edge of the pulmonary artery.

For quantitative inter-subject analysis, 5 analysis planes were manually positioned at different anatomical landmarks as shown in figure 6.5. Difference between two adjacent planes were calculated. The resulting pressure difference - time curves were temporally interpolated to 1ms. Next, comparisons (unpaired t-test, p-value < 0.05 was considered statistically significant) of systolic and diastolic peak pressure differences as well as time to peak pressure values between healthy subjects and patients were performed for all 4 curves.

6.1.3.2 In vivo study II

Measurement parameters

Twelve healthy subjects (mean age 24.5 ± 3.2 years, four female) and six patients after aortic coarctation repair (mean age 23.5 ± 7.3 years, two female) were included in our study after approval by the local ethics committee and written informed consent.

Patients were characterized by having undergone surgery for coarctation of the aorta at the age of 9 ± 6.9 years (range 0.04-14.2 years). MR measurements in patients were performed 15.1 ± 6.3 (range 6.3-23.7) years after the intervention. Four patients presented a re-stenosis. Five patients developed post-stenotic dilatation.

All measurements were performed on a 3 T system (Magnetom Trio, Siemens AG) with a standard eight-channel phased-array coil. Patients received contrast agent (Gadobenate dimeglumine) for contrast enhanced MR angiography of the aorta.
Flow sensitive 4D PC-MRI data with three directional velocity encoding and covering the entire thoracic aorta were acquired using a navigator respiration controlled and ECG-gated RF-spoiled gradient echo sequence. Imaging parameters can be found in table 6.4. Flip angles were independently adjusted for subgroups with and without contrast agents (α =15° and α =7°, respectively) to optimize image contrast. Data were acquired in a sagittal oblique 3D volume. The total scan time for the flow-sensitive measurement was 17.8 ± 4.9 min (heart rate dependent range 9.5-30 min).

		***in vivo* II**
Voxel size:		
- Phase-encoding direction	[mm]	1.9-2.4
- Readout direction	[mm]	1.7-1.8
- Slab direction	[mm]	2.0-2.5
$FOV_{phase \times freq}$	[mm^2]	213-255 × 320-340
Matrix size		128-144 × 192
Temporal resolution	[ms]	39.2-40.8
TR	[ms]	4.9-5.2
TE	[ms]	2.48-2.53
Bandwidth	[Hz/pixel]	440
Flip angle	[°]	7 or 15
v_{enc}	[cm/sec]	150-230

Table 6.4: *Pulse sequence parameters used for in vivo II measurements.*

Echocardiography

Prior to MRI, patients underwent echocardiography per clinical standard procedure on a Vivid 7 system (General Electrics Vingmed Ultrasound) equipped with a 2.5 - 5 MHz phased-array transducer. Cine loops of three consecutive heart cycles were digitally stored for off-line analysis. Scans included measurements of velocities at the site of coarctation and/or repair in the most appropriate view. Doppler values were recorded as maximum and mean velocity. Pressure gradients at the site of the aortic coarctation were derived from Doppler ultrasound using peak velocities and the simplified Bernoulli equation (6.1) for all six patients. During echocardiography the peak velocities were recoded by the operator but the full velocity-time curves were not available for retrospective analysis.

Data analysis

For vascular lumen segmentation a processing chain was used as described above in section 6.1.3.1. The segmented lumen was used in conjunction with the 4D velocity data for automated estimation of pressure differences based on the Navier-Stokes equation. In order to compare the data between subjects, a reference point (Δp=0 mmHg) was set manually in the ascending aorta at the level of the lower edge of the pulmonary artery.

4D pressure maps

For the 3D visualization of the resulting aortic geometry and the calculated pressure difference maps, data were loaded into a commercial software package (EnSight). The software could be used to manually position 2D analysis planes at any desired location in the 3D data volume. Pressure difference data in these analysis planes was exported and further analyzed.

Quantitative analysis

For quantitative inter-subject comparison of the *in vivo* data, five analysis planes were positioned at the anatomical land marks as shown in figure 6.7: 1. directly above the reference point in the ascending aorta (AAo), 2. proximal to the first aortic branch, 3. distal to the last aortic branch, 4. at the level of reference point in the descending aorta (DAo I), and 5. five cm further downstream in the DAo (Dao II). Additionally, the results from our study were compared to literature values [10, 11, 114]. For all analysis planes, the temporal evolution of the pressure differences averaged over the aortic lumen was calculated.

Comparison of systolic and diastolic peak pressure differences as well as time to peak values between healthy subjects and patients were performed for two anatomical positions (Last branch and DAo II as depicted in figure 6.7). Therefore temporal interpolation of the pressure differences from original time resolution to 1 ms was performed.

For comparison of peak and time-to-peak values between healthy subjects and patients an unpaired t-test was performed using interpolated data.

Coarctation quantification

In data from patients, two additional analysis planes proximal and distal to the aortic coarctation were used for analysis of the pressure differences across the aortic narrowing (see figure 6.8). For all data, mean pressure differences relative to the reference point were calculated in each plane for all time frames. The time-resolved pressure gradient between two analysis planes was determined by calculating the difference of mean values

from proximal and distal planes. Additionally the maximum value of the pressure gradient was determined from all possible paths between the two analysis planes [115]. The calculated pressure gradients across the coarctation were compared to findings from Doppler ultrasound and to MR based pressure differences using the simplified Bernoulli method.

Correlation with Doppler echocardiography
The correlation of pressure gradients calculated from MRI versus Doppler US was analyzed using linear regression analysis. Slope and intercept of linear regression were calculated. The overall quality of the regression was assessed using Pearson's correlation coefficient r; a correlation was considered significant for $p < 0.05$ [116].

6.1.3.3 In-vivo study III

Measurement parameters
Five patients (mean age 11.4 years, 1 female) with aortic coarctation were included in our study after approval by the local ethic committee and written informed consent. All measurements were performed on a 1.5 (Avanto, Siemens, Germany) or 3T system (Magnetom TRIO, Siemens, Germany) using an ECG gated and respiration controlled rf-spoiled gradient echo sequence. Measurements on the 1.5 T system were performed with contrast agent application (Prohance). Flow sensitive 4D MRI data were acquired covering the entire thoracic aorta. MRI measurement parameters are summarized in table 6.5.
Additionally, all patients were examined by echocardiography and cardiac catheterization 5.6 ± 8.3 months after the MR study as a part of the regular clinical examination. In echocardiography, mean and maximal pressure gradients over the coarctation were measured. During catheterization pressure gradients were determined between ascending and descending aorta, first, under no special condition, and secondly during medicamentous stress testing with Dobutamine.

Data analysis
Vascular lumen segmentation was performed using clustering analysis as described in section 5, resulting in a time-resolved 3D segmentation of the aorta. Additionally, static 3D lumen segmentation was performed as described in section 6.1.3.1. Pressure differences were calculated based on the Navier-Stokes equation using 4D velocity data in conjunction with the segmented 3D and 4D aortic lumen. A reference point (Δp=0 mmHg) was set manually in the ascending aorta at the level of the lower edge of the

		***in vivo* III**
Voxel size:		
- Phase-encoding direction	[mm]	2.0 - 2.25
- Readout direction	[mm]	1.75 - 1.88
- Slab direction	[mm]	2.0 - 2.8
$\text{FOV}_{phase \times freq}$	[mm^2]	213-293 × 320-340
Matrix size		128-176 × 192
Temporal resolution	[ms]	38.4 - 40.0
TR	[ms]	4.8 - 5.0
TE	[ms]	2.3 - 2.5
Flip angle	[°]	7-15
v_{enc}	[cm/sec]	150-300

Table 6.5: *MRI measurement parameters for in vivo study III*

pulmonary artery. For further analysis data were exported into a visualization software (EnSight). For comparison of pressure calculated from PC-MRI data with pressure catheter examination, 2 analysis planes were positioned at the locations where pressure gradient is measured using catheter: one in the ascending aorta (in the middle between aortic valve and first supra-aortic branch) and the second one - distal to the coarctation. Mean and maximal pressure difference between those planes was calculated.

6.2 Results

6.2.1 Pressure gradients

6.2.1.1 In vitro measurements and validation of PD mapping

Figure 6.3 illustrates pressure differences distribution along the stenosis model for three selected time frames of the pulsatile flow cycle. In this pulsatile flow measurement, one can observe both the influence of the transient and convective acceleration terms in the Navier-Stokes pressure modeling. As for the steady-flow condition, convective acceleration (spatially changing velocities) results in a pressure gradient across the stenosis. Transient acceleration (temporally changing velocities) resulted in a pressure inversion during diastole (time 445.2 ms) compared with the situation in systole. This pressure inversion is associated with deceleration of blood flow in diastole as well as with the pressure pulse wave reflection at the periphery [117, 118].

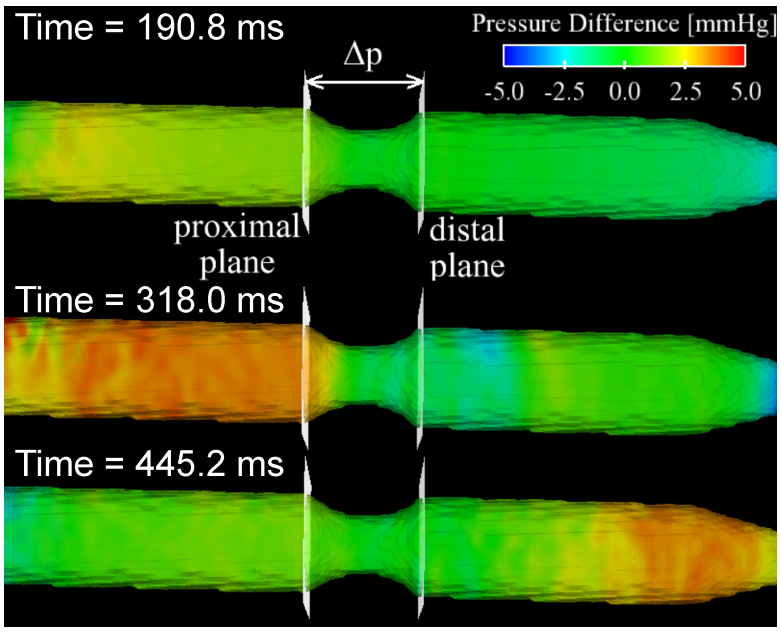

Figure 6.3: *Pressure difference distribution along the stenosis model using pulsatile flow. Images capture three selected time frames of the flow cycle. Pressure inversion during diastole (time point 445.2 ms) can clearly be appreciated.*

The dynamics changes of PDs between the two analysis planes in figure 6.3 during one flow cycle are shown in figure 6.4. Time-resolved PDs across the stenosis show good agreement between Navier Stokes modeling and the reference methods (Bernoulli). Linear regression analysis results are presented in table 6.6.

modified Bernoulli vs. Navier-Stokes	**simplified Bernoulli vs. Navier-Stokes**
y = 1.17x + 0.40	y = 0.85x + 0.25
$r = 0.95$	$r = 0.97$
$p < 0.05$	$p < 0.05$

Table 6.6: *Linear regression analysis results for modified and simplified Bernoulli vs. Navier-Stokes modeling.*

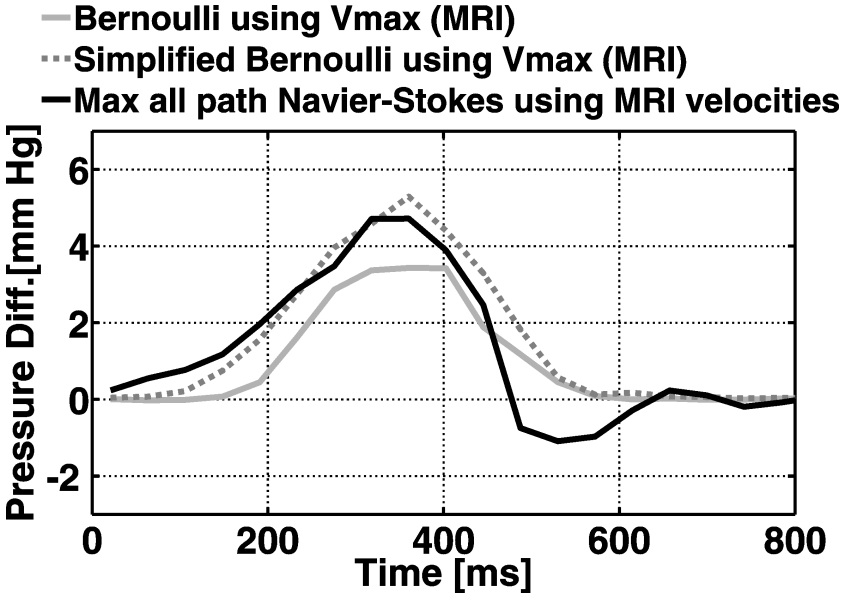

Figure 6.4: *The curves represent time resolved pressure gradient over the stenosis model. Maximum velocity measured in MRI was used to calculate pressure differences with modified Bernoulli (gray solid line) and simplified Bernoulli (gray dotted line) equations. The black line represents pressure differences calculated as maximum over all paths using the Navier-Stokes equation.*

6.2.1.2 In vivo study I

The resulting pressure waveforms in young and elder volunteers and in patients which were extracted from the 4D pressure mapping data are shown in figure 6.5. Black curves show the mean pressure differences averaged over 12 volunteers for all 4 aortic segments. Dark gray curves represent the mean pressure differences averaged over 5 healthy elder subjects and light gray lines show results averaged over 6 patients with aortic atherosclerosis.

Similar peak pressure differences in healthy and diseased subjects can be observed in segments 1 and 2. Decreased peak pressure differences are present in segments 3-4 in elder subjects and patients. Elder subjects and patients with atherosclerosis show a trend towards an earlier inversion of the pressure wave in segments 2-4.

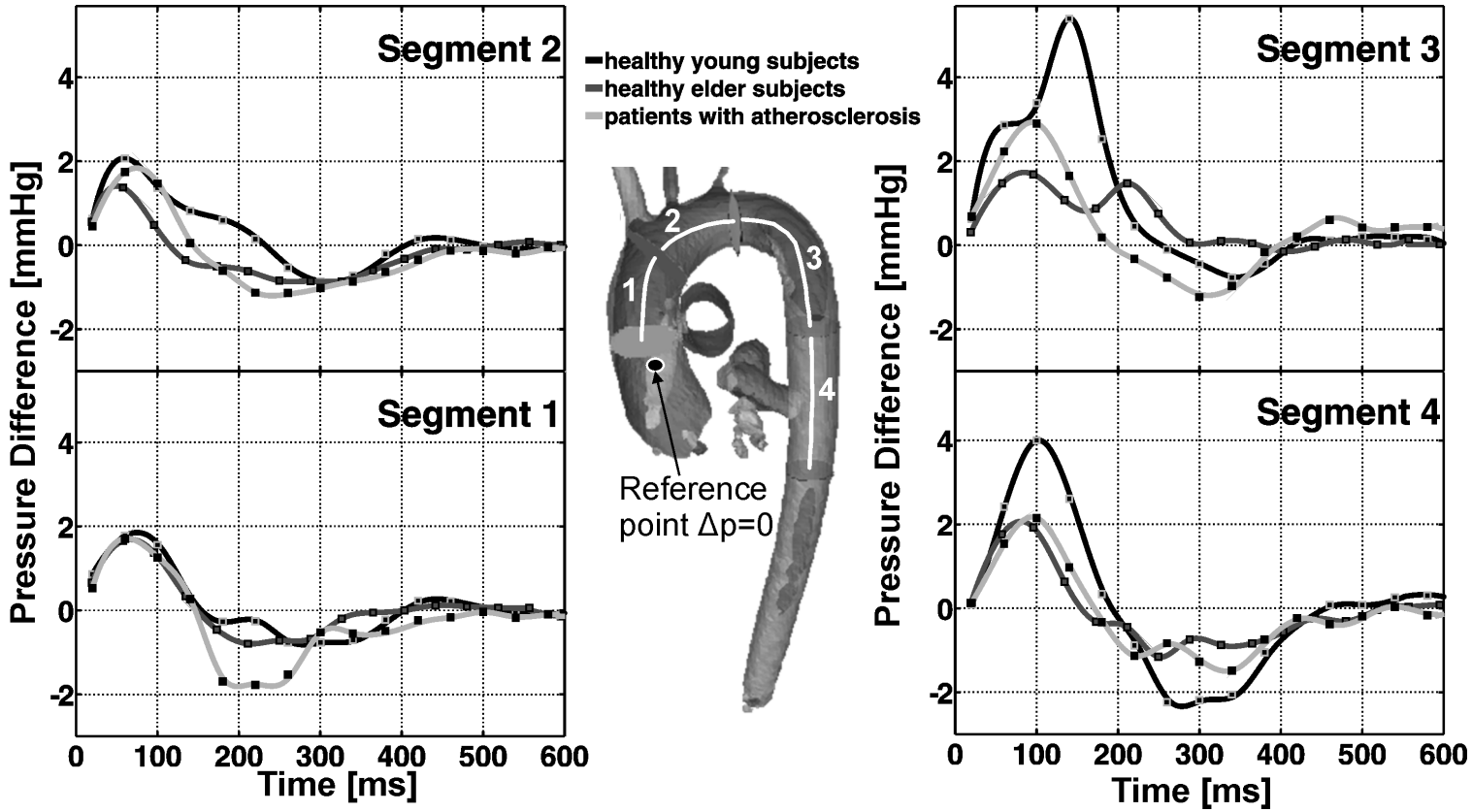

Figure 6.5: *Time-resolved mean pressure differences in 4 segments (difference between adjacent planes interpolated to 1 ms; black line: averaged over 12 healthy young subjects; dark gray line: averaged over 5 healthy elder subjects; light gray line: averaged over 6 patients with aortic atherosclerosis.*

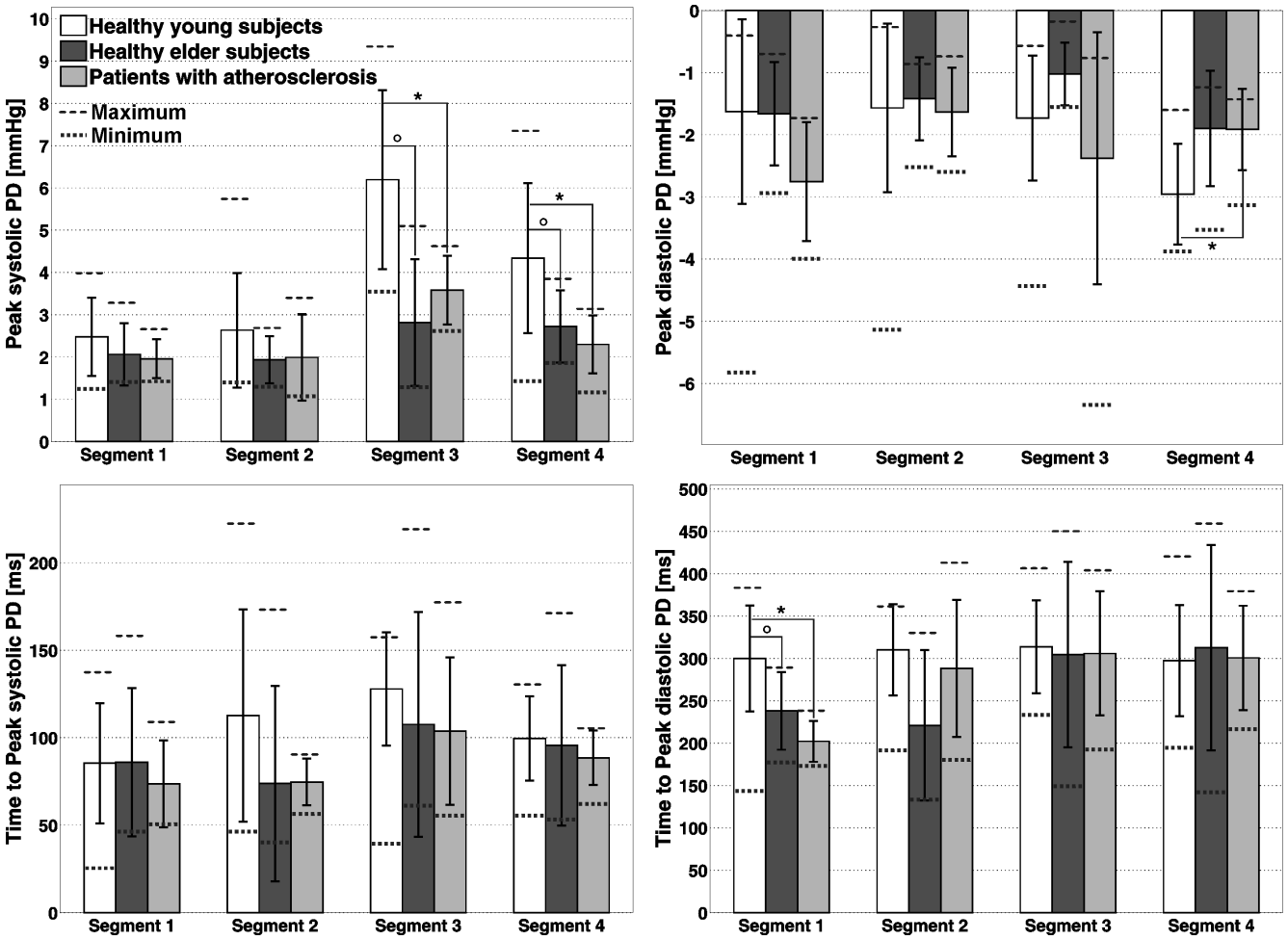

Figure 6.6: *Peak pressure differences and time-to-peak in systole and diastole for each subgroup in 4 segments. Values are shown as mean and with inter-individual standard deviation; range is given as maximum (dark grey dotted line) and minimum (black dotted line); significant results ($p<0.05$) from the unpaired t-test are marked with * for healthy young vs. atherosclerosis patients; and with ∘ for significant differences between young and old healthy subjects; no significant differences have been found between old healthy subjects and patients with atherosclerosis.*

Figure 6.6 shows results for systolic and diastolic peak pressure differences and time-to-peak for each subgroups in four segments. Unpaired t-test revealed significant differences ($p < 0.05$) for peak systolic values in segments 3 and 4 for healthy young subjects vs. atherosclerosis patients as well as between young and old healthy subjects. Significant differences in diastolic pressure differences were found between healthy young subjects and atherosclerosis patients in segment 4. Time-to-peak diastolic PD shows significant difference in segment 1 for healthy young subjects vs. atherosclerosis patients as well as between young and old healthy subjects. No significant differences have been found between old healthy subjects and patients with atherosclerosis.

6.2.1.3 In vivo study II

The cumulative results for all 12 normal subjects and 6 patients are summarized in figure 6.7. The graphs represent pressure differences averaged over all 12 volunteers and 6 patients for 5 analysis planes. High systolic pressure differences as well as the expected inverted pressure differences during early diastole [10] can be appreciated. The small standard deviations for healthy subjects indicate high data consistency.
In patients, pressure difference - time curves were of similar shape but demonstrated higher peak pressure differences and delayed times-to-peak. The descriptive statistics of peak and time-to-peak pressure gradients for volunteers and patients is summarized in table 6.7. Comparison of peak and time-to-peak values between healthy subjects and patients using unpaired t-test revealed no statistically significant differences for peak diastolic and time to peak systolic pressure differences at the "Last Branch" location (see figure 6.7). All other values showed statistically significantly increased peak and time-to-peak pressure differences in coarctation patients compared to healthy controls.
In patients, peak pressure gradients across the aortic coarctation (figure 6.8) were compared between the reference standard echocardiography and MRI findings at the same location (figure 6.9). The example in figure 6.8 illustrates that simplified Bernoulli calculations (top right, orange curve) resulted in a different temporal evolution of maximum pressure difference across the coarctation compared to Navier Stokes modeling (top right, white curve). Navier stokes provided improved peak pressure estimation and was similar to echocardiography and could show diastolic pressure inversion across the stenosis which could not be reproduced with the simplified assumptions of the Bernoulli approach. Quantitative results are summarized in table 6.9.

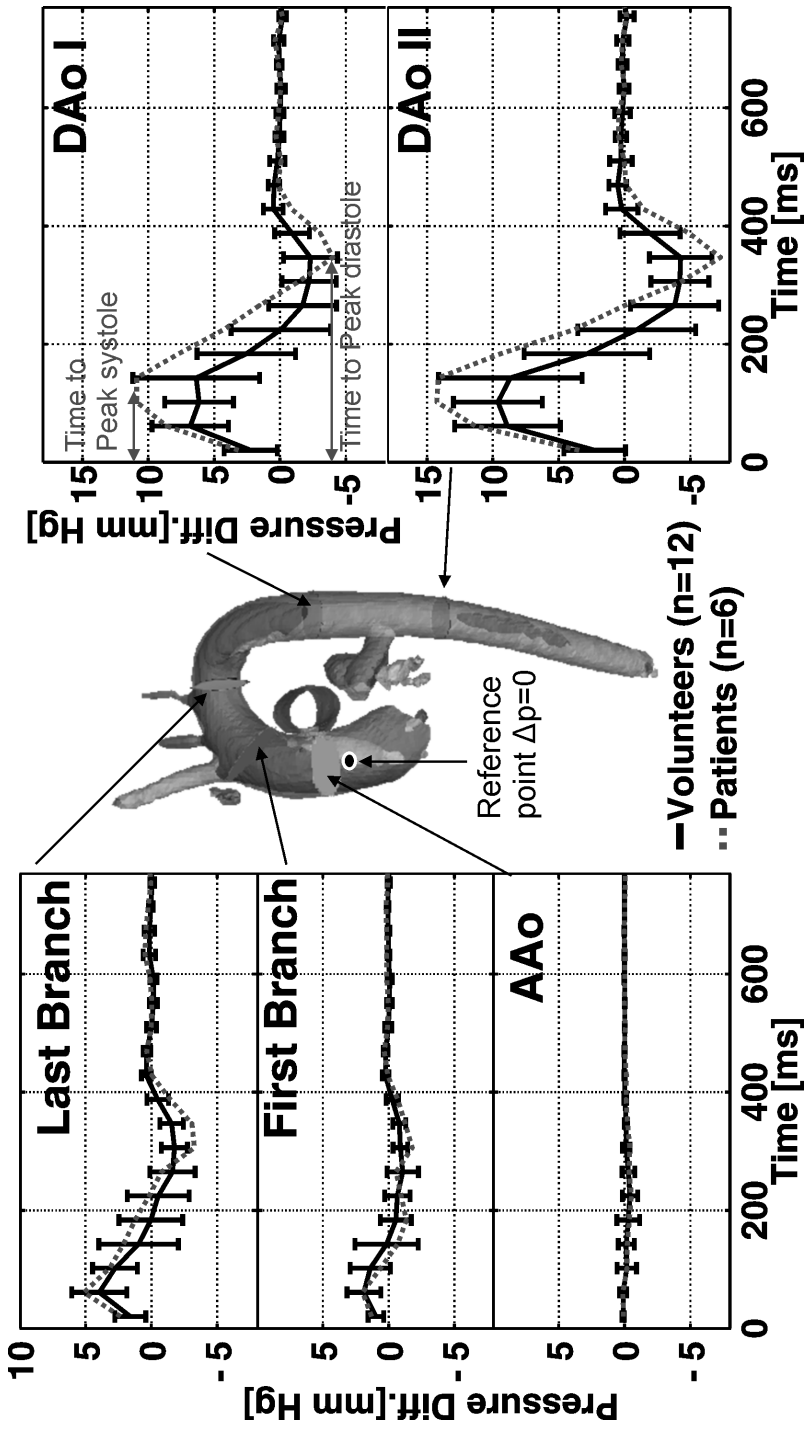

Figure 6.7: *Time-resolved pressure differences in 5 analysis planes relative to the reference point ($\Delta p=0$) averaged over 12 volunteers (solid black line) and over 6 patients with coarctation (dotted gray line). Standard deviations in volunteers represent inter-subject variations. Standard deviations in patients are omitted due to visibility reasons.*

		Peak systolic PD [mmHg]	Time to Peak systolic PD [ms]	Peak diastolic PD [mmHg]	Time to Peak diastolic PD [ms]
Last Branch	Healthy subjects	4.7 ± 1.8 (3.2 - 9.5)	54.8 ± 27.1 (21 - 117)	-2.9 ± 1.7 (-1.1 - -6.6)	269.5 ± 69.7 (122 - 359)
	Patients	9.6 ± 5.0 (1.5 - 15.5)	89.3 ± 73.3 (22 - 203)	-6.1 ± 4.4 (-0.5 - -10)	319.2 ± 33 (286 - 362)
	t-test	$p < 0.05$	NS	NS	$p < 0.05$
DAo II	Healthy subjects	12.5 ± 2.9 (8.5 - 17.9)	89.7 ± 33.6 (36 - 124)	-6.0 ± 2.0 (-3.4 - -10.0)	291.5 ± 45.6 (208 - 368)
	Patients	24.7 ± 13.8 (11.1 - 50.7)	134.3 ± 37.6 (81 - 194)	-11.6 ± 4.2 (-5.3 - 16.8)	323.8 ± 21.0 (295 - 351)
	t-test	$p < 0.05$	$p < 0.05$	$p < 0.05$	$p < 0.05$

Table 6.7: *Comparison of peak and time to peak pressure differences (PD) between healthy subjects and patients for two anatomical positions (Last Branch and DAo II as depicted in figure 6.7). Values are given as mean ± standard deviation with the minimum-maximum range in brackets. NS = not significant.*

	Pressure gradients along predefined paths [mmHg]			
	AAo ↔ DAoII	First supra-aortic branch ↔ Last supra-aortic branch	AAo ↔ First supra-aortic branch	Number of volunteers
Study 1 [10]	11/-5	n.a.	n.a.	1
Study 2 [11]	n.a.	3/-2	n.a.	1
Study 3 [114]	n.a.	1/-0.6	0.6/-0.4	1
This study [119]	7/-3	2/-1	1.9/-0.4	12

Table 6.8: *Comparison of MR pressure gradients derived along specified paths from previous work with results of this study. Values are given as maximum vs. minimum. n.a = not available.*

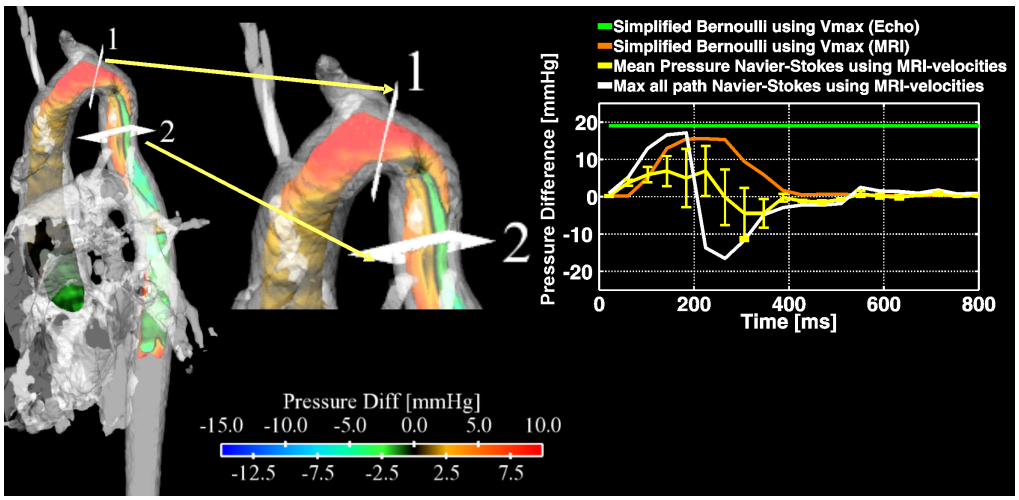

Figure 6.8: *4D pressure difference mapping in one patient with aortic coarctation. The upper part illustrates the analysis strategy for patient 2. Upper left: 3D systolic pressure differences directly mapped onto the aorta; Upper right: yellow curve: time-resolved mean pressure gradient between planes 1 and 2 calculated from MR data using Navier-Stokes modeling; white curve: time-resolved peak pressure gradient calculated from MR data using Navier-Stokes modeling; orange curve: time-resolved pressure gradient value calculated using simplified Bernoulli equation with peak velocity measured in MRI; green curve: pressure gradient measured using echocardiography.*

	Peak mean pressure gradients	**Simplified Bernoulli**	**Pressure gradients using all possible paths**
Underestimation [%]	60.1 ± 17.8	41.3 ± 9.9	14.7 ± 15.5
Correlation coefficient	NS	r = 0.94	r = 0.96
t-test	NS	$p < 0.05$	$p < 0.05$

Table 6.9: *Results of pressure gradients determined in three ways from MRI compared to echocardiography. NS = not significant.*

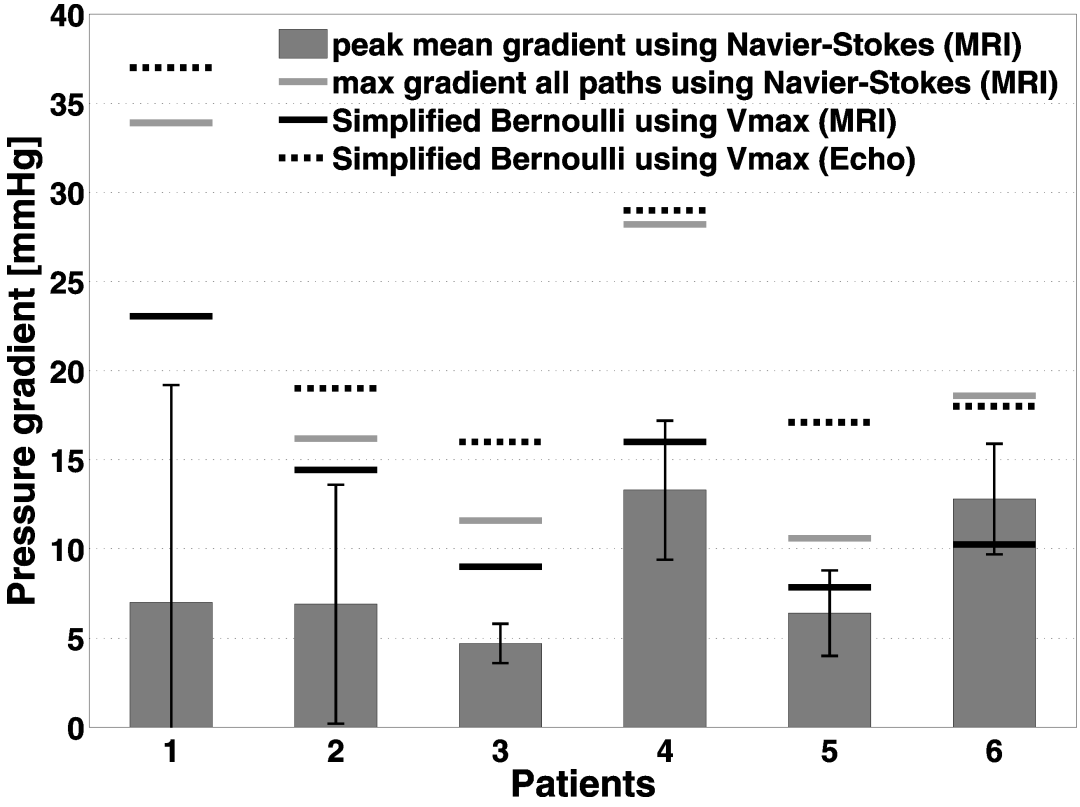

Figure 6.9: *Comparison of peak pressure gradients across aortic coarctation measured in echocardiography (black dotted line) and calculated from MRI data using simplified Bernoulli equation (black solid line), the Navier-Stokes equation (gray bars, peak mean difference between analysis planes ± standard deviation), and as maximum of all possible paths between planes 1 and 2 in figure 6.8 (gray solid line).*

6.2.1.4 In vivo study III

In 5 patients mean and peak pressure gradients across the aortic coarctation calculated using PC-MRI data in conjunction with static and time-resolved vessel geometry were compared to the catheter and echocardiography measurements at the same location (table 6.10). Mean pressure gradient determined with MRI in time-resolved segmentation shows moderate deviation from the standard method (catheterization) in 3 out of 5 patients (patients 01, 03, 04) by 15 ± 11%. By using static segmentation, the deviation increases to 59 ± 23% in the same patients.
In patient 02 the MRI pressure gradient was strongly overestimated for both calculations using MRI data compared to the catheter measurement. In patient 05 the pressure gradient was underestimated by 45% for time-resolved vessel geometry and by 60% using static segmentation compared to the catheter. However, the MRI data were acquired almost 2 years before the intervention. In such long period the pressure gradient might change.

Pressure gradients [mmHg]	01	02	03	04	05
Catheter (normal)	5	7	15	12	20
Catheter (stress)	n.a.	10	50	12	20
Echo (mean)	12	16	20	12	15
Echo (max)	22	37	50	38	36
MRI (mean), 4D PC-MRA	5	21	12	15	11
MRI (max), 4D PC-MRA	16	26	44	23	14
MRI (mean), 3D PC-MRA	3	21	22	23	8
MRI (max), 3D PC-MRA	20	28	57	27	13
Catheterization after MR [months]	0.1	2.2	2.8	2.7	20.3

Table 6.10: *Comparison of pressure gradients measured using different modalities (catheter, echocardiography and MRI) in five patients. For calculation of pressure gradients with MRI 3D and 4D PC-MRA were used. n.a = not available. Last row provides information on delay between the MR study and catheterization procedure.*

7 Discussion and Conclusion

7.1 Summary

In summary, our study showed the feasibility of time-averaged PC-MRA calculation from flow sensitive 4D MRI data for the thoracic aorta and supra-aortic branches. The application of contrast agent significantly improved vascular SNR and velocity noise, and helped to improve flow visualization and background suppression.
Clustering results indicate the potential of FCM for time-resolved 3D (4D) vessel segmentation. In comparison to the rigid segmentation, flow parameters could be determined more accurately and the aortic motion could be depicted over the cardiac cycle.
Pressure gradient study demonstrates the potential of the applied approach to derive 4D pressure gradients from time-resolved 3D PC-MRI. In addition to encouraging phantom comparison results, *in vivo* MRI-derived pressure gradients showed moderate deviation compared to the available clinical standard echocardiography and catheter measurements.

7.2 Discussion

7.2.1 3D PC-MRA

Our results indicate significant differences in the PC-MRA generated by the different algorithms. Based on qualitative and quantitative results, algorithm $PCMRA^1$ (equation (4.1)) found to be best suited for the calculation of aortic PC-MRA, since its demonstrated more homogeneous aortic lumen and good CNR.
Further investigations based on the above-mentioned algorithm demonstrated that derivation of a time-averaged 3D PC-MRA from flow-sensitive 4D MRI is feasible for the thoracic aorta and supra-aortic branches. It is possible to derive vessel geometry even for data acquired without contrast agent administration. However, smaller vessels were difficult to visualize without contrast agent administration, and in general the application of contrast agent affected image quality of PC-MRA positively and provided improved background suppression.

Influence of contrast agents

As expected, flow sensitive 4D MRI data acquired with contrast agent provided improved SNR in magnitude data and noise reduction in velocity data compared to measurements without contrast media. But SNR in data with contrast agent showed significantly higher variation among the population of each subgroup (with BPA and with ECA). This increased variance occurs presumably due to different scan timing and contrast agent elimination rates, e.g. because of different amounts of remaining contrast agent in the vascular system. Furthermore, these differences between subjects were most likely related to the differences in times of scan initiation after contrast agent administration. Since such variances may affect image quality, future studies should include the effect of scan timing and duration in more detail.

Compared to the reference standard CE-MRA, PC-MRA data showed reliable geometry depiction of the thoracic aorta and major supra-aortic branches. It should be noted that standard CE-MRA is clearly superior compared to the derived PC-MRA for the detailed depiction of vascular anatomy. Nevertheless, our results demonstrate that large vascular structures such as the thoracic aorta and major branches can be extracted reliably from the acquired 4D flow sensitive data and combined with 3D visualization.

Evaluation of 3D blood flow visualization quality was performed using streamlines, which represent the current velocity vector field and do not have temporal continuity. Their relative length and relative number for each acquired time frame were used to evaluate blood flow visualization quality, and a trend towards improved results for the data with contrast agent was observed. However, compared to data without contrast agent, the differences were statistically insignificant. A possible explanation of the lack of significant improvement may be provided by the longer TE of PC-MRA compared to CE-MRA, which could potentially reduce the effect of the contrast agent. Further, it has to be noted that identical flow sensitive 4D MRI sequence parameters were used for the acquisition of the data in all volunteers. Pulse sequence parameters were previously optimized for patients who underwent flow sensitive MRI after contrast agent administration [51, 120] and thus provided optimal results for the volunteer subgroup with standard contrast agent (ECA). By using identical sequence parameters for all measurements, it was probable that we did not get the maximum possible SNR from subgroups without contrast agent and with blood pool contrast agent. Therefore there is a need for additional phantom and *in vivo* studies to optimize the repetition time TR, echo time TE, flip angle, and maybe contrast agent doses when using blood pool CA in 4D flow sensitive measurements. The use of independently optimized parameters for subgroups without contrast agent and with blood pool contrast agent

would probably improve individual results and may help to further improve PC-MRA and flow visualization.
Nevertheless, the results presented here already indicate the improvements associated with different contrast agents, and in particular the potential of blood pool agents to enhance PC-MRA and blood flow visualization quality.
PC-MRA as performed in this study cannot compete with the much faster CE-MRA with its higher spatial resolution and increased signal due to shorter echo times and larger flip angles, resulting in better depiction of smaller vessels. Nevertheless, PC-MRA can be an alternative, since it is time- and thus bolus- independent and can be used without contrast agent administration. The quality of PC-MRA is not only dependent on the available SNR but also on velocity sensitivity (v_{enc}) and thus underlying blood flow velocities. It is therefore important to adapt the velocity sensitivity to the vascular region of interest, i.e. low v_{enc} for smaller arteries or veins with low flow and high v_{enc} for large arteries with high flow. However, since PC-MRA data depict both arterial and venous structures the evaluation of arterial pathologies may thus be more difficult on PC-MRA compared to CE-MRA with clearly defined arterial phases. Future developments will thus include information on flow direction, pulsatility, flow rates etc. inherent in the flow sensitive MRA data to separate retrospectively venous and arterial regions.
On the other hand, in CE-MRA a clear depiction of vascular structures during the venous phase is often difficult due to lower contrast agent concentration, and additional enhancement of organs and tissue. In this context, PC-MRA may be used for simultaneous visualization of arterial and venous system which may be useful for the evaluation of complex congenital disease affecting arterial and venous structures, as demonstrated in [121]. Additionally, the acquired flow sensitive data can be combined with calculated vessel geometry, and the determined vessel boundaries can be used for derivation of further hemodynamic parameters such as wall shear stress or pressure gradients [9, 10, 111].

7.2.2 Clustering of PC-MRI data

The presented results indicate the potential of FCM clustering for time-resolved 3D vessel segmentation. One of the advantages of the presented approach is that the segmentation is not based on any shape models (tubes, cylinders etc.) so it can be applied to various vascular pathologies and vessel deformations as shown in our study.
Furthermore, static tissue does not need to be determined extra, but is calculated simultaneously and can be used for subsequent eddy current correction without further

user interaction.
Limitations of the current implementation are related to low velocity in early systole and in diastole, which resulted in incomplete depiction of vessel boundaries during these time frames. Thus, time-resolved PC-MRA tends to underestimate the derived hemodynamic parameters. To overcome the problem with low velocities in early systole and diastole and therefore incomplete depiction of vessel structures, especially in the descending aorta, one can use PC-MRI acquisition with dual velocity encoding, which is suited for vascular regions with wide ranges of velocities [122]. Furthermore, dual velocity encoding would supersede the pre-processing of velocity data before clustering process (section 5.1.1) and thus save computational time.
Additional improvement of the data quality during acquisition could be achieved by using 32-channel coil instead of 12-channel coil [123], which will result in better quality (higher SNR) of the magnitude data and might make the inhomogeneity correction redundant and thus will save computational time as well.
In comparison to the rigid segmentation, flow could be determined more accurately. Advantages of the presented approach are that time-resolved segmentation follows the general motion of the aorta during the cardiac cycle. As a result, the incorporation of the noisy values from outside the vessel is reduced compared to a rigid segmentation.
One difficulty is the separation of the pulmonary artery from the aorta due to partial volume effect, which occurs if the pulmonal artery and aorta are very close to each other. A solution to this problem could be a data acquisition with better temporal and spatial resolutions. However, in order to not to increase the measuring time by the improvement in resolution, data acquisition would benefit from parallel imaging with high acceleration factors [124]. Especially the segmentation of children's small aorta would benefit from higher spatial resolution, since the aorta is smaller compared to the adults. Additionally, the heart rate is higher in children, and thus less time points can be acquired during cardiac cycle, and this can be improved by a better temporal resolution.
Further limitations is that the presented approach was tested and applied so far in large vessels (aorta, pulmonal artery) only. Since flow-sensitive PC-MRI is applied in many other vascular territories such as brain, neck, liver etc., future studies should investigate the applicability to smaller vessels which might also include the analysis of further features and/or features combinations.

7.2.3 Applications using vessel boundaries

The results of our *in vitro* and *in vivo* pressure difference studies demonstrate the potential of 4D pressure gradient mapping based on flow-sensitive 4D MRI data. The advantage of the presented method is related to the possibility to derive time-resolved 3D pressure differences. The complete spatial and temporal coverage may help to evaluate the impact of local pathologies on regional and global pressure gradient alterations in the entire system over time. Furthermore, one can combine pressure gradient data with additional information from flow-sensitive 4D PC-MRI such as flow visualization (vector fields, streamlines, particle traces), flow quantification and derived wall parameters (wall shear stress, etc.). Such combination of multiple parameters may provide new insights in the development of secondary pathologies (e.g. post stenotic aneurysms).

In-vitro measurements
In the presented study, comparison based on a stenosis model and constant flow showed good agreement between different approaches using Navier-Stokes, the modified Bernoulli and simplified Bernoulli equation. Further, the investigation of a stenosis model using pulsatile flow demonstrated the intrinsic consistency of the MRI data.
However, no additional measurements using another modality were performed to obtain an independent measure of the pulsatile flow waveform inside the phantom. It was thus not possible to calculate the expected pressure based on the flow curve and known geometry. Nevertheless, the presented comparisons between pressure differences using Navier Stokes modeling with standard methods (Bernoulli) for pulsatile flow indicates the intrinsic consistency of the presented data analysis strategy.

In-vivo study I
The *in vivo* study demonstrated that time-averaged aortic vessel geometry derived from flow sensitive 4D PC-MRI data can be successfully used in parallel with the acquired velocity field to semi-automatically determine time-resolved pressure gradients and 4D pressure differences maps.
Comparison of volunteer and patient data demonstrated the sensitivity of the method for the detection of altered magnitude and dynamics of pressure differences in the presence of atherosclerosis. Future studies including larger number of patients and a three-dimensional analysis of the pressure difference distributions are warranted to evaluate the potential of 4D pressure mapping for the improved characterization of atherosclerosis and its progression during therapy.

In-vivo study II

Pressure differences found in our cohort were in good to moderate agreement with findings in other MRI studies [10, 11, 114] as summarized in table 6.8. But the results from our study reflect average values over 12 healthy subjects while in all other studies only 1 subject was examined, which limits the power of a statistical comparison.

In a study using pressure catheters, Mills et al. [125] determined time-resolved pressure waves at certain positions in the aorta. Between the ascending and descending aorta the difference of peak pressures was approximately 8 mmHg. In our study we found 7 mmHg between approximately the same positions. To our knowledge, to date no other data on spatially- and temporally-resolved aortic relative pressure differences in healthy subjects are available that could be used to compare our results to standard methods such as those by echocardiography or catheter measurements.

Vessel segmentation and in vivo study III

The applied approach for vessel segmentation in *in vivo* studies I and II can only identify the inner part of the aortic lumen and does not provide the exact location of aortic walls due to the applied morphological operations. As a result, not all measured velocity values are included in the calculation of the relative pressure differences. Nevertheless, the time-resolved 3D pressure differences inside the determined lumen could still be reliably estimated from volunteer data as indicated by the consistency of the results (i.e. low inter-individual variations).

But as shown in study III, the pressure calculation benefit from the use of 4D PC-MRA. Since the time-resolved vessel boundary follows the general motion from the aorta and provide more exact location of aortic walls. Thus the incorporation of the velocity values from outside the vessel is limited and leads to more accurate pressure calculations compared to 3D vessel boundaries.

Comparison to echocardiography

In patients the pressure gradients were underestimated compared to echocardiography, which could be explained by the lower spatial and temporal resolution in MRI resulting in partial volume effects and temporal filtering and thus underestimation of peak velocities. Also, turbulence or complex flow resulting in signal dephasing could further compromise the accuracy of pressure gradient estimation from phase contrast MRI [126]. Nevertheless, the maximum pressure gradient of all possible paths within the pathology calculated from MRI velocity data are in good agreement with echocardiography.

However, echocardiography could also have overestimated the pressure gradients. Several studies have reported a close correlation ($r > 0.76$) between Doppler-estimated

and catheterization-determined pressure gradient with a systematic overestimation on the part of echocardiography [127, 128], especially in the setting when the proximal velocities exceed 1m/s or when gradients across the stenosis are low [127]. In mild vessel stenosis (peak Doppler gradient $<$ 20 mmHg [129]), measurement of instantaneous pressure drop by Doppler overestimates the pressure gradient because the velocity proximal to the obstruction is relatively higher to the distal velocity [130]. The patients of our population showed relative small velocity changes (34 $\pm$ 28% using MRI velocities) across the stenotic area, such that proximal velocity and viscous effects have a greater importance than in patients with higher velocity changes. Since velocities are acquired in a window placed in the center of the vessel, echocardiography acquisitions are prone to overestimating velocities, thereby potentially overestimating Δp to an even higher degree (equation (6.1)). Applying the Navier-Stokes approach in patients with mild stenosis may thus help to overcome this overestimation by simplified Bernoulli, since proximal and distal velocities as well as viscous effects are accounted for. Furthermore, the anatomy of the aortic vessel and the shape of the jet-stream have an important impact on the detected flow velocity [128]. Eccentric jet, often seen in coarctation, additionally leads to overestimation when using the simplified Bernoulli approach [131]. Due to complete temporal and spatial coverage in MRI data, it is possible to overcome these limitations and observe pressure development over long distances without being influenced by vessel shape and jet stream location in the stenosis. Furthermore, the presented Navier-Stokes approach could also be applied to regions that cannot be examined with echocardiography. A disadvantage compared to the routinely used Bernoulli method is the long acquisition and computation time. Nevertheless, the Navier-Stokes method was rarely used to date and provides new information (time-resolved 3D pressure maps with volumetric coverage) and future studies are needed to evaluate potential benefits associated with this new information.
A shortcoming of the study setup II (patients with coarctation) is that no pressure catheter measurements were available for the patients, which would constitute the most reliable reference method and could help overcoming limitations of the ultrasound. Furthermore, results presented here for analysis of peak systolic PD and time-to-peak systolic PD revealed significant differences for all parameters determined in a plane distal to the pathology. In the plane proximal to the stenosis higher systolic pressure differences and later occurrence of the diastolic peak were of statistical significance. However, these results were determined in a small cohort of patients and further investigations are needed including a larger number of patients.

Comparison to catheter

Pressure gradient comparisons between catheter and MRI show the potential of MR approach to determine the pressure gradient over the coarctation. The study is of great relevance, since it shows that it is also possible with a non-invasive method to determine the pressure gradient. However, the number of study subjects is small and needs to be increased in future studies. Furthermore, MR examinations should be performed within a shorter time interval to the catheter measurements. Since in this time period the coarctation might change and thus will result in gradient change as well. Additionally, medicamentous stress testing might as well be performed in MR measurements.

Another approaches

It is important to note that the iterative approach used in the studies was limited by lengthy computation times and pressure gradient underestimation. In a recent study Ebbers et al. [117] presented a multigrid-based solver for the pressure Poisson equation, which provided faster and better estimates of the relative pressure fields from velocity MRI data compared to the iterative approaches. In this study we did not compare the iterative approach with the method introduced by Ebbers [117]. However, further studies should involve comparisons of both techniques in a large cohort of subjects.

In addition, the pressure gradient estimation required the derivation of local temporal and convective acceleration by calculating spatial and temporal derivatives of the measured time-resolved velocity vector field. The calculation of derived quantities results in noise amplification of the underlying measured data (velocities), and those can corrupt the final pressure gradients. To reduce noise and improving accuracy of the derived quantities, directly acquired acceleration fields with recently reported fast 3D acceleration encoded PC-MRI [132] may help as has been shown in previous studies [112, 133].

In general, in this work presented processing and analysis of 4D flow-sensitive MRI data is a time-consuming process which is suitable for research studies but not for clinical routine. Future work should focuses on fast data acquisition with parallel imaging as well as on faster data processing and analysis. The existing analysis strategy uses different software tools for individual steps such as pre-processing, visualization and quantification. A software solution that supports the whole image analysis pipeline should be developed further.

Additionally, incorporation of further hemodynamic parameters such as wall shear stress [9] and pulse wave velocity [134] into the vessel analysis can contribute to the better understanding of development and progression of vascular pathologies.

Bibliography

[1] *http://www.cprhealth.co.uk/.*

[2] S. Silbernagl and F. Lang. *Taschenatlas Pathophysiologie.* Georg Thieme Verlag, 2009.

[3] J. Mackay, G.A. Mensah, S. Mendis, and K. Greenlund. *The atlas of heart disease and stroke.* World Health Organization, 2004.

[4] D. Saloner. Flow and vascular disease progression. In *Flow and Motion Workshop, New York*, 2006.

[5] N.M. van Popele, D.E. Grobbee, M.L. Bots, R. Asmar, J. Topouchian, R.S. Reneman, A.P.G. Hoeks, D.A.M. van der Kuip, A. Hofman, and J. Witteman. Association between arterial stiffness and atherosclerosis: the rotterdam study. *Stroke*, 32(2):454–460, 2001.

[6] R. van Pelt, H. Nguyen, B. ter Haar Romeny, and A. Vilanova. Automated segmentation of blood-flow regions in large thoracic arteries using 3d-cine pc-mri measurements. *International Journal of Computer Assisted Radiology and Surgery*, published online ahead of print:1–8, 2011.

[7] M. Markl, F.P. Chan, M.T. Alley, K.L. Wedding, M.T. Draney, C.J. Elkins, D.W. Parker, R. Wicker, C.A. Taylor, R.J. Herfkens, et al. Time-resolved three-dimensional phase-contrast mri. *Journal of Magnetic Resonance Imaging*, 17(4):499–506, 2003.

[8] A. Stalder. *Quantitative Analysis of Blood Flow and Vessel Wall Parameters using 4D Flow-Sensitive MRI.* PhD thesis, Albert-Ludwigs-University of Freiburg, 2009.

[9] A. F. Stalder, M. F. Russe, A. Frydrychowicz, J. Bock, J. Hennig, and M. Markl. Quantitative 2d and 3d phase contrast mri: optimized analysis of blood flow and vessel wall parameters. *Magn Reson Med*, 60(5):1218–1231, Nov 2008.

[10] J. M. Tyszka, D. H. Laidlaw, J. W. Asa, and J. M. Silverman. Three-dimensional, time-resolved (4d) relative pressure mapping using magnetic resonance imaging. *J Magn Reson Imaging*, 12(2):321–329, Aug 2000.

[11] T. Ebbers, L. Wigstrom, A. F. Bolger, J. Engvall, and M. Karlsson. Estimation of relative cardiovascular pressures using time-resolved three-dimensional phase contrast mri. *Magn Reson Med*, 45(5):872–9, 2001.

[12] D. Steinman. Cemra based computational fluid dynamics of the carotid bifurcation: a cautionary tale. In *MRA*, 2011.

[13] P.J. Currie, JB Seward, GS Reeder, RE Vlietstra, DR Bresnahan, JF Bresnahan, HC Smith, DJ Hagler, AJ Tajik, et al. Continuous-wave doppler echocardiographic assessment of severity of calcific aortic stenosis: a simultaneous doppler-catheter correlative study in 100 adult patients. *Circulation*, 71(6):1162, 1985.

[14] J.N. Cohn, A.A. Quyyumi, N.K. Hollenberg, and K.A. Jamerson. Surrogate markers for cardiovascular disease functional markers. *Circulation*, 109(25 suppl 1):IV–31, 2004.

[15] *SERVIER Medical Art. www.servier.com.*

[16] A. Despopoulos and S. Silbernagl. *Taschenatlas der Physiologie.* Georg Thieme Verlag, 2007.

[17] R.F. Schmidt, F. Lang, and G. Thews. *Physiologie des Menschen: mit Pathophysiologie.* Springer, 2005.

[18] C. Stefanadis, C. Stratos, H. Boudoulas, C. Kourouklis, and P. Toutouzas. Distensibility of the ascending aorta: comparison of invasive and non-invasive techniques in healthy men and in men with coronary artery disease. *European heart journal*, 11(11):990–996, 1990.

[19] DJ Patel, JC Greenfield, and DL Fry. In vivo pressure-length-radius relationship of certain blood vessels in man and dog. *Pulsatile blood flow*, 1:293–302, 1964.

[20] WH Pearce, MS Slaughter, S. LeMaire, AN Salyapongse, J. Feinglass, WJ McCarthy, and JS Yao. Aortic diameter as a function of age, gender, and body surface area. *Surgery*, 114(4):691, 1993.

[21] K. Kunsch and S. Kunsch. *Der Mensch in Zahlen.* Spektrum, Akad. Verl., 2000.

[22] R. Klinke and R. Baumann. *Physiologie.* Georg Thieme Verlag, 2010.

[23] W.W. Nichols and B.M. Singh. Augmentation index as a measure of peripheral vascular disease state. *Current opinion in cardiology*, 17(5):543–551, 2002.

[24] N. Westerhof, N. Stergiopulos, and M.I.M. Noble. *Snapshots of hemodynamics: an aid for clinical research and graduate education.* Springer Verlag, 2005.

[25] W. Pschyrembel. *Pschyrembel Klinisches Wörterbuch.* de Gruyter, 2001.

[26] D.J. Farrar, M.G. Bond, W.A. Riley, and J.K. Sawyer. Anatomic correlates of aortic pulse wave velocity and carotid artery elasticity during atherosclerosis progression and regression in monkeys. *Circulation*, 83(5):1754–1763, 1991.

[27] M. Reiser, F.P. Kuhn, J. Debus, and H. Holtermann. *Radiologie.* Thieme, 2006.

[28] M. Thelen, R. Erbel, K.F. Kreitner, and J. Barkhausen. *Bildgebende Kardiodiagnostik.* Georg Thieme Verlag, 2007.

[29] P. Summers. *Quantitative Flow by Magnetic Resonance Phase Mapping*. PhD thesis, University of London, 1998.

[30] R. Detrano, A.D. Guerci, J.J. Carr, D.E. Bild, G. Burke, A.R. Folsom, K. Liu, S. Shea, M. Szklo, D.A. Bluemke, et al. Coronary calcium as a predictor of coronary events in four racial or ethnic groups. *New England Journal of Medicine*, 358(13):1336–1345, 2008.

[31] M. Wintermark, SS Jawadi, JH Rapp, T. Tihan, E. Tong, DV Glidden, S. Abedin, S. Schaeffer, G. Acevedo-Bolton, B. Boudignon, et al. High-resolution ct imaging of carotid artery atherosclerotic plaques. *American Journal of Neuroradiology*, 29(5):875–882, 2008.

[32] MG Van der Vaart, R. Meerwaldt, R. Slart, GM van Dam, RA Tio, and CJ Zeebregts. Application of pet/spect imaging in vascular disease. *European Journal of Vascular and Endovascular Surgery*, 35(5):507–513, 2008.

[33] J.E. Aldrich. Basic physics of ultrasound imaging. *Critical care medicine*, 35(5):S131, 2007.

[34] O. Dössel. *Bildgebende Verfahren in der Medizin*. Springer, 2000.

[35] S. Moltzahn and M. Zeydabadinejad. *Dopplerechokardiographie*. Georg Thieme Verlag, 2000.

[36] B. Eklöf, K. Lindström, and S. Persson. *Ultrasound in Clinical Diagnosis: From Pioneering Developments in Lund to Global Application in Medicine*. Oxford University Press, 2012.

[37] E.M. Haacke, R.W. Brown, M.R. Thompson, and R. Venkatesan. *Magnetic resonance imaging: physical principles and sequence design*. Wiley New York, 1999.

[38] G.J. Stanisz, E.E. Odrobina, J. Pun, M. Escaravage, S.J. Graham, M.J. Bronskill, and R.M. Henkelman. T1, t2 relaxation and magnetization transfer in tissue at 3t. *Magnetic resonance in medicine*, 54(3):507–512, 2005.

[39] O. Al-Kwifi, D.J. Emery, and A.H. Wilman. Vessel contrast at three tesla in time-of-flight magnetic resonance angiography of the intracranial and carotid arteries. *Magnetic resonance imaging*, 20(2):181–187, 2002.

[40] E.L. Hahn. Spin echoes. *Physical Review*, 80(4):580–594, 1950.

[41] H.Y. Carr and E.M. Purcell. Effects of diffusion on free precession in nuclear magnetic resonance experiments. *Physical Review*, 94(3):630–638, 1954.

[42] J.P. Ridgway. Cardiovascular magnetic resonance physics for clinicians: part i. *Journal of Cardiovascular Magnetic Resonance*, 12(1):71, 2010.

[43] SiemensAG. *Magnets, Spins, and Resonances; An introduction to the basics of Magnetic Resonance*. Siemens Medical Solutions, 2003.

[44] D. Weishaupt, V.D. Köchli, and B. Marincek. *Wie funktioniert MRI?: eine Einführung in Physik und Funktionsweise der Magnetresonanzbildgebung*. Springer Medizin Verlag Heidelberg, Heidelberg, 2009.

[45] S. Bauer. *Entwicklung und Analyse von Beschleunigungsmethoden für die funktionelle Untersuchung des kardiovaskulären Systems mit Magnetresonanztomographie*. PhD thesis, Albert-Ludwigs-Universität, Freiburg im Breisgau, 2011.

[46] Michael Markl. *Funktionelle kardiale Phasenkontrast MRT: Entwicklung und Erprobung von Phasenkontrast-Methoden zur Darstellung und Beurteilung von Bewegungsabläufen am menschlichen Herzen*. PhD thesis, Albert-Ludwigs-Universität Freiburg im Breisgau, 2000.

[47] Michael Markl and Jochen Leupold. Gradient echo imaging. *Journal of Magnetic Resonance Imaging*, 35(6):1274–1289, 2012.

[48] M.F. Reiser, W. Semmler, and H. Hricak. *Magnetic resonance tomography*. Springer Verlag, 2007.

[49] B. Schulte, A. Boldt, and D. Beyer. *MRT des Herzens und der Gefäße: Indikationen-Strategien-Abläufe-Ergebnisse*. Springer Verlag, 2005.

[50] D. Giese. Neue methoden der atembewegungskompensation in der kardiovaskulären mrt mittels ultraschall. Master's thesis, University of Karlsruhe, 2009.

[51] M. Markl, A. Harloff, T.A. Bley, M. Zaitsev, B. Jung, E. Weigang, M. Langer, J. Hennig, and A. Frydrychowicz. Time-resolved 3d mr velocity mapping at 3t: Improved navigator-gated assessment of vascular anatomy and blood flow. *Journal of Magnetic Resonance Imaging*, 25(4):824–831, 2007.

[52] S. Uribe, P. Beerbaum, T.S. Sørensen, A. Rasmusson, R. Razavi, and T. Schaeffter. Four-dimensional (4d) flow of the whole heart and great vessels using real-time respiratory self-gating. *Magnetic Resonance in Medicine*, 62(4):984–992, 2009.

[53] M. Markl. Techniques in the assessment of cardiovascular blood flow and velocity. Technical report, University Hospital Freiburg, Departement of Diagnostic Radiology, Medical Physics, 2005.

[54] M.A. Bernstein, A. Shimakawa, and N.J. Pelc. Minimizing te in moment-nulled or flow-encoded two-and three-dimensional gradient-echo imaging. *Journal of Magnetic Resonance Imaging*, 2(5):583–588, 1992.

[55] D. Giese. Analysis and correction of artifacts in phase contrast magnetic resonance imaging (pc-mri). Master's thesis, University Karlsruhe, 2007.

[56] Jelena Bock. Programm zur bearbeitung von funktionellen zeitaufgelösten mrt-volumendaten. Master's thesis, FH Ulm, 2006.

[57] P. Chai and R. Mohiaddin. How we perform cardiovascular magnetic resonance flow assessment using phase-contrast velocity mapping. *Journal of Cardiovascular Magnetic Resonance*, 7(4):705–716, 2005.

[58] S. Heiland. From a as in aliasing to z as in zipper: Artifacts in mri. *Clinical Neuroradiology*, 18(1):25–36, 2008.

[59] D.L. Pham, C. Xu, and J.L. Prince. Current methods in medical image segmentation 1. *Annual review of biomedical engineering*, 2(1):315–337, 2000.

[60] O. Salvado, C. Hillenbrand, S. Zhang, and DL Wilson. Method to correct intensity inhomogeneity in mr images for atherosclerosis characterization. *Medical Imaging, IEEE Transactions on*, 25(5):539–552, 2006.

[61] U. Vovk, F. Pernus, and B. Likar. A review of methods for correction of intensity inhomogeneity in mri. *Medical Imaging, IEEE Transactions on*, 26(3):405–421, 2007.

[62] A. Chernobelsky, O. Shubayev, C. R Comeau, and S. D Wolff. Baseline correction of phase contrast images improves quantification of blood flow in the great vessels. *J Cardiovasc Magn Reson*, 9(4):681–685, 2007.

[63] M.A. Bernstein, X.J. Zhou, J.A. Polzin, K.F. King, A. Ganin, N.J. Pelc, and G.H. Glover. Concomitant gradient terms in phase contrast mr: analysis and correction. *Magnetic resonance in medicine*, 39(2):300–308, 1998.

[64] M. Markl, R. Bammer, MT Alley, CJ Elkins, MT Draney, A. Barnett, ME Moseley, GH Glover, and NJ Pelc. Generalized reconstruction of phase contrast mri: analysis and correction of the effect of gradient field distortions. *Magnetic resonance in medicine*, 50(4):791–801, 2003.

[65] L. Ying, Z.P. Liang, D.C. Munson Jr, R. Koetter, and B.J. Frey. Unwrapping of mr phase images using a markov random field model. *Medical Imaging, IEEE Transactions on*, 25(1):128–136, 2005.

[66] Q.S. Xiang. Temporal phase unwrapping for cine velocity imaging. *Journal of Magnetic Resonance Imaging*, 5(5):529–534, 1995.

[67] J.S. Suri, K. Liu, L. Reden, and S. Laxminarayan. A review on mr vascular image processing: skeleton versus nonskeleton approaches: part ii. *Information Technology in Biomedicine, IEEE Transactions on*, 6(4):338–350, 2002.

[68] C. Kirbas and F. Quek. A review of vessel extraction techniques and algorithms. *ACM computing surveys*, 36(2):81–121, 2004.

[69] David Lesage, Elsa D Angelini, Isabelle Bloch, and Gareth Funka-Lea. A review of 3d vessel lumen segmentation techniques: models, features and extraction schemes. *Med Image Anal*, 13(6):819–845, Dec 2009.

[70] R.C. Gonzalez and R.E. Woods. *Digital image processing*. Pearson Education, Inc., 2008.

[71] J.S. Suri, D.L. Wilson, and S. Laxminarayan. *Handbook of Biomedical Image Analysis: Volume II: Segmentation Models*, volume 2. Kluwer Academic/ Plenum Publishers, New York, 2005.

[72] N. Otsu. A threshold selection method from gray-level histograms. *Automatica*, 11:285–296, 1975.

[73] M. Kass, A. Witkin, and D. Terzopoulos. Snakes: Active contour models. *International journal of computer vision*, 1(4):321–331, 1988.

[74] S. Kozerke, R. Botnar, S. Oyre, M.B. Scheidegger, E.M. Pedersen, and P. Boesiger. Automatic vessel segmentation using active contours in cine phase contrast flow measurements. *Journal of Magnetic Resonance Imaging*, 10(1):41–51, 1999.

[75] R. L. Janiczek, F. H. Epstein, and S. T. Acton. Velocity guided segmentation of phase contrast magnetic resonance angiography. In *Proc. 15th IEEE Int. Conf. Image Processing ICIP 2008*, pages 2264–2267, 2008.

[76] K. S. Sundareswaran, D.H. Frakes, M. A. Fogel, D. D. Soerensen, J. N. Oshinski, and A.P. Yoganathan. Optimum fuzzy filters for phase-contrast magnetic resonance imaging segmentation. *J Magn Reson Imaging*, 29(1):155–165, Jan 2009.

[77] A.C.S. Chung, J.A. Noble, and P. Summers. Vascular segmentation of phase contrast magnetic resonance angiograms based on statistical mixture modeling and local phase coherence. *Medical Imaging, IEEE Transactions on*, 23(12):1490–1507, 2004.

[78] Jan Solem, Markus Persson, and Anders Heyden. Velocity based segmentation in phase contrast mri images. In Christian Barillot, David Haynor, and Pierre Hellier, editors, *Medical Image Computing and Computer-Assisted Intervention MICCAI 2004*, volume 3216 of *Lecture Notes in Computer Science*, pages 459–466. Springer Berlin / Heidelberg, 2004.

[79] Fei Zhao, Honghai Zhang, Andreas Wahle, Matthew T Thomas, Alan H Stolpen, Thomas D Scholz, and Milan Sonka. Congenital aortic disease: 4d magnetic resonance segmentation and quantitative analysis. *Med Image Anal*, 13(3):483–493, Jun 2009.

[80] R.K. Johnson, S. Premraj, S.S. Patel, N. Walker, A. Wahle, M. Sonka, and T.D. Scholz. Automated analysis of four-dimensional magnetic resonance images of the human aorta. *The International Journal of Cardiovascular Imaging (formerly Cardiac Imaging)*, 26(5):571–578, 2010.

[81] M. Schmidt, R. Unterhinninghofen, S. Ley, and R. Dillmann. Flow-based segmentation of the large thoracic arteries in tridirectional phase-contrast mri. In *Proceedings of SPIE*, volume 7259, page 725914, 2009.

[82] J.C. Bezdek. *Pattern recognition with fuzzy objective function algorithms*. Plenum Press, New York, 1981.

[83] A.K. Jain, M.N. Murty, and P.J. Flynn. Data clustering: a review. *ACM computing surveys (CSUR)*, 31(3):264–323, 1999.

[84] A.K. Jain and R.C. Dubes. *Algorithms for clustering data*. Prentice-Hall, Inc., 1988.

[85] A.I. Shihab. *Fuzzy clustering algorithms and their application to medical image analysis*. PhD thesis, University of London, 2000.

[86] J. Beutel, M. Sonka, and J.M. Fitzpatrick. *Handbook of Medical Imaging: Medical image processing and analysis*. Society of Photo Optical, 2000.

[87] S. Theodoridis and K. Koutroumbas. *Pattern recognition (Third edition)*. Academic Press, Elsevier, 3rd edition edition, 2006.

[88] L.A. Zadeh. Fuzzy sets*. *Information and control*, 8(3):338–353, 1965.

[89] K. S. Chuang, H. L. Tzeng, S. Chen, J. Wu, and T. J. Chen. Fuzzy c-means clustering with spatial information for image segmentation. *Comput Med Imaging Graph*, 30(1):9–15, 2006.

[90] J. C. Bezdek, L. O. Hall, and L. P. Clarke. Review of mr image segmentation techniques using pattern recognition. *Med Phys*, 20(4):1033–1048, 1993.

[91] I.N. Bankman. *Handbook of medical imaging: processing and analysis*. Academic Press, 2009.

[92] M. Misiti, Y. Misiti, G. Oppenheim, and J.M. Poggi. *Wavelet Toolbox 4*. Mathworks, 1997.

[93] A. Haar. Zur theorie der orthogonalen funktionensysteme. *Mathematische Annalen*, 69(3):331–371, 1910.

[94] J. Sijbers, A.J. Den Dekker, P. Scheunders, and D. Van Dyck. Maximum-likelihood estimation of rician distribution parameters. *Medical Imaging, IEEE Transactions on*, 17(3):357–361, 1998.

[95] J. Bock, B. W. Kreher, J. Hennig, and M. Markl. Optimized pre-processing of time-resolved 2d and 3d phase contrast mri data. In *15th Scientific Meeting International Society for Magnetic Resonance in Medicine*, page 3138, Berlin, Germany, 2007.

[96] P. G. Walker, G. B. Cranney, M. B. Scheidegger, G. Waseleski, G. M. Pohost, and A. P. Yoganathan. Semiautomated method for noise reduction and background phase error correction in mr phase velocity data. *J Magn Reson Imaging*, 3(3):521–530, 1993.

[97] J. Bock, O. Wieben, K. Johnson, J. Hennig, and M. Markl. Optimal processing to derive static pc-mra from time-resolved 3d pc-mri data. In *16th Scientific Meeting, International Society for Magnetic Resonance in Medicine, Toronto (03.-09.05.2008)*, page 3053, 2008.

[98] A. Anderson, K. Johnson, J. Bock, M. Markl, and O. Wieben. Comparison of image reconstruction algorithms for the depiction of vessel anatomy in pc vipr datasets. In *16th Scientific Meeting, International Society for Magnetic Resonance in Medicine, Toronto (03.-09.05.2008)*, page 934, 2008.

[99] M. Rohrer, H. Bauer, J. Mintorovitch, M. Requardt, and H.J. Weinmann. Comparison of magnetic properties of mri contrast media solutions at different magnetic field strengths. *Investigative radiology*, 40(11):715, 2005.

[100] D.G. Altman and J.M. Bland. Measurement in medicine: the analysis of method comparison studies. *The statistician*, 32:307–317, 1983.

[101] M. Bland and D.G. Altman. Statistical methods for assessing agreement between two methods of clinical measurement. *The lancet*, 327(8476):307–310, 1986.

[102] H. Gudbjartsson and S. Patz. The rician distribution of noisy mri data. *Magnetic Resonance in Medicine*, 34(6):910–914, 1995.

[103] S. Napel, D. H. Lee, R. Frayne, and B. K. Rutt. Visualizing three-dimensional flow with simulated streamlines and three-dimensional phase-contrast mr imaging. *J Magn Reson Imaging*, 2(2):143–153, 1992.

[104] M. H. Buonocore. Algorithms for improving calculated streamlines in 3-d phase contrast angiography. *Magn Reson Med*, 31(1):22–30, 1994.

[105] J.N. Cohn, A.A. Quyyumi, N.K. Hollenberg, and K.A. Jamerson. Surrogate markers for cardiovascular disease. *Circulation*, 109(25 suppl 1):IV–31, 2004.

[106] L.A. Walder and F.A. Schaller. Diagnostic cardiac catheterization. when is it appropriate? *Postgraduate medicine*, 97(3):37, 1995.

[107] J.S. Skinner and P.C. Adams. Outpatient cardiac catheterisation. *International journal of cardiology*, 53(3):209–219, 1996.

[108] J. Bock, A. Frydrychowicz, R. Lorenz, D. Hirtler, A.J. Barker, K.M. Johnson, R. Arnold, H. Burkhardt, J. Hennig, and M. Markl. In vivo noninvasive 4d pressure difference mapping in the human aorta: Phantom comparison and application in healthy volunteers and patients. *Magnetic Resonance in Medicine*, 66:1079–1088, 2011.

[109] L. Hatle, A. Brubakk, A. Tromsdal, and B. Angelsen. Noninvasive assessment of pressure drop in mitral stenosis by doppler ultrasound. *British Heart Journal*, 40(2):131–140, 1978.

[110] J.N. Oshinski, W.J. Parks, C.P. Markou, H.L. Bergman, B.E. Larson, D.N. Ku, S. Mukundan Jr, and R.I. Pettigrew. Improved measurement of pressure gradients in aortic coarctation by magnetic resonance imaging. *Journal of the American College of Cardiology*, 28(7):1818–1826, 1996.

[111] G.Z. Yang, P.J. Kilner, N.B. Wood, S.R. Underwood, and D.N. Firmin. Computation of flow pressure fields from magnetic resonance velocity mapping. *Magnetic Resonance in Medicine*, 36(4):520–526, 1996.

[112] F. Balleux-Buyens, O. Jolivet, J. Bittoun, and A. Herment. Velocity encoding versus acceleration encoding for pressure gradient estimation in mr haemodynamic studies. *Physics in Medicine and Biology*, 51:4747–4758, 2006.

[113] R. Lorenz, C. Benk, J. Bock, AF Stalder, JG Korvink, J. Hennig, and M. Markl. Closed circuit mr compatible pulsatile pump system using a ventricular assist device and pressure control unit. *Magnetic Resonance in Medicine*, 67(1):258–68, 2012.

[114] T. Nagao, K. Yoshida, K. Okada, S. Miyazaki, T. Ueguchi, and K. Murase. Development of a noninvasive method to measure intravascular and intracardiac pressure differences using magnetic resonance imaging. *Magnetic Resonance in Medical Sciences*, 7(3):113–122, 2008.

[115] L. Søndergaard, F. Ståhlberg, C. Thomsen, A. Stensgaard, K. Lindvig, and O. Henriksen. Accuracy and precision of mr velocity mapping in measurement of stenotic cross-sectional area, flow rate, and pressure gradient. *Journal of Magnetic Resonance Imaging*, 3(2):433–437, 1993.

[116] J.L. Rodgers and W.A. Nicewander. Thirteen ways to look at the correlation coefficient. *American Statistician*, 42:59–66, 1988.

[117] T. Ebbers and G. Farneback. Improving computation of cardiovascular relative pressure fields from velocity mri. *J Magn Reson Imaging*, 30(1):54–61, 2009.

[118] D.A. McDonald. The relation of pulsatile pressure to flow in arteries. *The Journal of physiology*, 127(3):533–552, 1955.

[119] J. Bock, A. Frydrychowicz, A.F. Stalder, T.A. Bley, H. Burkhardt, J. Hennig, and M. Markl. 4d phase contrast mri at 3 t: Effect of standard and blood-pool contrast agents on snr, pc-mra, and blood flow visualization. *Magnetic Resonance in Medicine*, 63(2):330–338, 2010.

[120] A. Frydrychowicz, A. Harloff, B. Jung, M. Zaitsev, E. Weigang, T.A. Bley, M. Langer, J. Hennig, and M. Markl. Time-resolved, 3-dimensional magnetic resonance flow analysis at 3 t: visualization of normal and pathological aortic vascular hemodynamics. *Journal of computer assisted tomography*, 31(1):9, 2007.

[121] A. Frydrychowicz, R. Arnold, A. Harloff, C. Schlensak, J. Hennig, M. Langer, and M. Markl. In vivo 3-dimensional flow connectivity mapping after extracardiac total cavopulmonary connection. *Circulation*, 118(2):e16–e17, 2008.

[122] E.J. Nett, K.M. Johnson, A. Frydrychowicz, A.M. Del Rio, E. Schrauben, C.J. Francois, and O. Wieben. Four-dimensional phase contrast mri with accelerated dual velocity encoding. *Journal of Magnetic Resonance Imaging*, 35:1462–1471, 2012.

[123] A.F. Stalder, Z. Dong, Q. Yang, J. Bock, J. Hennig, M. Markl, and K. Li. Four-dimensional flow-sensitive mri of the thoracic aorta: 12-versus 32-channel coil arrays. *Journal of Magnetic Resonance Imaging*, 35(1):190–195, 2012.

[124] B. Jung, A.F. Stalder, S. Bauer, and M. Markl. On the undersampling strategies to accelerate time-resolved 3d imaging using k-t-grappa. *Magnetic Resonance in Medicine*, 66(4):966–975, 2011.

[125] CJ Mills, IT Gabe, JH Gault, DT Mason, J. Ross Jr, E. Braunwald, JP Shillingford, et al. Pressure-flow relationships and vascular impedance in man. *Cardiovasc Res*, 4(4):405–417, 1970.

[126] A. Nasiraei-Moghaddam, G. Behrens, N. Fatouraee, R. Agarwal, E. T. Choi, and A. A. Amini. Factors affecting the accuracy of pressure measurements in vascular stenoses from phase-contrast mri. *Magn Reson Med*, 52(2):300–9, 2004.

[127] G.R. Marx and H.D. Allen. Accuracy and pitfalls of doppler evaluation of the pressure gradient in aortic coarctation. *Journal of the American College of Cardiology*, 7(6):1379–1385, 1986.

[128] P. Syamasundar Rao and P. Carey. Doppler ultrasound in the prediction of pressure gradients across aortic coarctation. *American Heart Journal*, 118(2):299–307, 1989.

[129] DC. Fyler, JF. Keane, and JE Lock. *Nadas' pediatric cardiology*. Hanley & Belfus Philadelphia, 1992.

[130] S.D. Colan. Quantitative applications of doppler cardiography in congenital heart disease. *Cardiovascular and interventional radiology*, 10(6):332–347, 1987.

[131] W. Lai. *Echocardiography in pediatric and congenital heart disease: from fetus to adult*. Wiley-Blackwell, 2009.

[132] F. Staehle, B.A. Jung, S. Bauer, J. Leupold, J. Bock, R. Lorenz, D. Föll, and M. Markl. Three-directional acceleration phase mapping of myocardial function. *Magnetic Resonance in Medicine*, 65(5):1335–1345, 2011.

[133] J.P. Tasu, E. Mousseaux, A. Delouche, C. Oddou, O. Jolivet, and J. Bittoun. Estimation of pressure gradients in pulsatile flow from magnetic resonance acceleration measurements. *Magnetic resonance in medicine*, 44(1):66–72, 2000.

[134] M. Markl, W. Wallis, S. Brendecke, J. Simon, A. Frydrychowicz, and A. Harloff. Estimation of global aortic pulse wave velocity by flow-sensitive 4d mri. *Magnetic Resonance in Medicine*, 63(6):1575–1582, 2010.

Publications

Journal papers

- A.J. Barker, M. Markl, J. Bürk, R. Lorenz, **J. Bock**, S. Bauer, J. Schulz-Menger, and F. von Knobelsdorff-Brenkenhoff. *Bicuspid aortic valve is associated with altered wall shear stress in the ascending aorta.* Circulation: Cardiovascular Imaging, published online, 2012.

- S. Krittian, P. Lamata, C. Michler, D.A. Nordsletten, **J. Bock**, C.P. Bradley, A. Pitcher, P.J. Kilner, M. Markl, and N.P. Smith. *A finite-element approach to the direct computation of relative cardiovascular pressure from time-resolved MR velocity data.* Medical Image Analysis, 16(5):1029–1037, 2012.

- A. Frydrychowicz, A. Berger, A. Munoz del Rio, M.F. Russe, **J. Bock**, A. Harloff, and M. Markl. *Interdependencies of aortic arch secondary flow patterns, geometry, and age analysed by 4-dimensional phase contrast magnetic resonance imaging at 3 Tesla.* European Radiology, 22:1122–1130, 2012.

- A.F. Stalder, Z. Dong, Q. Yang, **J. Bock**, J. Hennig, M. Markl, and K. Li. *Four-dimensional flow-sensitive MRI of the thoracic aorta: 12- versus 32-channel coil arrays.* Journal of Magnetic Resonance Imaging, 35(1):190–195, 2012.

- R. Lorenz, C. Benk, **J. Bock**, AF Stalder, JG Korvink, J. Hennig, and M. Markl. *Closed circuit MR compatible pulsatile pump system using a ventricular assist device and pressure control unit.* Magnetic Resonance in Medicine, 67(1):258–68, 2012.

- A.J. Barker, F. Staehle, **J. Bock**, B.A. Jung, and M. Markl. *Analysis of complex cardiovascular flow with three-component acceleration-encoded MRI.* Magnetic Resonance in Medicine, 67(1):50–61, 2012.

- **J. Bock**, A. Frydrychowicz, R. Lorenz, D. Hirtler, A.J. Barker, K.M. Johnson, R. Arnold, H. Burkhardt, J. Hennig, and M. Markl. *In vivo noninvasive 4D pressure difference mapping in the human aorta: Phantom comparison and application in healthy volunteers and patients.* Magnetic Resonance in Medicine, 66:1079–1088, 2011.

- C. Benk, R. Lorenz, F. Beyersdorf, **J. Bock**, R. Klemm, J.G. Korvink, and M. Markl. *Three-dimensional flow characteristics in ventricular assist devices:*

Impact of valve design and operating conditions. The Journal of Thoracic and Cardiovascular Surgery, 142(5):1019–1026, 2011.

- O. Friman, A. Hennemuth, A. Harloff, **J. Bock**, M. Markl, and H.O. Peitgen. *Probabilistic 4D blood flow tracking and uncertainty estimation.* Medical Image Analysis, 15(5):720–8, 2011.

- T. Schubert, F. Santini, AF Stalder, **J. Bock**, S. Meckel, L. Bonati, M. Markl, and S. Wetzel. *Dampening of blood-flow pulsatility along the carotid siphon: Does form follow function?* American Journal of Neuroradiology, 32(6):1107–1112, 2011.

- F. Staehle, B.A. Jung, S. Bauer, J. Leupold, **J. Bock**, R. Lorenz, D. Föll, and M. Markl. *Three-directional acceleration phase mapping of myocardial function.* Magnetic Resonance in Medicine, 65(5):1335–1345, 2011.

- **J. Bock**, A. Frydrychowicz, A.F. Stalder, T.A. Bley, H. Burkhardt, J. Hennig, and M. Markl. *4D phase contrast MRI at 3T: Effect of standard and blood-pool contrast agents on SNR, PC-MRA, and blood flow visualization.* Magnetic Resonance in Medicine, 63(2):330–338, 2010.

- A. Frydrychowicz, M.F. Russe, **J. Bock**, A.F. Stalder, T.A. Bley, A. Harloff, and M. Markl. *Comparison of gadofosveset trisodium and gadobenate dimeglumine during time-resolved thoracic MR angiography at 3T.* Academic Radiology, 17(11):1394 – 1400, 2010.

- O. Friman, A. Hennemuth, A. Harloff, **J. Bock**, M. Markl, and H.-O. Peitgen. *Probabilistic 4D blood flow mapping.* Med Image Comput Comput Assist Interv, 13(Pt 3):416–423, 2010.

- F. Santini, S.G. Wetzel, **J. Bock**, M. Markl, and K. Scheffler. *Time-resolved three-dimensional (3D) phase-contrast (PC) balanced steady-state free precession (bssfp).* Magnetic Resonance in Medicine, 62(4):966–974, 2009.

- A. Frydrychowicz, A.F. Stalder, M.F. Russe, **J. Bock**, S. Bauer, A. Harloff, A. Berger, M. Langer, J. Hennig, and M. Markl. *Three-dimensional analysis of segmental wall shear stress in the aorta by flow-sensitive four-dimensional-MRI.* Journal of Magnetic Resonance Imaging, 30(1):77–84, 2009.

- A. Harloff, C. Strecker, P. Dudler, A. Nussbaumer, A. Frydrychowicz, M. Olschewski, **J. Bock**, A.F. Stalder, A.L. Stroh, C. Weiller, et al. *Retrograde embolism from the descending aorta: visualization by multidirectional 3D velocity mapping in cryptogenic stroke.* Stroke, 40(4):1505, 2009.

- A. Harloff, F. Albrecht, J. Spreer, AF Stalder, **J. Bock**, A. Frydrychowicz, J. Schöllhorn, A. Hetzel, M. Schumacher, J. Hennig, et al. *3D blood flow*

characteristics in the carotid artery bifurcation assessed by flow-sensitive 4D MRI at 3T. Magnetic Resonance in Medicine, 61(1):65–74, 2009.

- A. F. Stalder, M. F. Russe, A. Frydrychowicz, **J. Bock**, J. Hennig, and M. Markl. *Quantitative 2D and 3D phase contrast MRI: optimized analysis of blood flow and vessel wall parameters.* Magn Reson Med, 60(5):1218–1231, 2008.

- C. Canstein, P. Cachot, A. Faust, AF Stalder, **J. Bock**, A. Frydrychowicz, J. Küffer, J. Hennig, and M. Markl. *3D MR flow analysis in realistic rapid-prototyping model systems of the thoracic aorta: Comparison with in vivo data and computational fluid dynamics in identical vessel geometries.* Magnetic Resonance in Medicine, 59(3):535–546, 2008.

- A. Frydrychowicz, M. Markl, A. Harloff, AF Stalder, **J. Bock**, TA Bley,A. Berger, MF Russe, C. Schlensak, J. Hennig, et al. *Flow-sensitive in-vivo 4D MR imaging at 3T for the analysis of aortic hemodynamics and derived vessel wall parameters.* RöFo: Fortschritte auf dem Gebiete der Röntgenstrahlen und der Nuklearmedizin, 179(5):463, 2007.

Conference proceedings (as first author)

- **J. Bock**, H. Burkhardt, and M. Markl. *A new approach for time-resolved 3D phase-contrast MRA.* In Proceedings 20th Scientific Meeting, International Society for Magnetic Resonance in Medicine, Melbourne, Australia, 2012.

- **J. Bock**, H. Burkhardt, and M. Markl. *A new approach for time-resolved 3D phase-contrast MRA.* In 23nd Annual International Conference on Magnetic Resonance Angiography, Banff, Canada 2011.

- **J. Bock**, R. Lorenz, A. Harloff, and M Markl. *4D aortic pressure difference mapping: an approach for the detection of pressure wave changes associated with atherosclerosis?* In Proc 19th Scientific Meeting, International Society for Magnetic Resonance in Medicine, Montreal, Canada, 2011.

- **J. Bock**, R. Lorenz, A. Harloff, and M. Markl. *4D pressure difference mapping in the aorta.* In Proceedings 22nd Annual International Conference on MR Angiography, Seoul, South Korea, 2010.

- **J. Bock**, F. Staehle, R. Lorenz, K. Johnson, J. Hennig, and M. Markl. *Pressure gradient estimation from PC-MRI: acceleration versus velocity encoding.* In Proceedings 18th Scientific Meeting, International Society for Magnetic Resonance in Medicine, Stockholm, Sweden, 2010.

- **J. Bock**, A. Frydrychowicz, R. Lorenz, K. Johnson, R. Arnold, J. Hennig, and M. Markl. *4D pressure difference mapping in the aorta.* In Workshop on

Cardiovascular Flow, Function & Tissue Mechanics, Sintra, Portugal, Sintra, Portugal, 2009.

- **J. Bock**, A. Frydrychowicz, K. Johnson, O. Wieben, J. Hennig, and M. Markl. *Optimized data analysis for the assessment of aortic pressure difference maps.* In Proceedings 17th Scientific Meeting, International Society for Magnetic Resonance in Medicine, Honolulu, USA, 2009.

- **J. Bock**, K. Johnson, O. Wieben, J. Hennig, and M. Markl. *Aortic PC-MRA based on PC-MRI data.* In 20th Annual Internationl Conference on Magnetic Resonance Angiography, Graz, Austria, 2008.

- **J. Bock**, A. Frydrychowicz, T. Bley, A. Stalder, M. Russe, M. Keckeis, J. Hennig, and M. Markl. *3D phase contrast MRA of the thoracic aorta at 3T: Feasibility and effect of standard and blood-pool contrast agents.* In 16th Scientific Meeting, International Society for Magnetic Resonance in Medicine, Toronto, Canada, 2008.

- **J. Bock**, O. Wieben, K. Johnson, J. Hennig, and M. Markl. *Optimal processing to derive static PC-MRA from time-resolved 3D PC-MRI data.* In 16th Scientific Meeting, International Society for Magnetic Resonance in Medicine, Toronto, Canada, 2008.

- **J. Bock**, B. W. Kreher, J. Hennig, and M. Markl. *Optimized pre-processing of time-resolved 2d and 3d phase contrast MRI data.* In 15th Scientific Meeting International Society for Magnetic Resonance in Medicine, Berlin, Germany, 2007.

Talks & Seminars

- **J. Bock.** *4D pressure difference mapping in the aorta.* In University of Oxford - 4D Flow Workshop, Oxford, England, 2011.

- **J. Bock.** *Post-processing of 4D phase contrast MRI data.* In University of Oxford - 4D Flow Workshop, Oxford, England, 2011.

- **J. Bock**. *4D pressure difference mapping in the aorta.* In Xuanwu-Freiburg Workshop, Beijing, China, 2010.

- **J. Bock**. *Flow-sensitive 4D MRI.* In 2nd Madison-Freiburg Workshop on Accelerated Medical Imaging, Madison, USA, 2010.

- **J. Bock**. *Aortic PC-MRA based on 4D PC-MRI data.* In Seminar MR, Abt. Radiologie, Medizin Physik, University Medical Center Freiburg, Germany, 2009.

- **J. Bock**. *Pressure difference mapping.* In Oberseminar CeVis/MeVis, Bremen,

Germany 2008.

Awards

- Best paper award (Medical Image Analysis-MICCAI 2011) for the paper: O. Friman, A. Hennemuth, A. Harloff, **J. Bock**, M. Markl, and H.O. Peitgen. *Probabilistic 4D blood flow tracking and uncertainty estimation.* Medical Image Analysis, 15(5):720–8, 2011.

- R. Lorenz, **J. Bock**, S. Huff, A. Barker, M. Markl. Winners of the Potchen award for the best presentation at the MR angiography meeting, Seoul, South Korea, 2010.

Danksagung

An dieser Stelle möchte ich mich bei allen bedanken, die mich während der letzten Jahren unterstützt haben, und somit zum Gelingen dieser Arbeit beigetragen haben.

Prof. Dr. Hans Burkhardt danke ich für das Betreuen der Arbeit seitens der Technischen Fakultät sowie für seine hilfreichen Anregungen und Ratschläge.

Bei Prof. Dr. Jürgen Hennig bedanke ich mich für die Bereitstellung der Arbeit sowie die Möglichkeit in seiner Arbeistgruppe zu forschen.

Mein ganz besonderer Dank gilt Prof. Dr. Michael Markl für die hervorragende Betreung meiner Arbeit. Durch die guten Ratschläge und Diskussionen gab er mir die notwendige Unterstützung und durch seine Begeisterung für die Forschung verstand er immer zu motivieren.

Allen Cardio-Gruppenmitgliedern danke ich für die Diskussionen und Unterstützung, insbesondere Ramona Lorenz für die netten Stunden innerhalb und außerhalb unseres Büros sowie für die Phantomdatenakquisition.

Den klinischen Partnern, insbesondere Dr. Alex Frydrychowicz, danke ich für die Unterstützung bei den klinischen Fragen.

Laurence Haller danke ich für das Managen der finanziellen und verwaltungstechnischen Situtationen.

Bei Stefanie Schwenk, Dr. Marco Reisert und Dr. Jeff Snyder bedanke ich mich für das sorgfältige Korrekturlesen meiner Arbeit.

Ich bedanke mich bei all meinen Freunden für ihre Unterstützung.

Meinem Freund und Partner Frederik Testud möchte ich für seine Unterstützung,

Ermunterung und die Verlässlichkeit in jeder Situation danken.

Nicht zuletzt danke ich von ganzem Herzen meinen Eltern, Tamara und Viktor Bock, die mich immer bedingungslos unterstützt haben und ohne die das alles nicht möglich gewesen wäre.